AGH University of Science and Technology

Doctoral Dissertation

Beam test studies of monolithic pixel structures for CLIC vertex detector

Author:
mgr inż. Roma Bugiel

Supervisor:
prof. dr hab. inż. Marek Idzik
dr inż. Krzysztof Świentek

AGH University of Science and Technology

Faculty of Physics and Applied Computer Science
Department of Particle Interactions and Detection Techniques

May, 2019

Declaration of Authorship

Declaration of the author of this dissertation:
Aware of legal responsibility for making untrue statements I hereby declare that I have written this dissertation myself and all the contents of the dissertation have been obtained by legal means.

Signed: _____

Date: _____

Declaration of the dissertation Supervisors:
This dissertation is ready to be reviewed.

Signed: _____

Date: _____

Signed: _____

Date: _____

Abstract

Roma BUGIEL

Beam test studies of monolithic pixel structures for CLIC vertex detector

The Compact Linear Collider (CLIC) is an international project of e^+e^- linear accelerator with maximal centre-of-mass energy of 3 TeV. It is planned to be located near CERN scientific centre in Switzerland. The intensive development of both accelerator and detectors are ongoing. One of the challenging part is a vertex detector, which physics-driven requirements are highly demanding. For this detector, situated closest to an interaction point, a spatial resolution of 3 µm, time-stamping of 10 ns and material budget less than 0.2 % of radiation length per layer is foreseen. In order to reach these goals different silicon detector technologies are being tested, including monolithic solutions. Theirs benefit over hybrid technologies is that they integrate readout electronics and sensor matrix on the same wafer and bump-bonding process is no longer needed. This limits the material budget of a detector, decreasing a particle scattering.

In this dissertation the test-beam data analysis results of monolithic pixel detectors designed in Japanese Fully-Depleted Low-Leakage Lapis 200 nm Silicon-On-Insulator (SOI) CMOS technology are presented. The SOI CMOS is implementing an insulator layer into standard CMOS structure and thus a substrate and thin silicon layer dedicated for electronics circuits are separated from each other. For the substrate the highly-resistive silicon wafer is used which makes the structure perfect for particle detectors.

Two pixel detector prototypes targeted to fulfill the CLIC vertex detector spatial resolution requirement were designed in Cracow, fabricated in Japan and tested in CERN. The prototypes incorporate source follower and charge-sensitive preamplifier pixel readout electronics. The pixel size is 30 µm $\times$ 30 µm and the matrix consists of 16 $\times$ 36 pixels. The detectors were fabricated on different substrate types. Both systems were tested on beam at Super Proton Synchrotron (SPS) in collaboration with CLICdp group.

Various analysis methods were developed in terms of the SOI pixel detector performance studies, focusing mainly on the efficiency and spatial resolution optimisation. The results indicate on a very good performance of the tested prototypes. The spatial resolution is in the best case on the level of 2.1 – 2.7 µm at the efficiency of about 96 % – 98 %. The performed studies show a high potential of the SOI CMOS technology for future devices proposed for the CLIC vertex detectors and other highly-demanding applications.

Streszczenie

Roma BUGIEL

Beam test studies of monolithic pixel structures for CLIC vertex detector

CLIC (The Compact Linear Collider) jest międzynarodowym projektem liniowego zderzacza leptonów, który miałby zostać zbudowany w Europejskim Ośrodku Badań Jądrowych (CERN) w pobliżu Genewy. W CLIC zderzane mają być pozytony i elektrony z maksymalną energią w środku masy, która być równa 3 TeV dla ostatniego stopnia. Obecnie projekt jest w intensywnej fazie rozwoju zarówno pod kątem akceleratora, jak i detektorów. Ostateczna decyzja na temat budowy CLIC ma zapaść w najbliższym czasie. Jednym z najbardziej wymagających detektorów dla CLIC jest detektor wierzchołka, położony najbliżej punktu zderzenia wiązek. Szacuje się, że aby spełnić fizyczne założenia eksperymentu, detektor wierzchołka powinien cechować się rozdzielczością przestrzenną lepszą niż 3 µm, rozdzielczością czasową poniżej 10 ns oraz budżetem materiałowym nie większym niż 200 µm, biorąc pod uwagę kable, system chłodzenia oraz statyw. Z uwagi na fakt, że wymagania te są obecnie stosunkowo trudne do osiągnięcia, testuje się wiele różnych technologii detektorowych, w tym rozwiązania monolityczne. W porównaniu do naj bardziej popularnych detektorów hybrydowych, detektory monolityczne integrują elektronikę odczytu oraz matrycę sensorów na tym samym waflu krzemowym. Dzięki temu nie jest wymagany proces *bump-bondingu*, co pozwala zmniejszyć budżet materiałowy detektora, a przez to ograniczyć rozpraszanie cząstek na jego objętości.

Głównym przedmiotem niniejszej rozprawy jest analiza danych z testów na wiązce monolitycznego detektora krzemowego, w japońskiej technologii Lapis 200 nm *Silicon-On-Insulator* (SOI) CMOS. W porównaniu do standardowej struktury CMOS, SOI wprowadza warstwę izolatora, separującą podłoże od cienkiej warstwy krzemu przeznaczonej na elektronikę. Dzięki temu, że dobór wafla krzemowego na elektronikę i podłoże jest w SOI CMOS dowolny, istnieje możliwość zaimplementowania wysokorezystywnego podłoża dedykowanego dla matrycy sensorów. Taka struktura staje się bardzo dobrym kandydatem do produkcji monolitycznych detektorów krzemowych.

Przedmiotem badań przedstawionych w tej pracy są dwa prototypy detektorów SOI CMOS, zaprojektowanych w Krakowie, wyprodukowanych w Japonii, a następnie przetestowanych na wiązce w CERN w Szwajcarii. Testy na wiązce odbyły się dwukrotnie, w 2016 oraz w 2017 roku, w kolaboracji z grupą CLICdp. Głównym celem pracy było zweryfikowanie, czy mierzone prototypy są w stanie osiągnąć rozdzielczość przestrzenną wymaganą przez detektor wierzchołka dla eksperymentu CLIC. Detektory posiadały matryce

16×38 pikseli o wymiarze $30 \times 30\,\mu m^2$ oraz zostały wyprodukowane na różnych podłożach krzemowych (*Floating Zone* typu n oraz *Double SOI* typu p). Zmierzona rozdzielczość przestrzenna wynosiła około $2.1 - 2.7\,\mu m$ w zależności od typu testowanego detektora. Efektywność została oszacowana na około $96\,\% - 98\,\%$. Uzyskane wyniki wskazują na to, że SOI CMOS jest bardzo obiecującą technologią dla detektora wierzchołka eksperymentu CLIC.

Acknowledgements

I would like to thank my supervisors: Marek Idzik and Krzysztof Świentek for shared experience and wide knowledge provided me during my doctoral studies. I would not be as open-minded as I became, without possibilities gave me by Marek Idzik for international co-operations and internships. My thesis-paper would be significantly less professional without support from Krzysztof Świentek, as well.

Furthermore, I would like to thank CLICdp team for test-beams organisation and overall support. I appreciate a lot an excellent working and social atmosphere.

Next, thank You, Szymon, for being always the deck captain, in the full sense of this word. You are the best one on this position.

Especially, I wish to thank my parents, Jolanta and Shankar, for inspirations, essential education and being always a trustworthy and irreplaceable support. This PhD is more Your success than mine.

I would like to thank also great teachers that I have met on my way. In particular, Mariusz Przybycien, for proving that physics enthusiasts really exist. (I would like to ensure You, that I am still working on true physics). And also Grażyna and Jarosław Linder. Thanks to them I become a physicist. You could not do a better job.

Finally, a lot of thanks for Ela, for being a confidante, whatever happens, and the only one reliable source of information.

This work was financed by the European Union Horizon 2020 Marie Sklodowska-Curie Research and Innovation Staff Exchange program under Grant Agreement no. 645479 (E-JADE) and also by the Polish Ministry of Science and Higher Education from funds for science in the years 2017 – 2018 allocated to an international co-financed project.

Contents

List of Abbreviations

2HLM	Two **H**ighiest **L**ine Clusterization **M**ethod
2TM	Two **T**hreshold Clusterization **M**ethod
3PM	Three **P**ixel Clusterization **M**ethod
4PM	Four **P**ixel Clusterization **M**ethod
9PM	Nine **P**ixel Clusterization **M**ethod
ASIC	**A**pplication-**S**pecific **I**ntegrated **C**ircuit
ADC	**A**nalogue-to-**D**igital **C**onverter
ADU	**A**nalogue-to-**D**igital converter **U**nits
BN(P)W	**B**uried **N**(**P**)-**W**ell
BOX	**B**uried-**O**xide
BSM	**B**eyond **S**tandard **M**odel
CCPD	**C**apacitive **C**oupled **P**article **D**etector
CDR	**C**onceptual **D**esign **R**eport
CERN	The European Organization for Nuclear Research
CDS	**C**orrelated **D**ouble **S**ampling
CMOS	**C**omplementary **M**etal-**O**xide **S**emiconductor
CLIC	**C**ompact **L**inear **C**ollider
CLIPS	**CLI**C **P**ixel **S**oi
COG	**C**enter **O**f **G**ravity
CPA	**C**harge-sensitive **P**re**a**mplifier
CROS	**Cros**s Clusterization Method
CZ-n	**C**z**o**chralski type **n**
DAQ	**D**ata **Ac**quisition
DRC	**D**esign **R**ule **C**heck
DSOI(-p)	**D**ouble **S**ilicon **O**n **I**nsulator (type **p**)
DUT	**D**evice **U**nder **T**est
ECAL	**E**lectromagnetic **CAL**orimeter
ENC	**E**quivalent **N**oise **C**harge
FD	**F**ully-**D**epleted
FPGA	**F**ield-**P**rogrammable **G**ate **A**rray
FZ-n(-p)	**F**loating **Z**one type **n** (type **p**)
GEAR	**Ge**ometry **A**PI for **R**econstruction
GUI	**G**raphical **U**ser **I**nterface
HCAL	**H**adronic **CAL**orimeter
HL-LHC	**H**igh-**L**uminosity **L**arge **H**adron **C**ollider

HR-CMOS	**H**igh-**R**esistivity **C**omplementary **M**etal-**O**xide **S**emiconductor
Mid-Si	**Mid**dle-**Si**licon
HV-CMOS	**H**igh-**V**oltage **C**omplementary **M**etal-**O**xide **S**emiconductor
ILC	**I**nternational **L**inear **C**ollider
I/O	**I**nput / **O**utput
IP	**I**nteraction **P**oint
KEK	The High Energy Accelerator Research Organization
LCC	**L**inear **C**ollider **C**ollaboration
LCIO	**L**inear **C**ollider **I/O**
LHC	**L**arge **H**adron **C**ollider
Marlin	**M**odular **A**nalysis and **R**econstruction for the **LIN**ear collider
MIP	**M**inimum **I**onizing **P**article
MPV	**M**ost **P**robable **V**alue
NMOS	**N**-channel **MOS**FET
PCB	**P**rinted **C**ircuit **B**oard
PETS	**P**ower **E**xtraction and **T**ransfer **S**tructures
PMOS	**P**-channel **MOS**FET
R&D	**R**esearch and **D**evelopment
RMS	**R**oot **M**ean **S**quare
RF	**R**adio-**F**requency
SAR	**S**uccessive **A**pproximation **R**egister
SCR	**S**pace **C**harge **R**egion
SEE	**S**ingle **E**vent **E**ffects
SF	**S**ource **F**ollower
SNR	**S**ignal to **N**oise **R**atio
SM	**S**tandard **M**odel
SOI	**S**ilicon **O**n **I**nsulstor
SPIDR	**S**peedy **Pi**xel **D**etector **R**eadout
SPS	**S**uper **P**roton **S**ynchrotron
SUSY	**SU**per**SY**mmetry
TCP	**T**ransmission **C**ontrol **P**rotocol
TID	**T**otal **I**onizing **D**ose
ToA	**T**ime **o**f **A**rrival
ToT	**T**ime **o**ver **T**hreshold
UDP	**U**ser **D**atagram **P**rotocol
XML	E**X**tensible **M**arkup **L**anguage

Introduction

The Large Hardon Collider (LHC) located close to Geneva is presently the largest and the most powerful collider, meant for scientific high energy physics researches. The LHC was built by the European Organization for Nuclear Research, known as CERN, being a significant European physics scientific centre. The LHC is a circular accelerator able to collide proton beams with a centre-of-mass energy up to 13 TeV. In 2012, the Higgs particle observation and its mass determination [1] was considered as one of the main success of the LHC and a milestone in physics researches.

In 2018 a large upgrade of the LHC has been started and it is called High-Luminosity LHC (HL-LHC) project. A main aim of the present modernization is to increase a luminosity. The HL-LHC will run on its full capabilities in the year 2026 [2], providing a high-quality physical data. Although the LHC upgrade is being just started, plans over its successor are still ongoing. A main goal of a next collider is to complete the LHC measurements over the Higgs boson, to investigate the Supersymmetry Theory (SUSY) and to study physics Beyond Standard Model (BSM), as well.

In order to perform a precise measurements of the particles discovered by the LHC, there is a need to study leptons collisions, since these events are clean and more straightforward to analyse. There are two options for accelerator type: a circular or linear accelerator, both having many advantages depending on working energy ranges. The circular solutions may be used effectively for longer distance to accelerate and moreover, a beam is not lost after the collision. The main problem that occurs is a synchrotron radiation, so the electromagnetic radiation that is emitted when charged particle trajectory is bent. The energy loss caused by electromagnetic radiation is inversely proportional to the fourth power of a particle mass. Due to this effect, e^+e^- acceleration cannot be efficiently performed in circular accelerators. The solution is to develop a linear collider.

At present, there are two main linear collider projects: the International Linear Collider (ILC) and the Compact Linear Collider (CLIC). The ILC is planned to have a centre-of-mass energy of 500 GeV with possibility to 1 TeV upgrade. CLIC foresees three energy stages starting from 380 GeV with an upgrading up to 1.5 TeV and 3 TeV. The Linear Collider Collaboration (LCC) unites both projects in order to coordinate and increase quality of the research and development (R&D).

As mentioned earlier, the researches on detectors and accelerator development are ongoing for both linear colliders. The main subject of this doctoral dissertation is focused on the R&D over a vertex detector for the CLIC experiment. Author of presented researches

belongs to Poland-based Cracow scientific group, which is currently developing pixel detectors in the advanced Japanese Silicon-On-Insulator (SOI) Complementary Metal-Oxide-Semiconductor (CMOS) technology provided by the Lapis Semiconductor Company. The SOI CMOS introduces an insulator layer to a standard CMOS structure, separating a high-resistivity substrate and a thin silicon layer. Such a structure provides possibility of monolithic pixel detectors production.

The Cracow scientific group is one of the very few European teams, working within the international SOIPIX collaboration. The SOIPIX collaboration, joining many scientific groups mainly from Japan and China, is developing monolithic pixel detectors in Lapis 200 nm Fully-Depleted (FD) Low-Leakage SOI technology. A leader of the collaboration is the High Energy Accelerator Research Organization (KEK) scientific centre hosted in Japanese Tsukuba city which works closely with Lapis Semiconductor Company. SOIPIX develops detectors for particle physics, astrophysics and X-ray imaging [3]. Currently, one of the most advanced systems that have been developed in Lapis SOI CMOS technology are SOPHIST [4] for the ILC, XRPIX for astrophysics [5] and INTPIX general purpose pixel detectors family [6, 7].

The detector prototyping taking place in Cracow is ultimately targeted to meet requirements of the CLIC vertex detector. At this stage, it has been assumed that the CLIC vertex detector needs to have at least 3 µm single-point spatial resolution, 10 ns time-stamping and 200 µm detector thickness including cables, supports and cooling systems. A power consumption limitation is set at $50\,\mathrm{mW/cm^2}$.

A full detector production chain is being developed in Cracow for the CLIC vertex detector prototype. It starts from detector design, including readout electronics, sensor layout, signal post-processing circuits and finishes with detailed data analysis. Also detector measurement setups are being prepared for laboratory measurements with radioactive source and for tests on beam, as well. Author of this dissertation, as a participant of the described project research, has been also involved in the SOI detector design, mainly control logic, analouge-to-digital converter (ADC) and data acquisition during test-beams but an essential task of the doctoral studies was aimed at the analysis of a test-beam data. Two detector prototypes were measured with a particle beam on Super Proton Synchrotron (SPS) at CERN in 2016 and 2017 year. The project was focused on calculation of an efficiency and spatial resolution parameters. Meeting other requirements, such as timing resolution and power consumption is foreseen for the next prototype called CLIPS (CLIc Pixel Soi). CLIPS has been already designed and fabricated but not tested so far.

The important part of this work was to develop a dedicated data analysis software that allowed for testing and extracting overall detector performance. The development of the dedicated data analysis tool is a key step in the first stages of detector studies. Although there are several analysis softwares available for this purpose, as for example Modular Analysis and Reconstruction for the LINear collider (Marlin) [8] for linear accelerators, they are usually very sophisticatedly designed and complex in their functions. This feature makes them very useful in a case of systematic detectors testing, but this is not practical when intensive research and debugging of the system is of the primary interest. For this reason it

was crucial to develop the dedicated analysis tool in terms of efficient detector prototypes studies.

The used technology Lapis 200 nm SOI is just being developed in the context of use for particle detectors. The systems produced in Lapis SOI CMOS have many physical features that yet need to be thoroughly studied and comprehended in order to fully use the potential of this technology in practice. Therefore, the data analysis program must be not only flexible, but also should possess high functionality at the same time. This is also an important issue why the separate, dedicated analysis tool for SOI prototypes has been developed as a large contribution to this doctoral project. However, the proposed algorithms are universal and can be applied to other similar systems, which make the work useful for the development of a silicon pixel detector in general.

The main goal of the research analysis is to achieve at least 3 µm spatial resolution required by the CLIC vertex detector. Taking into account that pixel size is $30 \times 30\,\mu m^2$, it has been demanding goal to reach. The significant charge sharing effect for the tested detectors turns out to be its main advantage, allowing to significantly improve spatial resolution. For this reason, various clustering methods were investigated to find the best working one and the multi-pixel η-correction algorithm was developed, as well. Introduction of such dedicated algorithms made it possible to achieve the target spatial resolution of around 2 µm at 98 % of the detector efficiency.

This thesis is comprised of an introduction, five separated chapters with work presentations and a final chapter to close the dissertation with conclusion. To chapter 1 glances through the CLIC experiment, giving brief introduction to physics at CLIC and then to an accelerator and detector projects. Current technologies for the vertex detector are described as well, with the main focus on the SOI CMOS monolithic technology. The chapter 2 describes a theoretical background of charged particle interactions with matter and it introduces basic concepts of working principles and properties of silicon particle detectors. Following to that, the next chapter 3 describes the detector design and used measurements setups. The test-beam infrastructure is also presented there in the third chapter. After-where, the analysis methods and developed algorithms are presented in chapter 4. The final results, being the core of this dissertation, focused on spatial resolution and efficiency calculations are described in the chapter 5. To sum up, the last chapter 6 concludes the research results and also gives an overview on overall future plans. In appendix A the complementary results are shown. Finally, at the end this work comprises a bibliography.

Chapter 1

The Compact Linear Collider (CLIC)

The development of an accelerator and detectors for particle physics experiments is an extremely complex and time-consuming process. Thus, the R&D phase for large colliders begins many years before the project final approval. The first CLIC Conceptual Design Report (CDR) was published in 2012 [9] and the updated versions based on many years of development and the LHC discoveries have been shown in 2018 – 2019 [10, 11]. The R&D for CLIC is currently in its final stage and the future of this experiment will be clarified in the Update of the European Strategy for Particle Physics 2019 – 2020.

CLIC is the international project of e^+e^- linear accelerator developed at CERN in Switzerland [12]. The main accelerator is planned to be placed underground near Geneva city as it is presented in the figure 1.1. The machine is going to collide electrons and positrons with centre-of-mass energy from 380 GeV to 3 TeV depending on experiment stage. There are three stages foreseen. The current status of basic parameters at various energy stages is shown in the table 1.1. CLIC energy parameters have been updated after Higgs boson discovery and may be further tuned after the LHC final data collection. The physics background of the CLIC experiment is mainly determining the technical demands put on both the accelerator and detectors.

TABLE 1.1: Basic parameters of the CLIC energy stages [10].

Parameter	**Symbol**	**Unit**	**Stage 1**	**Stage 2**	**Stage 3**
Centre-of-mass energy	$\sqrt{\sigma}$	GeV	380	1500	3000
Main tunnel length		km	11.4	29.0	50.1
Total luminosity	L	$10^{34}/(\mathrm{cm}^2 \cdot \mathrm{s})$	1.5	3.7	5.9
Acceleration gradient	G	MV/m	72	72/100	72/100
Power consumption	P	MW	252	364	589
Repetition frequency	f_{rep}	Hz	50		
Train length	τ_{train}	ns	156		
Bunch length	σ_z	µm	70	44	44
IP beam size	σ_x/σ_y	nm	$\sim 149/2.9$	$\sim 60/1.5$	$\sim 40/1$
Bunch separation	Δ_t	ns	0.5		
Nb of bunches per train	n_b	–	352	312	312
Nb of particles per bunch	N	$\times 10^9$	5.2	3.7	3.7

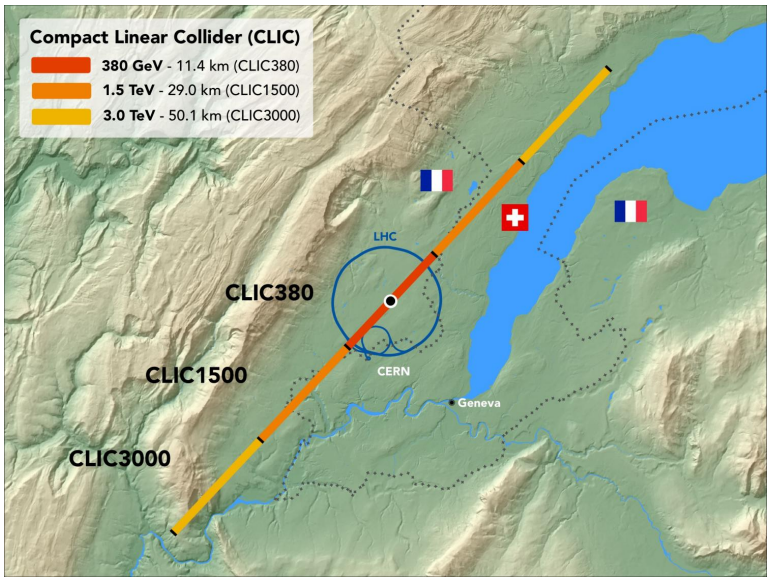

FIGURE 1.1: CLIC proposed location [12].

1.1 Physics at CLIC

The physics at CLIC will be focused on several goals depending on the project energy stage. The first CLIC stage will cover 380 GeV centre-of-mass energy and the Higgs basic parameters extraction will be undertaken as well as top quark physics measurements. The next two stages: 1.5 TeV and 3 TeV are going to cover rare Higgs processes, physic Beyond Standard Model (BSM), dark mater candidates and new particles search.

1.1.1 Higgs physics

CLIC is often called "Higgs-factory", since the e^+e^- collisions provide clean events with well-defined initial and final state, so parameters of the Higgs particle can be precisely measured. There are three processes of the highest cross-section dominating the first stage of the CLIC experiment:

$$\text{Higgsstrahlung:} \quad e^+e^- \to ZH \tag{1.1}$$

$$\text{WW-fusion:} \quad e^+e^- \to H\overline{\nu_e}\nu_e \tag{1.2}$$

$$\text{ZZ-fusion:} \quad e^+e^- \to He^+e^- \tag{1.3}$$

where W is W-boson, Z is Z-boson, H is the Higgs particle and $\overline{\nu_e}/\nu_e$ are electron antineutrino and neutrino respectively. All these processes are shown using Feynman diagrams in Fig. 1.2A. The single Higgs production incorporates mainly Higgsstrahlung, dominant up to 450 GeV, whereas WW-fusion covers large statistics above this energy. The WW-fusion and ZZ-fusion are significant in terms of the Higgs boson coupling to fermions and gauge bosons. Moreover, the Higgs rare processes may be observed, as for example top quark (t) Yukawa coupling ($e^+e^- \to t\bar{t}H$) shown also in Fig. 1.2A, giving a precise look into the Higgs particle parameters and the Higgs potential. A summary of these processes is presented

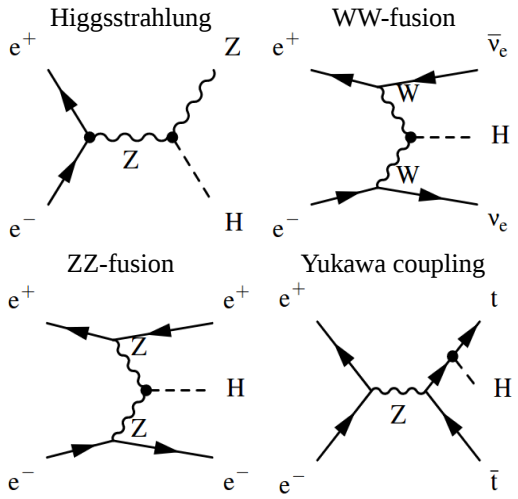

(A) Feynman diagrams

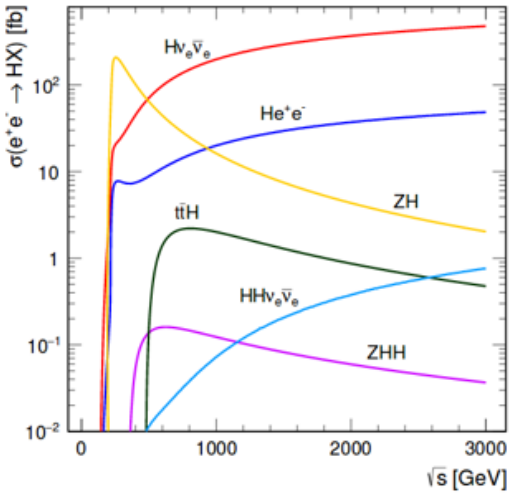

(B) Cross-sections in function of centre-of-mass energy

FIGURE 1.2: Main processes of Higgs production at CLIC [10]. The values for cross-sections (1.2B) shown for unpolarized beams and do not include the effect of the Beamstrahlung.

in Fig. 1.2B showing the cross-section of Higgs processes in function of the centre-of-mass energy $\sqrt{s}$ [10, 13].

1.1.2 Top quark physics

As the top quark is the heaviest elementary particle in the Standard Model (SM) its precise measurements are of a high importance. The mass of the top quark means that it couples the most strongly the Higgs field. The CLIC clean events allow to determine the top quark invariant mass with the precision of about 50 MeV which is significantly higher than allowed by the LHC (several hundred of MeV) [14] and also allow to make top quark threshold scan.

1.2 CLIC experiment concept

The CLIC project comprises a novel two-drive beam accelerating system with single beams interaction point (IP) in the middle of the collider. The length of the accelerator pipe will depend on the energy stage, starting from around 11 km and finishing at around 50 km for the highest energy stage. The cost of first CLIC stage is estimated at 6 to 7 billion CHF [10].

A scheme of the CLIC accelerator complex is shown in Fig. 1.3. The acceleration system proposed for CLIC is an original and innovative approach allowing to obtain very high energies. The 3 TeV beam energy is being achieved using large-gradient accelerating field up to 100 MV m^{-1}. The accelerating gradient for each CLIC stage was already presented in Tab. 1.1. The superconducting cavities cannot be used because of limited maximum intrinsic field for superconductors. Thus, the normal-conducting copper cavities are developed.

As presented in Fig. 1.3, the Drive Beam and the Main Beam are running in parallel. The Drive Beams are powered by 540 klystrons each and are characterized by low energy

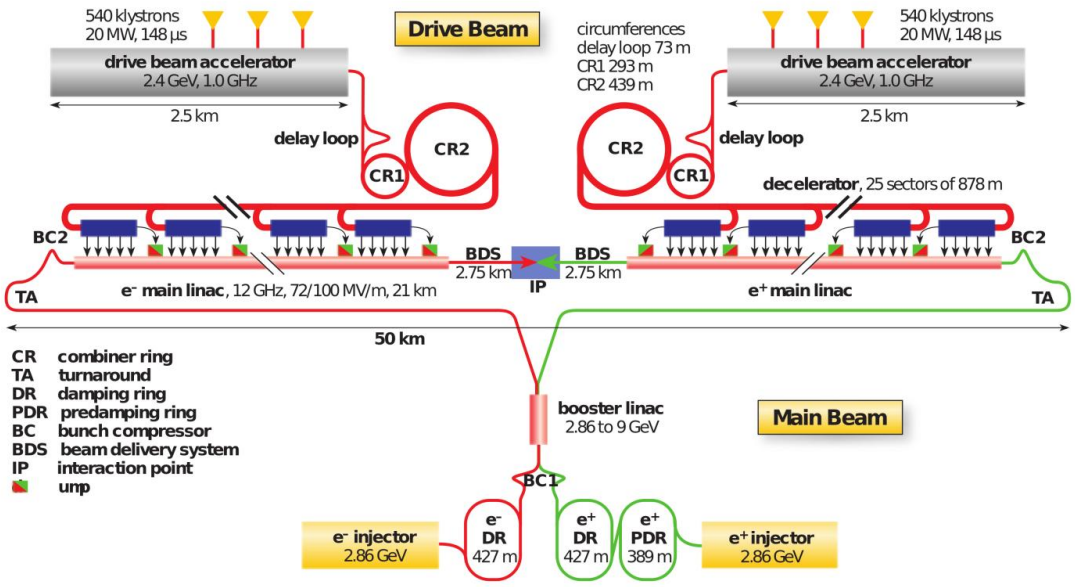

FIGURE 1.3: Idea of the CLIC accelerator system at 3 TeV energy stage [12].

of 2.4 GeV but high current of 100 A. Then the Power Extraction and Transfer Structures (PETS), that are specialized radio-frequency (RF) devices, gain power from the Drive Beam by deceleration and transfer it to the Main Beam which is low current but high energy.

A beam is built from trains of 156 ns length each containing 312 bunches spaced by 0.5 ns [10]. The train repetition rate is 50 Hz, which corresponds to 20 ms time gaps between trains. To obtain a high luminosity of $5.9 \times 10^{34}\,\mathrm{cm}^{-2}\mathrm{s}^{-1}$ the bunches are squeezed to very small dimensions as shown in Tab. 1.1. Due to the high particle density in the bunch, strong electromagnetic interactions occur between bunches as well as particles in the bunches. This effect is known as the Beamstrahlung. The Beamstrahlung effect reduces an available centre-of-mass energy of e^+e^- collisions and causes large background. The particle background consists of hadronic events ($\gamma\gamma \rightarrow hadron$) as well as incoherent e^+e^- pairs which are predominantly produced with low transverse momenta (p_T). This results in pile-up of low energy particles with p_T less than 5 GeV. The pile-up means the situation where a particle detector is affected by several events at the same time, which is undesired effect since hits might be merged. Thus, the beam structure determines the physics-driven detector requirements for the CLIC experiment. In order to limit the influence of background, the timing cuts are needed to be applied. Hits time-stamping on the level of 1 ns to 10 ns for all sub-detectors is essential to separate the desired physics events from the Beamstrahlung effect [15].

The radiation exposure in CLIC is predicted to be about 10^4 less than in the LHC. The Total Ionizing Dose (TID) effects will be smaller than 1 kGy per year in the inner vertex layers [11]. Due to that the radiation damages of main detector elements will be much less compared to the Large Hadron Collider [15].

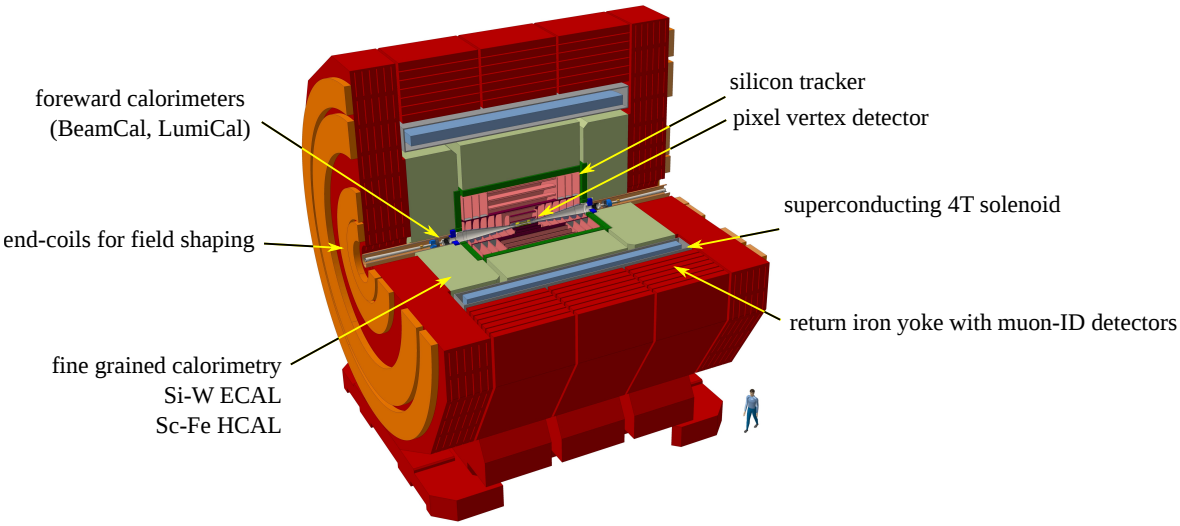

FIGURE 1.4: Graphics of the CLIC detector system [12, 17].

1.2.1 CLIC detectors

The CLIC detector (CLICdet) concept foresees the standard design of complex, general purpose particle detector. The size of the whole system will be 11.4 m in length and 12.9 m in height [16]. The CLICdet is designed as cylindrical system volume built of various detector types as tracking detectors and calorimeters composed in multiple layers, as shown in model in Fig. 1.4. The closest to the interaction point is the vertex detector, planned to be a silicon pixel detector with the excellent timing and space resolution. The vertex detector is surrounded by the tracking system. Then the electromagnetic (ECAL) and hadronic (HCAL) calorimeters provide the information about particles deposited energies. In the forward region there are two smaller calorimeter systems: the Lumical calorimeter (LumiCal) for luminosity measurements and forward beam calorimeter (BeamCal) used for high energy electron tagging. The hadronic and electromagnetic calorimeters are surrounded by superconducting coils generating magnetic field of 4 T. The most outer part is the iron yoke together with muon identification system [9].

Vertex detector

The current project foresees the vertex detector comprising three double layers in barrel ended with the spiral end-caps. The graphical visualization of the vertex detector is shown in Fig. 1.5A. The overall length of the barrel, that is built from staves, is 260 mm. The end-caps are created by flat trapezoids petals arranged in a spiral and in total there are 24 petals per side. The longitudinal distance between the individual petals is 5.5 mm. In radial direction, the petals cover the range from 33 mm to 102 mm. The inner edge of the petals is 28 mm long, the outer edge measures 85 mm and thus an overlap of 2 mm from petal to petal is foreseen [16]. The spiral geometry allows for planned air-cooling, that is chosen in order to limit the material budget since then is no need for colling pipes and coolant.

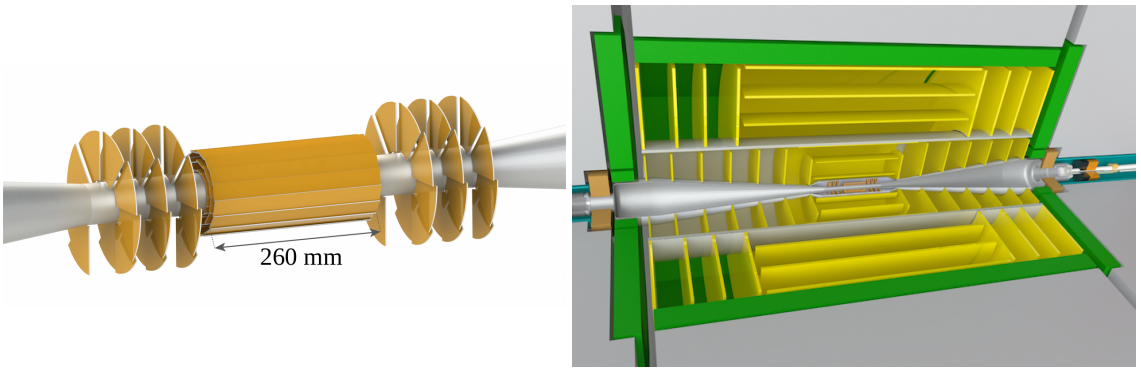

(A) Vertex detector (B) Tracking detector

FIGURE 1.5: Graphical visualization of the CLIC detectors [12].

The vertex is the most inner tracking detector and it provides vertices reconstruction. Accuracy of this procedure determines the flavor tagging capabilities and thus the precise measurement of the impact parameter is needed. The transverse impact parameter d_0 is defined as the closest distance between the reconstructed track and primary vertex. Its resolution $\sigma(d_0)$ is described by the canonical parametrisation as given in Eq. 1.4 [18]:

$$\sigma(d_0) = \sqrt{a^2 + \frac{b^2}{p^2 \sin^3 \theta}} \tag{1.4}$$

where p denotes particle momentum and θ to polar angle. The constant a depends on the point resolution of the vertex detector. The b parameter is related to a multiple scattering and thus it depends on the amount of material in the inner detector and the geometrical arrangement of the layers. The Monte Carlo simulations show that $a \lesssim 5\,\mu\text{m}$ and $b \lesssim 15\,\mu\text{m}$ are required to fulfill physics-driven CLIC demands [9]. Therefore, a single-point resolution of 3 µm for each sensors is desired. The high spatial resolution requirement determines also a pixel pitch not larger than $25 \times 25\,\mu\text{m}^2$.

The limitations for material budget are also derived from the mentioned considerations. Currently, the constraints are 0.2 % of radiation length (X_0) per layer corresponding to 200 µm silicon thickness, including cables, support and cooling system [11]. The background elimination is also important as mentioned in the previous sections. For this reason, the time-stamping capability better than 10 ns is needed [9].

The low material budget limits amount of cooling infrastructure, so the low power consumption of about $50\,\text{mW/cm}^2$ is desired. The long gaps between particle trains (20 ms) allow to introduce power pulsing working mode of readout chips. It is based on switching off parts of the electronics between particle trains [17, 18].

Tracker detector

The tracking detector will be divided into an inner and outer region with separate supports. Each region will consist of three layer barrel. The inner barrel will be enclosed by seven end-cap discs on each side whereas the outer region by four discs as shown in Fig. 1.5B.

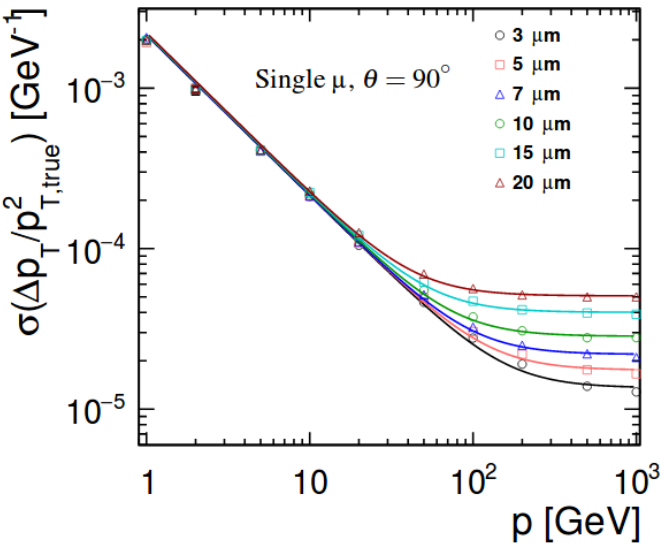

FIGURE 1.6: Transverse momentum resolution for single muons in the CLIC tracking detector as a function of particle momentum shown for various single-point resolutions [19].

For the tracker a single-point resolution of $\sigma_{r\phi} \approx 7\,\mu\text{m}$ is required what comes from the transverse momentum resolution demanding of $\sigma_{p_T}/p_T^2 \approx 2 \times 10^{-5}\,\text{GeV}^{-1}$ [10]. The high accuracy transverse momentum is crucial in terms of physics measurements for example the Higgsstrahlung process. In Fig. 1.6 the simulations from GEANT4 show the transverse momentum resolution for individual muons in the central region of the tracker for different resolutions in the transverse plane of the detector. It can be easily noticed that in order to fulfill the transverse momentum resolution demand, the single-point resolution has to be better than 7 µm [19].

The time-stamping requirements remain the same as for the vertex detector. The occupancy range must be kept in the order of several percent (below 3 %). The total material budget on the level of about 2 % X_0 per layer should be maintained [10]. To achieve this goal, an ultralight carbon fiber support frame is envisaged.

Calorimetry

CLIC requirement for jet (narrow cone of particles) energy resolution is approximately 3.5 %. The basic aim is to improve the jet energy resolution by resolving energy depositions of the individual particles in jet. To achieve this, a high cell granularity and also a precise time information of about 1 ns at the cell level are required. The granularity for ECAL is kept at 5 mm × 5 mm × 2 mm. It uses silicon pad sensors, tungsten absorbers and scintillating tiles with silicon photomultiplier readout. In the hadronic calorimeter granularity of 30 mm × 30 mm × 2 mm and steel absorbers will be used [16].

As it was mentioned earlier, the very forward region consists of two additional calorimeters: the BeamCal and the LumiCal. The BeamCal provides forward tagging of high-energy electrons and delivers fast luminosity estimation. The LumiCal will measure precisely the luminosity value by using Bhabha events at low angles. The LumiCal and BeamCal are

extended to very low angles, covering polar angles from around 39 mrad to 134 mrad and from 10 mrad to 46 mrad, respectively [16].

Muon identification system

The iron yoke is instrumented with muon detection layers. This system is not dedicated for improvement of muon tracking precision. However, it supports particle identification by muon tagging. Moreover, the first layers act as tail catcher for showers developed late in the calorimeters that can slightly improve the energy measurement in HCAL. Another aspect of the muon system is the stand-alone identification and reconstruction of beam-halo muons. This requirement has an impact on the muon system granularity and time resolution. The occupancy and effective muon tagging needs the time resolution of 1 ns as for the calorimeters and cell size of 30 mm $\times$ 30 mm $\times$ 2 mm [9].

1.3 Technologies for the CLIC vertex detector

The all-silicon pixel detector of low material budget is a target for the CLIC vertex detector. Silicon is a dominant semiconductor used currently for position-sensitive detecting devices. Silicon pixel detectors are characterized by high granularity, meaning small sensing cell size. The band gap of 1.12 eV is large enough in comparison to the thermal energy at room temperature (25.9 mV), so the cooling is usually not needed. The minimum ionizing particle (MIP) generates about 90 electron–hole pairs per micrometer [20], thus the detector can be quite thin providing still a good signal in comparison with a gaseous solution. The typical silicon detector thicknesses are presently kept between 50 µm to 500 µm depending on an application and technology [21].

There are several types of silicon pixel detectors that are being intensively developed for high-energy physics experiments. One can distinguish two basic groups in terms of detector structure: hybrid pixel detectors and CMOS-based monolithic systems. In case of the hybrid detectors the readout electronics is soldered with sensors using metal bumps. These detectors show a very good overall performance and they are successfully used in many high energy physics experiments. Nevertheless, the bump-bonding process is burdened with high cost. Furthermore, it introduces an additional material to the detectors causing particle scattering and influencing on spatial resolution achievements. The size of bumps used in soldering is limiting size of the pixel cell, which also has an impact on final detector capabilities. Future physics experiments, such as CLIC, require a low material budget as well as high spatial resolution, which leads to the need of developing alternative solutions that are free of characteristic limitations of hybrid detectors. These competitive solutions are monolithic pixel detectors, where sensor matrix and electronics are fabricated in single wafer. Although the monolithic technologies are currently on the R&D stage, first fully-working prototypes have been already demonstrated, but these are relatively new achievements. Thus, the hybrid pixel detectors are still being developed for future particle physics experiments.

Nowadays, the most promising monolithic solutions are based on CMOS process. CMOS technology is well known, used in industry for commercial applications, what makes it

relatively cheap and easily accessible. Additionally, the CMOS-based detectors are capable to provide good radiation hardness. The example of well developed monolithic devices are MAPS dedicated for STAR experiment [22] or DEPFETs for Belle II [23].

The CLIC vertex detector prototypes are developed using hybrid as well as monolithic structures. The silicon technologies for CLIC are widely described in [21] and [24]. The following paragraph gives a glance through several promising solutions that are currently being developed for CLIC. There are more prototypes that are focused on the CLIC vertex or tracking systems on various stage of progress but only currently the most developed are presented.

1.3.1 Hybrid pixel detectors

As it is mentioned above, hybrid pixel detectors are presently dominating in the pixel detector branch. The pixel size is limited by bumps dimensions, but cells down to 25 µm are still possible to achieve [21]. The detector can be fully depleted, which provides relatively large signal and fast collection time.

Two hybrid concepts are being developed for the CLIC vertex detector with different interconnection method between the sensor and readout chip. The first standard approach is using fine pitch bump-bonding to planar sensors and the second one uses capacitive coupling to high-voltage CMOS (HV-CMOS) sensors.

Both hybrid prototypes incorporate CLICpix2 chip as the readout Application-Specific Integrated Circuit (ASIC). CLICpix2 derives from the Medipix/Timepix family [48] and was fabricated in 65 nm CMOS technology with squared pixels of $25 \times 25\,\mu m^2$ size. Matrix size is 128×128 pixels. The 5-bit Time over Thereshold (ToT) and 8-bit Time of Arrival (ToA) was implemented for each pixel [25]. The pixel was designed to gather both the amplitude and time hit information with the implementation of power pulsing possibility, as well. The final performance studies of CLICpix2 is yet to come up in the nearest future [21].

Planar sensor assemblies

CLICpix2 was bump-bonded to planar n-in-p pixel sensors. One part of the sensors was produced by Micron with a slim-edge design and thickness of 200 µm. The other set of sensors was fabricated by Advacam with an active-edge design with a thickness of 50 µm [26]. Current results show the resolution of about 4 µm at the optimal operation voltage for 200 µm thickness sensor [24]. Achieving a desired resolution on thinner wafer is challenging and measurements are ongoing [25].

Capacitively coupled HV-CMOS sensors

The much more promising solution are capacitively coupled HV-CMOS sensors which form bumpless hybrid pixel detectors [28]. The HV-CMOS maintain the beneficial properties of hybrid detectors and overcome theirs disadvantages as particle scattering on metal bumps and high cost of production. The idea of the capacitively coupled particle detector (CCPD) is to connect the sensor to the readout chip using non-conductive glue and transfer the signal

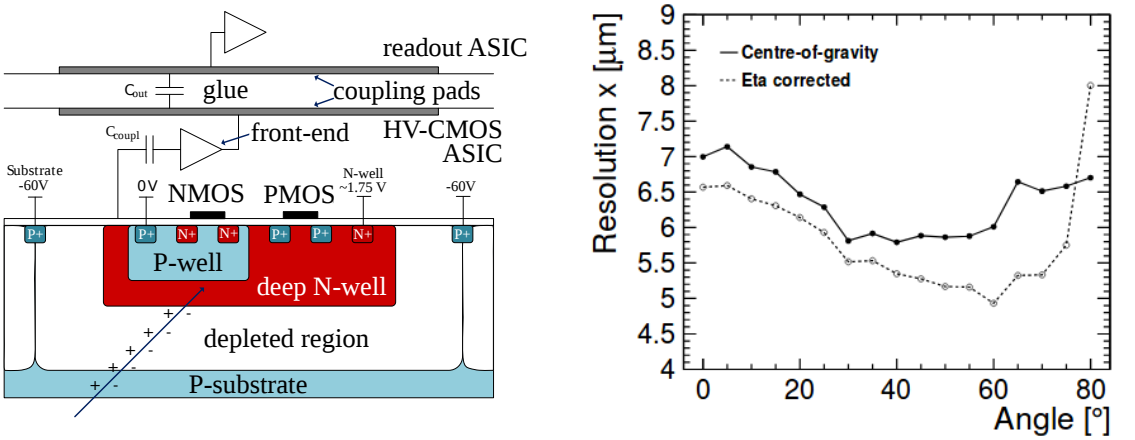

(A) HV-CMOS as a particle detector [27] (B) Single-hit resolution at different angles [26]

FIGURE 1.7: HV-CMOS monolithic pixel detector scheme and exemplary performance results.

capacitively. The main drawback of this solution is that the capacitance between the two chips reduces the signal transfer. Another disadvantage is that the satisfying alignment accuracy of the glued parts is hard to achieve.

The HV-CMOS sensor example is shown in Fig. 1.7A where there are a p-type silicon substrate implanted in a deep n-well. Thus, full CMOS process is available: PMOS transistors are directly implemented in the deep n-well, while for the NMOS transistors the additional p-well is needed. The deep n-well/p-substrate diode acts also as a sensing element. Moderate high voltage is applied in order to deplete part of a substrate volume around n-well (several micrometers). The charge collection comes from drift from the depleted region but also the contribution from undepleted region is significant [25].

For the CLIC vertex detector the CLICpix2 readout chip is glued with CCPDv2 sensor using flip-chip techniques. The glue layer is of a few microns. The pixel is squared with pitch of 25 µm and it is produced on wafer of resistivity of about 20 Ωcm. The first results show 190 mV/ke$^-$ gain and 40 e$^-$ noise with a power consumption of 4.8 µW per pixel [27]. The spatial resolution was measured on beam-test in SPS at CERN in the function of rotation angle of the Device Under Test (DUT) plane. The results are shown in Fig. 1.7B. The single-hit resolution for the 0 angle is 6.5 µm. The 99.8 % efficiency was obtained over the full angular acceptance. The detailed results may be found in [26].

1.3.2 Monolithic High-Resistivity Pixel CMOS Sensors

Comparing to the HV-CMOS structures, in HR-CMOS (High-Resistive CMOS) the electronics is implemented outside the collecting diode. The standard HR-CMOS structure is shown in Fig. 1.8A. Thanks to that a pixel implant is separated from the readout electronics and small sensor capacitance may be achieved. The benefits from small sensor capacitance are mainly larger signal to noise ratio and faster rise time for a given power consumption.

In order to deplete the structure in depth and lateral to the pixels, the back bias voltage is applied to the p-wells. The depleted area is evolving from the pn-junctions around the

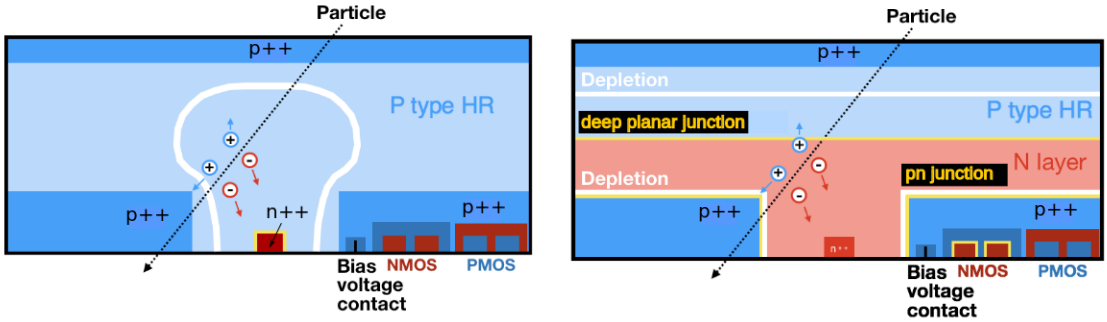

(A) Standard process

(B) Modified process

FIGURE 1.8: HR-CMOS detector schemes [29].

implant and it is growing into the bulk. The pn-junction is also created between n-doped implants of NMOS transistors and p-wells. Thus, applying too high back bias voltage might cause breakdowns. Although the highly-resistive silicon bulk is used to achieve reasonable depletion volume, it is still very challenging to deplete a significant area with such a structure. To achieve a full lateral depletion over the pixel cell, the HR-CMOS process has been modified and a new structure is shown schematically in Fig. 1.8B. The n-type layer is introduced between highly-resistive bulk and the epitaxial layer with electronics and pixel implants. In such a case the pn-junction is created between p-wells and additional n-type layer and between this n-type layer and highly-resistive p-bulk. The area of pn-junctions is much larger than in the standard structure, thus depletion region might grow homogeneously [29].

The Monolithic Active Pixel Sensor called ALPIDE, has been developed in the HR-CMOS technology for ALICE Inner Tracking System. The Investigator chip, that is inheriting from ALIPIDE, is considered currently as a promising prototype mainly for the CLIC tracker detector. It is designed in the Tower Jazz 180 nm technology. The Investigator was produced both in standard and in the modified HR-CMOS process. The measurements of Investigator prototype show 6 µm single-point resolution for 28 µm pixel pitch. The timing resolution is around 5 ns and the efficiency above 99 % [30].

1.3.3 Silicon-On-Insulator technology

The Silicon-On-Insulator (SOI) CMOS technology implements the insulator layer (silicon dioxide – SiO_2) between the highly-resistive substrate and an outer silicon layer, where the CMOS electronics is implemented. The insulator layer is called Buried-Oxide (BOX) and can be applied as a single layer or it can be doubled creating so-called Double SOI (DSOI) structure. The comparison of these two approaches is graphically depicted in Fig. 1.9.

The SOI CMOS technology is currently widely used for commercial applications (for example high-end IBM processors) but it also provides excellent possibilities for fabrication of monolithic pixel detectors for science researches. The highly-resistive substrate can be used for collecting diode implementation with the pixel electronics placed in thin silicon layer above BOX. Since the substrate is separated from the electronics, the structure can be

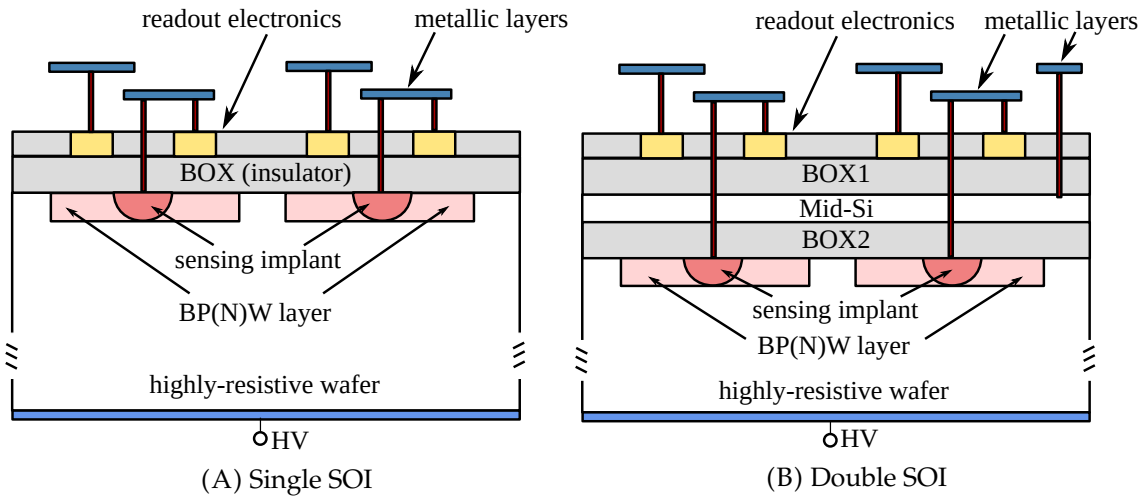

FIGURE 1.9: SOI detector schemes [31].

easily fully depleted allowing for fast and full charge collection. This makes the SOI CMOS technology a promising candidate for particle detectors.

The SOI structures provide a series of benefits in terms of the electronics performance. In the SOI the parasitic capacitances to the bulk are significantly reduced. Due to that there is a possibility to design faster and low-power consuming circuits. The other advantage is a full immunity to the latch-up effects as well as a high suppression of Single Event Effects (SEE), which is achieved thanks to the thin CMOS active layer. Each PMOS and NMOS transistor is separated by BOX layer, therefore no guard rings are needed. This allows to design smaller systems than in the standard CMOS process. The electronics layer is independent from substrate, so a full CMOS process can be used. This is not always the case for other presented monolithic technologies, where full CMOS process is not directly possible or a multiple deep-well technology has to be used.

The SOI technology used for the designs presented in this thesis comes from Japanese Lapis Semiconductor Corporation. The Lapis offers 200 nm Fully-Depleted Low-Leakage SOI CMOS process. Users of the Lapis SOI technology have relatively large possibilities to interfere on a detector design as they can chose type of a substrate wafer from four provided by the company and also design in details a sensor layout using differently doped layers. The thinning of a detector is possible up to 50 µm.

Although it is used by the company for commercial applications, it is also being developed for science purposes. Therefore, the process used for monolithic pixel detectors production shows currently some shortcomings and problems needed to be understood and solved. The KEK scientists, being mostly incorporated in technology development in collaboration with Lapis company, are still doing research on electronics models and overall process performance. Thus, the Lapis 200 nm SOI CMOS technology best performance will be probably achieved only in the near future.

Back-gate effect and BP(N)W layers

One of the major issues connected with the SOI pixel detectors is a back-gate effect. BOX layer is rather thin ($\sim$200 nm) and the high voltage from sensor depletion generates a potential below the insulator which is then acting as a back gate of the transistors. Therefore, the effective threshold voltage of transistors is shifted after biasing the sensor and the circuit would does work correctly. To suppress this effect, the sensing implant is surrounded by the Buried P-Well (BPW) or Buried N-Well layer (BNW), depending on the substrate type. The BP(N)W layer is characterized by higher doping than substrate and it is implemented above any active electronics element. The BP(N)W is set externally to a constant potential, thus this layer shield electronics from the influence of the electric field coming from detector polarization voltage. The disadvantage is that the BP(N)W is increasing the detector capacitance as well as increasing the capacitive coupling between a sensor and electronics.

The other problem that occurs when the SOI is acting as a charged particle detector is radiation hardness. The SEE are significantly limited, because a volume of random charges generation able to switch transistor states is very low. Nevertheless, the TID effects become a dominant issue. Positive charges generated during an ionization are accumulated in the silicon dioxide because of theirs nearly zero mobility. Therefore, the electric field induced by them is affecting transistors threshold voltage. The radiation damages of SOI detectors are the most significant drawback in comparison to other monolithic solutions. Because of that they are currently not suitable for proton and ion colliders. Nevertheless, for lepton accelerator where TID effects are significantly smaller, the upgraded SOI structures, called Double SOI (DSOI), are reasonably considered as candidate for particle detectors.

Double SOI

In DSOI structures two BOX layers are implemented. A scheme of the DSOI is presented in Fig. 1.9B. The problem of back gate effect is solved for this structure type. The silicon layer between BOX layers called Middle-Silicon (Mid-Si) can be set on a constant potential preventing structure from this negative effect.

As in the case of back-gate effect, the DSOI structure shows a potential for better radiation hardness than the single SOI. When the electronics suffer from irradiation, a correction potential may be applied to the Mid-Si to alleviate undesired influence of BOX positive potential on transistors threshold voltage. The tests of the single SOI and DSOI in terms of radiation hardness for particle experiments are ongoing and are promising [32]. Although the DSOI provides several improvement over standard single SOI structure, its fabrication is more challenging.

Comparison with other monolithic technologies

One of the biggest advantage of the SOI detectors in comparison with other solutions developed for the CLIC vertex detector is that there are no constrains put on choosing substrate and electronics wafers. Each of them can be selected separately and tailored to the particular demands. Thus, choosing a highly-resistive wafer for sensor matrix and low-resistive

wafer for electronics is possible as for the hybrid detectors. Moreover, the SOI structure does not need bump-bonding, which reduces significantly the detector material budget. Lower material budget translates to smaller multiple particle scattering and therefore much better detector performance. The detector production basing on bump-bonding or flip-chipping is complex and time-consuming, leading to additional production steps. This makes the process expensive. The accuracy of bump-bonding, especially for small pixels is also challenging, thus a significant part of the fabricated prototypes are not suitable for application in experiment. The SOI shows significantly higher production yield than hybrid solutions and at the same time benefits using two different wafer types for sensors and electronics.

The most desirable advantage of the SOI over the HV-CMOS and HR-CMOS is a possibility of achieving the full depletion. Thanks to that, the signal is large and charge collection is fast. The depletion of the HV-CMOS sensors is usually limited by the resistivity of the bulk. In addition, since the electronics for the HV-CMOS is placed in the collection diode, the detector capacitance is relatively large. On the other hand, for the HR-CMOS a highly-resistive substrate is used and the sensing node is small, but it is still hard to develop the depletion volume. Even in modified process the depletion region is very shallow, leading to small signal. This is not the case for the SOI detectors, which can be easily fully depleted. There is also no limitation for pixel size in the SOI, which depends only on amount of electronics that has to be placed in the pixel readout.

A meaningful benefit regards also the in-pixel electronics performance. Since the SOI is a commercial technology it offers the full CMOS process and as explained earlier the performance of these circuits is comparable or better in comparison with the standard CMOS circuities. Since for the HV- and HR-CMOS detectors electronics is placed in the same wafer as sensing nodes, that generates more constrains and complications in electronics design and limits final performance.

There are various examples of already developed SOI Lapis 200 nm detectors showing excellent performance. For example the FPIX detector presents the best ever achieved spatial resolution, going below 1 µm for 8 µm squared pixels [33]. The SOFIST detector prototype, dedicated for the ILC, is showing spatial resolution of 1.2 µm (on 200 µm wafer) and around 2 ns time resolution (on 65 µm wafer) with 20 µm squared pixels [34]. Such a performance is currently hard to obtain using other monolithic or hybrid technology. Thus, the SOI CMOS seems to be promising candidate for the CLIC vertex detector and for other demanding particle detectors.

Chapter 2

Working principles of semiconductor tracking detectors

The particle detection is possible because of its interactions with a medium. These interactions can be simply divided into two basic types: the charged particles interactions such as interactions of electrons, muons or ions and neutral particles interactions, for example photons or neutrons. The knowledge of physics standing behind these phenomenons is crucial for understanding particle detectors working principles.

The choice of a detector type mainly depends on its application, especially on information that has to be obtained from a measurement. The analyses presented in this work regards the performance of solid state silicon prototypes dedicated for tracking purposes. Silicon detectors are characterized by a high density and a large energy loss over a short distance. Low ionization energy (few electronvolts per electron–hole pair) in comparison to gaseous detectors (several tens of electronvolts per electron–ion pair) provides relatively large signal from a single ionizing particle. Also the resistance for irradiation is satisfactory, since the deep-submicron CMOS technologies that are used for these devices are characterized by good radiation hardness. This is especially important for experiments with huge total ionizing dose as hadron colliders. All mentioned features make silicon detectors highly competitive in comparison to other solutions.

The design of particle detector has to be optimized in terms of its application. Since the requirements coming from future high energy experiments are demanding, very often the detector has to show a high precision performance in more than one field. For example for tracking purposes the spatial resolution is the most important whereas for calorimeters the energetic resolution. However, for CLIC the fine timing resolution is required for all detector types, as well as ultra-low power consumption. This makes the particle detector design a challenging work.

2.1 Charged particle interactions with matter

Two processes are dominant for charged particle interactions. The first one is excitation, when electron is pushed into higher shell and the second one is ionization when electron is completely removed from an atom. A projectile can also interact with a nuclei but this process is quite rare. For relativistic particles the energy loss may also happen by the

Bremsstrahlung phenomenon, that is electromagnetic radiation produced by the deceleration of the charged particle.

2.1.1 Maximum kinetic energy

The large contribution to particle energy losses comes from ionization. One can designate the maximum kinetic energy $T'^{\max}_e$ that can be transfered in collision of the projectile of momentum p with an electron at rest. The total initial energy E of incident particle is defined as:

$$E = \sqrt{p^2c^2 + m^2c^4} = T + mc^2 \tag{2.1}$$

where:

c — the speed of light

$p = \gamma m\beta c$ — projectile momentum, where $\gamma = \frac{1}{\sqrt{1-\beta^2}}$ is the Lorentz factor and β is defined by particle velocity $v = \beta c$

m — projectile mass

T — projectile kinetic energy

The above equation is applied into the energy conservation relation of considered case:

$$\sqrt{p^2c^2 + m^2c^4} + m_ec^2 = \sqrt{p'^2c^2 + m^2c^4} + T'_e + m_ec^2 \tag{2.2}$$

where prime symbol is used for variables in the final state (after collision), so p' is the projectile final momentum and T'_e is electron final kinetic energy. Basing on momentum conservation and the law of cosines, the p'^2 is:

$$p'^2 = p^2 + p'^2_e - 2pp'_e\cos\theta \tag{2.3}$$

where θ is an angle between the projectile initial momentum $\overrightarrow{p}$ and the electron momentum after collision $\overrightarrow{p'_e}$. Merging eqs. (2.1) to (2.3) with the condition of $\cos\theta = 1$ one can designate the maximum transferable kinetic energy $T'^{\max}_e$:

$$T'^{\max}_e = \frac{2m_ec^2\beta^2\gamma^2}{1 + 2\frac{m_e}{m}\gamma + \left(\frac{m_e}{m}\right)^2} = \frac{2m_ep^2}{m^2 + m_e^2 + 2m_e\frac{E}{c}} \tag{2.4}$$

Very often Eq. 2.4 is considered for two important cases when the incident particle is heavier than electron ($\frac{m_e}{m} \ll 1$) and when the incident particle is an electron ($\frac{m_e}{m} = 1$). For heavy particle the quadratic term $\left(\frac{m_e}{m}\right)^2$ in denominator of Eq. 2.4 can be neglected [20]:

$$\text{heavy} \rightarrow \quad T'^{\max}_e = \frac{p^2}{\frac{m^2}{2m_e} + \gamma m} \tag{2.5}$$

Furthermore, the approximation for low energy particles might be done, which is useful in the Bethe-Bloch relation considered later in this chapter. Low energy particles corresponds

practically to that $2\gamma m_e \ll m$ [35] and then relation becomes as follows:

$$\text{heavy, low energy} \rightarrow \quad T'^{\max}_e \approx 2m_e c^2 \beta^2 \gamma^2 \tag{2.6}$$

The next considered case is an relativistic heavy particle for which the total energy is approximately equal to kinetic energy ($E \approx pc$). Applying this approximation into Eq. 2.5, the relation for heavy relativistic particles is given by [20]:

$$\text{heavy, relativistic} \rightarrow \quad T'^{\max}_e \approx \frac{E^2}{\frac{m^2c^2}{2m_e} + E} \tag{2.7}$$

Considering the denominator of Eq. 2.7, there is a special case ($\frac{m^2c^2}{2m_e} \ll E$) when almost all incident particle energy can be transferred to a single electron. However, the energy is mainly transferred in many ionization processes [20].

If the incident particle is an electron, the condition of $m = m_e$ is put into Eq. 2.4 and finally the relation is the same as for central collision of equal masses for classical non-relativistic case:

$$\text{electron} \rightarrow \quad T'^{\max}_e = E - m_e c^2 \tag{2.8}$$

2.1.2 Bethe-Bloch formula

The important relation in terms of particle interactions with matter is the Bethe-Bloch formula known also as stopping power relation [35]:

$$\left\langle -\frac{\mathrm{d}E}{\mathrm{d}x} \right\rangle = Kz^2 \frac{Z}{A} \frac{1}{\beta^2} \left(\frac{1}{2} \ln \left(\frac{2m_e c^2 \beta^2 \gamma^2 T'^{\max}_e}{I^2} \right) - \beta^2 - \frac{\delta(\beta\gamma)}{2} \right) \tag{2.9}$$

where:

$K = 4\pi N_A r_e^2 m_e c$ — coefficient for $\frac{\mathrm{d}E}{\mathrm{d}x}$, where r_e is the classical electron radius and N_A is Avogadro number

z — charge number of incident particle

Z — atomic number

A — mass number

$I = 16Z^{0.9}$ — mean excitation energy

$\delta(\beta\gamma)$ — density effect correction to ionization energy loss

$T'^{\max}_e$ — maximum transferable electron energy from Eq. 2.6

The Bethe-Bloch formula uses approximation given in Eq. 2.6 thus it describes the mean rate of energy loss by moderately relativistic charged heavy particle. The given formula works fine for the mean rate of energy loss in the region $0.1 < \beta\gamma < 1000$ for intermediate-Z materials. However, it does not include all effects, such as large angle multiple scattering or Cherenkov radiation. Exemplary relation of mean energy losses for different particles in various medium is shown in Fig. 2.1.

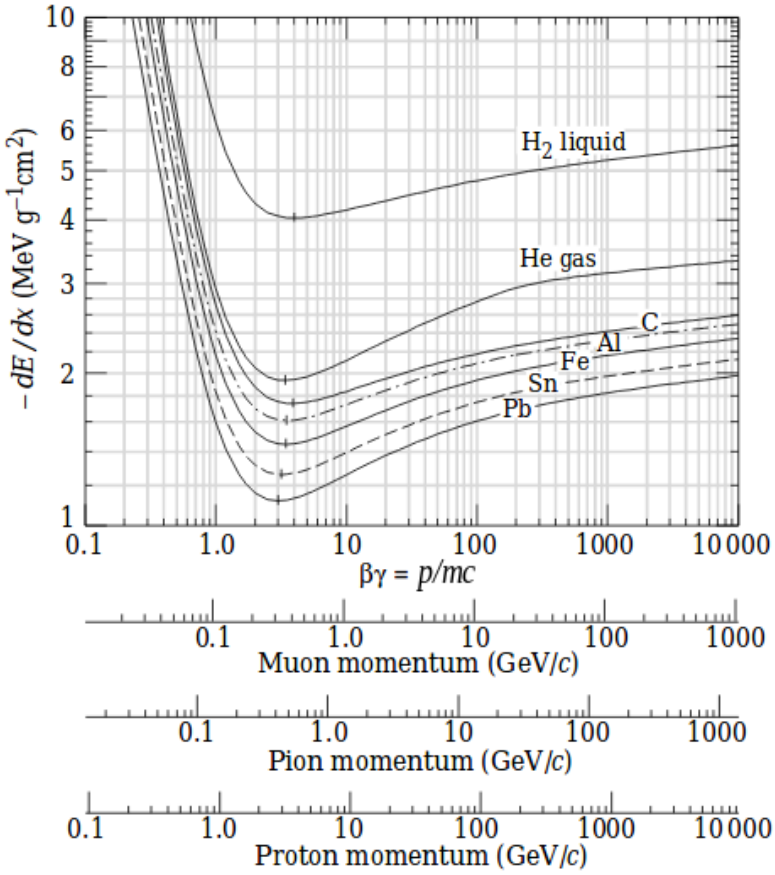

FIGURE 2.1: Mean energy loss rate in liquid (bubble chamber) hydrogen, gaseous helium, carbon, aluminum, iron, tin, and lead. Radiative effects, relevant for muons and pions, are not included. These become signicant for muons in iron for $\beta\gamma > 1000$ and at lower momenta for muons in higher-Z absorbers. The plot is orginal work from [36].

The definition of minimum ionizing particle (MIP) also comes from interpretation of $\left\langle -\frac{\mathrm{d}E}{\mathrm{d}x} \right\rangle$ function and it describes a particle for which mean energy loss is close to the minimum. For example for silicon the mean energy loss of MIP is around 1.6 MeVg^{-1}cm^2 [35]. The Bethe-Bloch formula given as in Eq. 2.9 is not valid for electrons. The relation for kinetic energy should be replaced according to Eq. 2.8. In addition, effects that are not common for heavy particles should be included, such as mentioned before large angle multiple scattering or Cherenkov radiation.

2.1.3 Landau-Vavilov distribution

The delta electrons or knock-on electrons, are the orbiting electrons that are knocked out of atoms. Such delta electrons have enough energy to ionize other atoms in a medium. Due to that the knock-on electrons are often a limitation for position and energy measurement, because delta electrons introduce large fluctuations into energy loss dependence. In practice, particle collisions in the medium are stochastic and considering the energy loss distribution is more practical approach than the mean energy loss from the Bethe-Bloch formula. The Landau distribution (also known as Landau-Vavilov) describes energy loss of particle

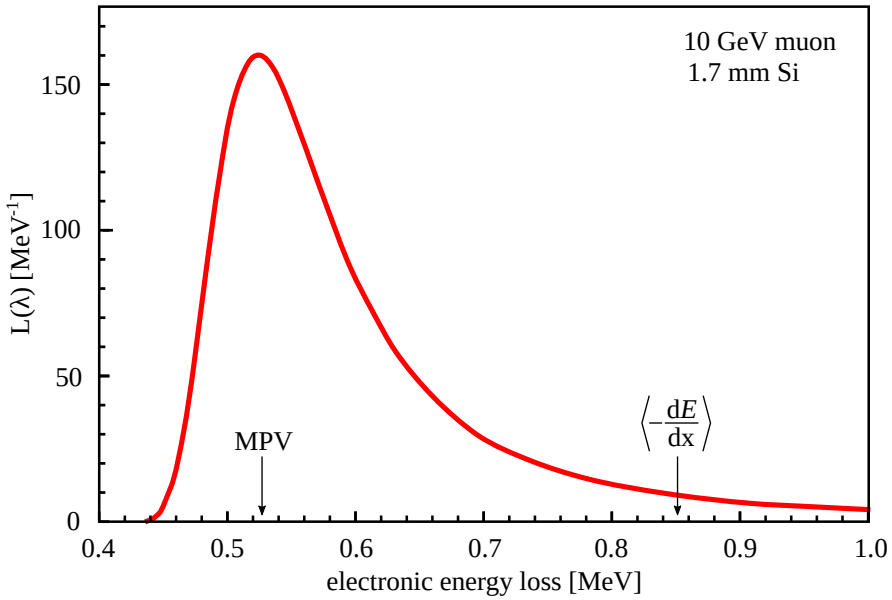

FIGURE 2.2: Landau function of energy deposit distribution. *MPV* is the most probable energy loss from Landau and for comparision the Bethe-Bloch $\left\langle -\frac{\mathrm{d}E}{\mathrm{d}x} \right\rangle$ divided by the detector thickness is shown [35].

traversing by the medium, taking into account possible fluctuations [37]. The approximation of Landau distribution is given by:

$$L(\lambda) \quad = \quad \frac{1}{2\pi} e^{-\frac{1}{2}(\lambda - e^{\lambda})} \tag{2.10}$$

where λ characterises the deviation from the most probable energy loss [20]. The example of Landau function of energy deposit distribution is presented in Fig. 2.2. The most probable value (MPV) of Landau distribution is always smaller than the average energy loss from the Bethe-Bloch considerations as shown in the example. The Landau distribution is good approximation for moderate thickness detectors (the definition of moderate thickness is in details considered in [38]). In case of experimental data, most often the Landau convolution with Gaussian function is fitted to energy deposit distribution since in true experiment the Gaussian-distributed noises contribute to the signal.

2.2 Silicon particle detectors

Silicon is nowadays a very desirable material used for various applications. It is widely used not only in science, but especially in industry, what makes this material easily available, very well developed and relatively cheap. Since the silicon detectors are comprising good performance with low costs of production, they become a most popular solution for the high-energy particle physics experiments.

The MIP particle is generating about 90 electron–hole pairs per micrometer of silicon [20] what provides relatively large signal. Also the time response of silicon detectors is very

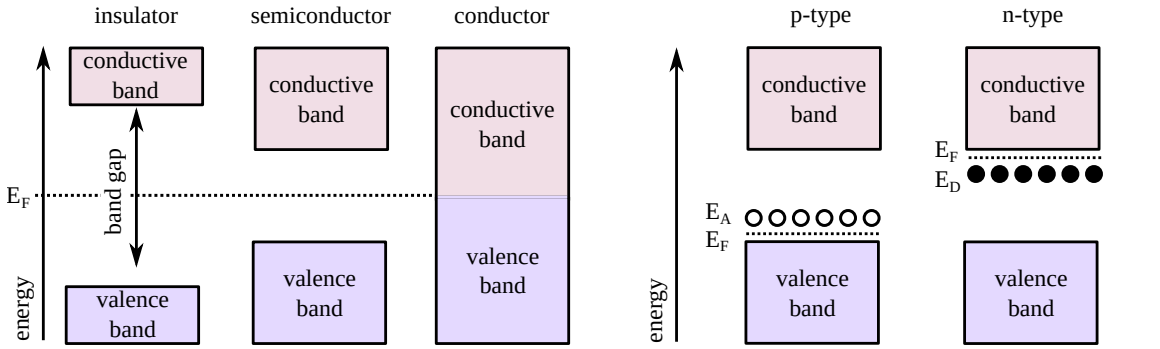

(A) Insulators, semiconductors and conductors (B) n-type and p-type doped semiconductors

FIGURE 2.3: Simplified energy band schemes. E_F is the Fermi level defined as the last occupied energy level at $T = 0\,\mathrm{K}$. The accpetor band E_A is an extra hole energy level and the donor band E_D an extra electron energy level.

good in comparison to other solutions. Because of these reasons silicon solid state detectors are very good systems for high energy particle physics experiments.

2.2.1 Semiconductor physics overview

Silicon is a semiconductor material of electrical conductivity between conductors and insulators. The scheme of energy bands for these three material types are presented in Fig. 2.3A. Both for insulators and semiconductors the electron has to excite into conducting band to become conductive. The size of the band gap depends on the material and for silicon it is 1.12 eV.

The conductive properties of intrinsic (pure) semiconductors can be easily changed by doping. Doping is simply introducing impurities to pure silicon crystal lattice. Since silicon is in the group-IV of the Mendeleev Table, it has four valence electrons which bond silicon atom with four neighbouring ones. Doping the intrinsic semiconductor with element from a higher group introduces additional electron. These doping atoms are called donors. Such a procedure is introducing additional energy band (shallow donor band) which is located just below conduction band. When the additional electron is excited, what is easy because of the small distance of the conductive band to shallow donor band, donor atom becomes a positive ion. The donor element for silicon is for example phosphorous belonging to group-V. The silicon may be also doped using the element from lower group as for example boron. This introduces shallow acceptor state close to the valence band. The lack of electron is effectively an additional hole carrier. The dopant is thus called acceptor. The scheme of energy bands for these two cases are graphically shown in Fig. 2.3B. The dopant type determines which carrier are dominant in the material (majority carriers), thus donors creates n-type semiconductors and acceptors p-type.

2.2.2 Charge transport in silicon

The charged particle passing through detector volume generates electron–hole pairs being the free charge carriers. The signal formation in silicon detectors is determined by the charge

transport in the active volume. The charge transport may be caused by diffusion or drift phenomenon.

The drift is a movement of charge carriers driven by external electric field. The drift velocity v_d is calculated as:

$$\overrightarrow{v_{\text{drift}}} = \mu_{e,h} \cdot \overrightarrow{E} \tag{2.11}$$

where $\mu_{e,h}$ is carrier mobility of electrons (e) or holes (h) and $\overrightarrow{E}$ is external electric field.

The drift velocity saturates since the number of particle collisions in time increases with increase of the electric field. The relation between electron drift velocity versus electric field is presented in Fig. 2.4A. The carrier mobility μ depends on the temperature and donor density. The example of μ_e relation versus doping concentration for different temperatures is presented in Fig. 2.4B. For calculations one can usually take the approximate value of holes mobility of about $480\,\text{cm}^2\text{V}^{-1}\text{s}^{-1}$ and $1415\,\text{cm}^2\text{V}^{-1}\text{s}^{-1}$ for electrons at an room temperature and doping density below $10^{16}\,\text{cm}^{-1}$ [39, 40].

The diffusion describes random movement of the charge carriers. In equilibrium state the averaged displacement of the carriers is zero. In silicon the diffusion movement is determined by the carriers gradient and electrons or holes move from high-concentration to low-concentrations region. Thus, the diffusion current inverse to the charge carrier gradient is created. According to diffusion phenomenon one may also define free path length parameter that is an variable describing the mean path between the scattering. For silicon this value is around 0.1 µm.

The diffusion phenomenon smears also the trajectories of carries drifting towards electrodes by the external electric field influence. When the trajectories are perpendicular, one can assume the diffusion cloud to be a Gaussian shape. The standard deviation of this cloud is given by Eq. 2.12:

$$\sigma_{\text{diff}}(d) = \sqrt{2D_{e,h} \cdot t_{\text{drift}}(d)} \tag{2.12}$$

$$D_{e,h} = \frac{kT}{q} \cdot \mu_{e,h} \tag{2.13}$$

where:

d — distance traveled by carries within detector volume

$D_{e,h}$ — diffusion coefficient defined with the Einstein relation

$t_{\text{drift}}(d)$ — drift time on d distance

T — absolute temperature

k — Boltzmann constant

Let us asses the size of diffusion cloud at the sensing implants level ($d = 0$) for the charges generated near the back plane ($d \to D$, where D is wafer thickness). The considered example is the SOI detector prototype presented in this work. Further measurements show that the full depletion voltage for the 500 µm thick FZ-n SOI wafer is achieved for the back bias voltage of $V_D = 70\,\text{V}$. The drift velocity from Eq. 2.11 and thus drift time depends on the external electric field $E(x)$. Relations for electric field and approximate value of maximum

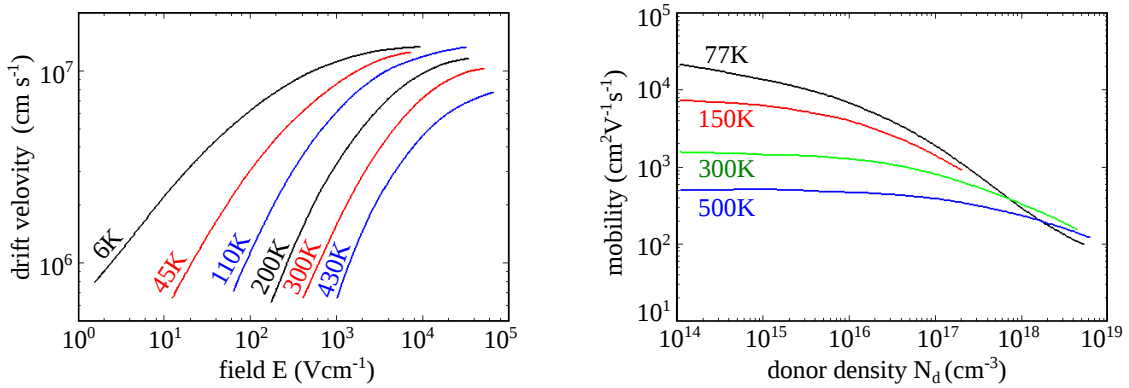

(A) Drift velocity in function of the electric field [42].

(B) Carriers mobility in function of doping concentration [39].

FIGURE 2.4: Selected electron carrier properties in silicon for different temperatures.

electric field in reversely biased pn-junction are taken from [41]:

$$E(x) = E_{\max}\left(1 - \frac{x}{D}\right) \tag{2.14}$$

$$E_{\max} \approx \frac{2V_D}{D} \tag{2.15}$$

Using above approximations, one can extract the final relation for drift time and diffusion cloud as follows:

$$t_{\text{drift}}(d) = \int_0^d \frac{1}{v_{\text{drift}}(x)}\mathrm{d}x = \int_0^d \frac{D}{2V_D\mu_e}\left(\frac{D}{D-x}\right)\mathrm{d}x \tag{2.16}$$

$$\sigma_{\text{diff}}(d) = \sqrt{\frac{kT}{q}\cdot\frac{D^2}{2V_D}\cdot\ln\left(\frac{D}{D-d}\right)} \tag{2.17}$$

Let us estimate the diffusion cloud on the level of 99 % of overall detector thickness ($d = 99\%D$). The $\sigma_{\text{diff}}(0.99D)$ is thus around 15 µm.

2.2.3 pn-junction

The pn-junction is created between the n-type and p-type semiconductor. Graphical scheme of pn-junction is depicted in Fig. 2.5. The electron carries from n-type silicon diffuse into p-type silicon and there recombine with holes canceling each other out. The same situation happens for holes diffusing from p-type silicon to n-type. The remaining ions are part of the crystal and are not moving as depicted schematically in Fig. 2.5. Those ions create so-called space charge region (SCR) and built-in electric field occurs. The electric field forces charge movement of opposite direction than this caused by diffusion. Thanks to that the equilibrium state is achieved. The built-in potential V_{bi} depends on the doping levels of extrinsic semiconductors:

$$V_{bi} = \frac{kT}{q}\ln\left(\frac{N_a N_d}{n_i^2}\right) \tag{2.18}$$

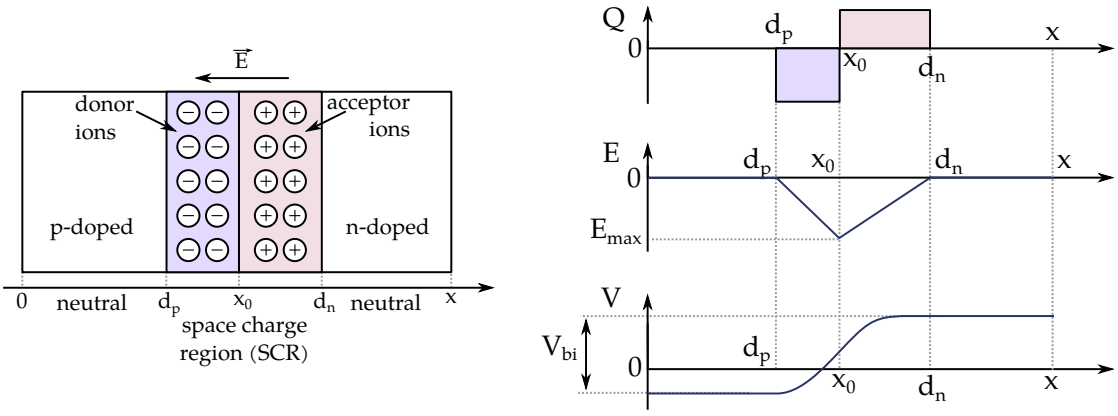

FIGURE 2.5: pn-junction scheme with schematic diagram of charge (Q), electric field (E) and electric potential (V) distribution across the junction.

where N_a and N_d are acceptor and donor concentrations and n_i is the intrinsic silicon concentration, which is approximately $1.45 \times 10^{10}\,\mathrm{cm}^{-3}$ in room temperature.

A pn-junction creates a diode, one of the basic circuit elements that allows one-direction current flow. The SCR region between the p-type and n-type is called a depleted area since it is free from mobile charges. Applying the external voltage to the pn-junction in forward direction causes the decrease of the depleted area and when the applied voltage is high enough the current may flow through the junction freely. When the voltage is applied in direction of the built-in potential, the diode is reversely biased and then the depletion region grows.

The reverse biased pn-junction acts as a basic model of particle detector. The charges generated by ionization in the depleted area drift to the electrodes and form a signal proportional to the induced charge. The electron and hole movement is just the opposite direction and depends on the bulk type. For n-type bulk holes are collected by the sensing node and electrons by the backplane and inversely for p-type silicon.

2.2.4 Full depletion voltage

For MIP particles, the larger is the depleted volume, the higher is the generated signal. The depletion area width d depends on the back bias voltage V_d (also called as reverse bias voltage, polarization voltage) and silicon resistivity ρ_d as follows [43]:

$$d = \sqrt{2\epsilon_s V_d \mu_{e,h} \rho_d} \tag{2.19}$$

where ϵ_s is semiconductor permittivity. Assuming as previously that D is the total sensor thickness, one can define the full depletion voltage as V_D which allows to deplete the entire detector volume:

$$V_D = \frac{D^2}{2\epsilon_s \mu_{e,h} \rho_d} \tag{2.20}$$

The pn-junction acting as a particle detector behaves as a capacitor with the depleted volume acting as a dielectric. The pn-junction capacitance C_{pn} formed under reverse bias

condition is equal to:

$$C_{pn} = \frac{\epsilon_s A}{d} \tag{2.21}$$

where A is device contact area [36]. Minimizing the detector capacitance is an important issue, since the signal amplitude may depend inversely proportional from C_{pn}. Thus, the technologies allowing to fully deplete the sensor are of the major importance, because the pn-junction capacitance is inversely proportional to depletion width d [43].

For partially depleted structures one has to study the influence of charges coming from undepleted volume. The charges induced in undepleted region tend to collide with the other carries causing their scattering. The life-time of these charges is relatively short, because they recombine with each other. Theoretically, they should not contribute significantly to the signal gathered on electrodes. However, it is not obvious since for example the life-time of charges in non-depleted region depends on the doping of the wafer. Thus in a specific conditions it might happen that the contribution of charges from undepleted region can be significant.

2.3 Detection chain

Depending on the application of the detector, there are various options for readout electronics. In very general approach, the charge has to be converted into the voltage signal which can be further amplified, shaped and digitized. Furthermore, also depending on the architecture, zero suppression can be done, that is removal of events below some threshold. The signal might be sent out in a raw analouge form or as a digitalized signal what is more preferred and practiced solution for well-developed systems.

Two different strategies might be chosen in terms of output information type. The first one, called binary readout, gives only an information if the pixel/strip was hit or not. There is a discriminator implemented in the readout electronics that is sensitive on signal above some threshold value. Thus, in case of this readout type the output is binary (one or zero). The other approach is to send out the measured amplitude value. Still, a discrimination of the signal might be implemented, but in this case there is an information about how much signal was collected on pixels/strips that fired. In this work, the data analysis comes from detectors implementing the second approach.

Two most popular approaches of input stage readout electronics architectures are presented in Fig. 2.6. In first of them is a buffer and the second one is a charge-sensitive amplifier. Both of these designs are implemented in detector matrix presented in this thesis, thus their brief analysis is introduced below.

In Fig. 2.6A a scheme of voltage buffer with unity amplification is shown. The typical example of buffer architecture is so-called source follower, which is a single transistor amplifier in a common-drain topology. The source follower benefits in a simple architecture and hence a limited number of electronic noise sources. The voltage at the buffer input is

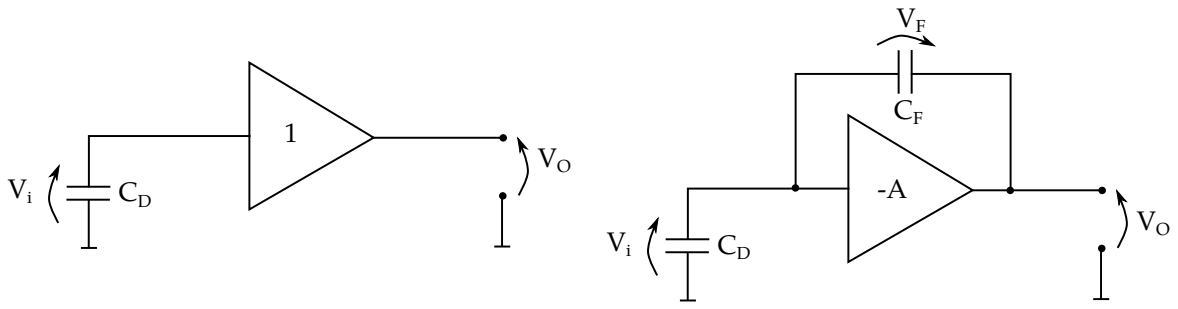

(A) Buffer implementation (B) Charge-sensitive amplifier implementation

FIGURE 2.6: Schemes of signal integration electronics types [20].

then given by:

$$V_i = \frac{Q_i}{C_D + C_i} \sim \frac{1}{C_D} \text{ for } C_i \ll C_D \tag{2.22}$$

where Q_i denotes to collected charge, C_i is input capacitance and C_D is detector capacitance. Assuming that input capacitance is significantly smaller than detector capacitance, which should be the case for well done design, the voltage V_i is inversely proportional to C_D. This is a common case for example for strip detectors where the C_D is relatively large. However, in general case the signal V_i for this architecture is inversely proportional to the total capacitance ($C_T = C_D + C_i$) seen from the input node.

The other approach of front-end electronics is the charge-sensitive amplifier. It is shown schematically in Fig. 2.6B. Typically, in this readout type an inverting amplifier with amplification $-A$ and feedback capacitor C_f is implemented. The charge-sensitive preamplifier output voltage V_o is:

$$V_o = -A\frac{Q_i}{C_D + C_f(A+1)} \tag{2.23}$$

This architecture allows to alleviate the problem of signal dependence on detector capacitance. Assuming that the amplification A is large enough and $A \cdot C_f \gg C_D$, the Eq. 2.23 may be simplified to Eq. 2.24. Thus, the input charge to output voltage conversion ratio A_Q is defined by Eq. 2.25.

$$V_o \simeq -\frac{Q_i}{C_f} \tag{2.24}$$

$$A_Q \simeq \frac{\mathrm{d}V_o}{\mathrm{dQ_i}} = -\frac{1}{C_f} \tag{2.25}$$

Contrary to the first approach the output signal depends on the feedback capacitance and not on detector capacitance.

The idea of implementing pixels containing both mentioned architectures was driven by the fact that Lapis SOI technology offers different silicon wafer types as single and Double SOI (as described in Sec. 1.3.3 on page 15). The charge-sensitive amplifier architecture was planned to be universal pixel type for both wafer types. On the other hand, the source

follower signal is dependent on detector capacitance, thus this readout was rather dedicated for single SOI because its detector capacitance is much lower than the DSOI. Nevertheless, a simple architecture of source follower was expected to benefit in lower noises and thus a good final performance.

2.3.1 Electronics noise

Noise refers to a stochastic process, that usually is an unwanted effect that influence on a true signal. In case of particle detectors the measured signal is distorted by statistical effects as fluctuations of a number of generated charges. However, a dominant noise contribution comes usually from the electronic noises of in-pixel readout and any other post-processing circuit.

Various types of noise are generated by different electronic elements and different processes are standing behind them. As the most common, one can mention thermal noise, shot noise and 1/f noise. The first one is caused by the velocity fluctuations of charges in conductor. The shot noise and 1/f come from fluctuations of number of carries. Detailed noise analyses are beyond the scope of this dissertation. Nevertheless, from the practical point of view the terms of Equivalent Noise Charge (ENC) and signal to noise ratio (SNR) are useful in further considerations. The ENC gives noise value in charge units, which is very useful in case of noise comparison for charge-sensitive detectors. Since both the signal and noise levels depend on the detector type and electronics architecture, the more conclusive is to consider the SNR than the absolute values of signal or noise. The good SNR performance is one of the crucial parameter of a detecting system. Usually, it is assumed that signal should be at least few times larger than noise value. In general, the large SNR is a guarantee for good performance of the device.

2.4 Properties of tracking detectors

The detector technology, sensor design as well as pixel front-end electronics influence on final detector performance. Depending on the application the overall design is focused on optimization of the chosen set of parameters. The resolution is a major figure of merit of the detecting devices. It describes the accuracy of various quantities reconstruction, such as position, energy, momentum or time. Also the efficiency of the detector is of the high interest.

2.4.1 Efficiency

The detector efficiency is the ratio of a number of particles reconstructed by the DUT to all particles passing through its volume:

$$\text{efficiency} = \frac{\text{number of reconstructed particles}}{\text{number of all particles}} \tag{2.26}$$

Since the real number of all particles is usually not known, the reasonable reference has to be chosen to calculate the device efficiency. For test-beam measurements the reference sample is the track data set coming from telescope.

There are many effects that may influence on efficiency, for example hits pile-up or readout-connected issues. Especially the dead time of the detector is of the major influence. It is defined as a time when the detector is insensitive for particle detection or readout is not able to process and save the event. The hits coming during detector dead time are lost, decreasing the final efficiency.

2.4.2 Spatial resolution

Let x be a continuous physical quantity measured N times. A distribution of x from N measurements is denoted as $P(x)$. An expectation value μ_x and a variance ν_x of the x quantity are given by Eq. 2.27 and Eq. 2.28 respectively.

$$\mu_x = \int_{x_{min}}^{x^{max}} xP(x)\,\mathrm{dx} \tag{2.27}$$

$$\nu_x = \int_{x_{min}}^{x^{max}} (x-\mu_x)^2 P(x)\,\mathrm{dx} \tag{2.28}$$

The basic approach of measuring quantity x resolution is to calculate standard deviation σ_x which is simply square root of variance:

$$\sigma_x = \sqrt{\nu_x} \tag{2.29}$$

For discrete probability distribution of quantity x, the standard deviation for finite number N of measurement samples is defined as:

$$\sigma_x = \sqrt{\frac{1}{N}\sum_i^N (x_i-\overline{x})^2} = \sqrt{\overline{x^2}-\overline{x}^2} \tag{2.30}$$

where $\overline{x} = \frac{1}{N}\sum_i^N x_i$ is the mean value of x and $\overline{x^2} = \frac{1}{N}\sum_i^N x_i^2$ is the mean of x^2.

The spatial resolution of a pixel detector may be considered for binary systems, where only the pixel pitch influences on the final result or for the systems characterized by charge sharing effect. For the last one the analysis of energy distribution over pixels may improve significantly the final performance.

As it was mentioned earlier, for the binary readout the threshold for signal extraction is set in such a way, that pixel fires or not and no other information is gained from the measurement. In such a case the $P(x)$ is uniform as shown in Fig. 2.7, assuming the uniform detector irradiation. From the normalization condition one has $P(x) = \frac{1}{p}$, where p is the pixel pitch size. Basing on Eq. 2.29, the standard deviation of x for uniform distribution is

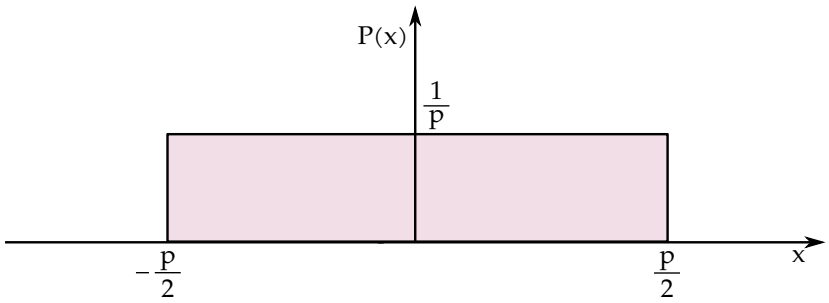

FIGURE 2.7: Uniform density of particle hit distribution $P(x)$ for pixel size p.

equal to:

$$\sigma_x = \sqrt{\int_{-\frac{p}{2}}^{\frac{p}{2}} (x-\mu_x)^2 P(x)\,\mathrm{dx}} = \sqrt{\frac{1}{p}\int_{-\frac{p}{2}}^{\frac{p}{2}} x^2 \mathrm{dx}} = \frac{p}{\sqrt{12}} \tag{2.31}$$

Thus, the spatial resolution for binary readout is determined by the pixel size p divided by the square root of twelve (approximately 3.5). For example for the CLIC vertex detector, the pixel size has to be around 10.5 µm to fulfill the 3 µm of single-point spatial resolution when using binary readout.

The phenomenon which may improve the spatial resolution is charge sharing. When the collected charge spreads between several pixels and the energy information is available one can calculate the hit position weighting signal coming from those pixels. The spreading effect comes from charge diffusion. However, one cannot assume a linear charge division between pixels and the so-called η-correction is necessary to be applied, what is widely described further in Sec. 4.5.

In order to calculate the resolution of the device under test (DUT), the proper reference has to be defined. The common measurement uses other detector with known spatial resolution, forming so-called telescope detector with several planes allowing for whole track reconstruction. The telescope resolution σ_t affects on the DUT true resolution σ_{res}, therefore it has to be finally subtracted:

$$\sigma_{\mathrm{res}} = \sqrt{\sigma_{\mathrm{DUT}}^2 - \sigma_t^2} \tag{2.32}$$

where σ_{DUT} is measured DUT resolution. In order to estimate σ_{DUT} the residuum distribution is studied. The difference between the measured hit position and the reference position (track position) is the residuum value. When charge sharing occurs, the residuum distribution may be modeled by Gaussian distribution. Thus, the standard deviation of residuum distribution acts as a measured DUT resolution. Nevertheless, the delta electrons as well as the clusterization constrains may often distort the shape of the residuum distribution [44]. In such a case the standard deviation of the distribution may give a misrepresenting results when the non-Gaussian tails contribute to the residua distributions. The common solution is reject from the whole sample around 5 % of extreme entries and then calculate a standard deviation. Other solution is to fit a Gaussian and take its standard deviation as the measured spatial resolution σ_{DUT}. Rejecting extreme entries while fitting a Gaussian fit is also a known approach.

Chapter 3

Detector design and measurement setup

The Cracow group is developing the silicon pixel detectors focused on requirements of the CLIC vertex detector. The used technology is provided by the Japanese Lapis Semiconductor Corporation and it is the Fully-Depleted Low-Leakage 200 nm SOI CMOS process, introduced already in Sec. 1.3.3. The significant benefit of the Lapis SOI is a possibility to fabricate monolithic structures. Since the monolithic pixel detectors show many advantages over popular nowadays hybrid solutions, the R&D on these detectors is ongoing for the demanding CLIC vertex system. Although the Lapis SOI CMOS electronics has been used for commercial purposes for a long time, the studies of its use for particle physics experiments are relatively new. Thus, the technology parametrization and understanding its specific physical phenomenons are still ongoing.

The Lapis process offers one single polysilicon layer and five metal layers. The supply voltage is 1.8 V for core transistors and 3.3 V for I/O transistors. There are also several kinds of buried n/p-well formations (different doping concentrations and depths) available for user to sensor design. The thickness of BOX is around 200 nm. The Top-Si layer dedicated for electronics implementation is 40 nm thick and it is fabricated using Czochralski type p process. The Lapis SOI CMOS pixel detectors may be fabricated on four different wafer types: the Floating Zone type n (FZ-n) and type p (FZ-p), the Czochralski type n (CZ-n) and the Double SOI type p (DSOI-p). The wafers differ with resistivity and thicknesses as it is presented in Tab. 3.1.

In the past few years five SOI detector prototypes have been developed in Cracow. I have been taking part in design and implementation of the last four ASICs (Application-Specific Integrated Circuit) and I was responsible mainly for design and simulations of matrices

Wafer name	Carrier type	Labeling	Thickness	Resistivity
Czochralski	n	CZ-n	300 µm	above 0.7 kΩcm
Floating Zone	n	FZ-n	500 µm	above 2.5 kΩcm
Floating Zone	p	FZ-p	500 µm	above 4 kΩcm
Double SOI	p	DSOI-p	300 µm	above 2 kΩcm

TABLE 3.1: Lapis SOI CMOS wafer types, their thickness and resistivities.

control logic blocks, pixel test structures and a Successive Approximation Resister (SAR) Analouge to Digital Converter (ADC) for future use in SOI detectors. The design and simulation procedures take usually about half an year. The SOI detector production is relatively long process, because the ASICs come from fabrication in the best case after six months. Except the design, I have been also involved in data collection during beam-tests and also for full data analysis process of this data, what is the core of this dissertation.

Two of the mentioned Cracow SOI prototypes were adapted to the tests with particle beam. They were fabricated and tested in 2016 and 2017 year respectively. Both of these prototypes are focusing mainly on fulfilling the CLIC vertex spatial resolution demand (3 µm) but also on technology possibilities testing. It is worth to mention, that the last fifth designed prototype, called CLIPS (CLIc Pixel Soi), is targeting strictly to the CLIC vertex detector requirements, including spatial resolution and time-stamping demands and also taking into account material budget constrain. I have been also fully involved in the CLIPS development, which was sent to production in December 2017. It came from Lapis in the middle of 2018, but is not yet measured.

3.1 Detector design

Basically, the designs from 2016 and 2017 year are very similar. In Fig. 3.1 graphical schemes of both prototypes are shown. For each case the detector is built of two matrices of 8×36 pixels with pixel size (pitch) equal 30 µm $\times$ 30 µm. One of the matrix is incorporating source followers (SF) and the second one charge-sensitive preamplifiers (CPA) pixels readouts. There is a physical gap between the SF and CPA matrices of about 114 µm, where some part of the readout electronics is placed. Unfortunately, there are no dummy pixels around the matrix.

As it was mentioned before, the main aim of the SOI detectors development is not only the R&D for CLIC, but also gaining professional knowledge about Lapis technology. Thus, the 2016 SOI prototype was treated as a test structure. It was also the first time for Cracow SOI detectors to be used on the test-beam, so the group was getting familiar with the setup infrastructure and test-beam measurements specifications. Because of these two facts, the 2016 prototype comprised several features making it not perfectly tuned to regular, fully conclusive measurements. First of all, a mistake in design of biasing circuits for the CPA matrix was done and finally it has been not working. On the other hand, the SF matrix is built of smaller submatrices as shown in Fig. 3.1A, each of slightly different layout and design. Since the technology is not fully parameterized, the purpose of incorporating various modifications in pixel designs was to find the best working configuration and also to compare the simulation results with the real performance. These modifications regarded mainly input transistor type since there are four transistors types provided by the Lapis SOI. Also two different BP(N)W layer sizes were used, what results in different detector capacitance. In Fig. 3.1A dark violet marks a large sensing diodes and lighter violet are smaller sensing elements. Unfortunately, the sumbatrices are too small to provide enough statistics

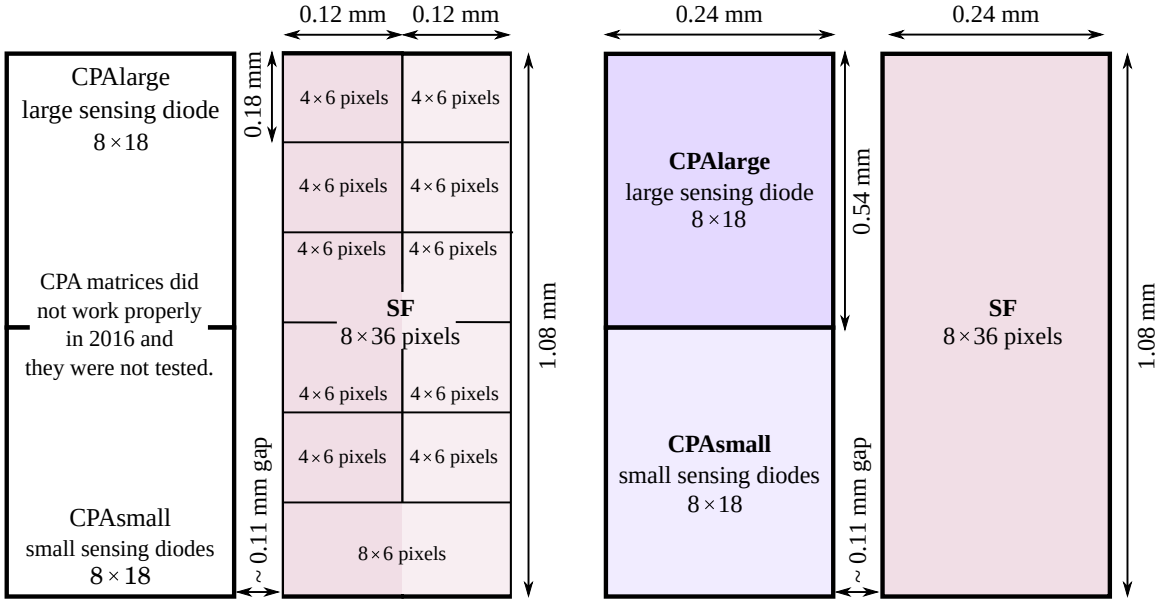

(A) 2016 prototype (B) 2017 prototype

FIGURE 3.1: Schemes of detector matrices from 2016 and 2017 year. The darker shade of the same color means respectively larger sensing diode size.

from beam-test data and to perform a separate analyses of test-beam data because of limited statistics. Moreover, the different gains and different noise levels of each submatrix distort the overall matrix performance. In this dissertation, the detailed differences between submatrices are not discussed, since the analysis are finally made for entire matrix.

In 2016 the prototypes were fabricated on two types of wafers: the CZ-n and the FZ-n. The working performance of the CZ-n detector wafer was verified during laboratory measurements and also during test-beam. The correctness of operation is confirmed, but the noise of the CZ-n was much higher than in the FZ-n, thus the regular tests were done for the FZ-n detectors.

Although the 2017 prototype is very similar in design to that from 2016, the improvements that were done significantly changed the performance of the detector. The matrix scheme is presented in Fig. 3.1B. For this matrix, both SF and CPA pixels are working properly. The pixel size is also 30 µm × 30 µm and there are two matrices of 8×36 pixels with gap in-between them as shown in Fig. 3.1B. The SF matrix is this time homogeneous built of identical pixels. The CPA matrix is divided into two parts again with small and large sensing diode sizes. Hence, the CPA matrix consists of two submatrices of 8 × 18 pixels each. Different BP(N)W sizes are dedicated to different detector wafer types. This two submatrices are further denoted as CPAsmall and CPAlarge respectively.

3.1.1 Pixel readout electronics architecture

The description of signal integration ideas comprised by both the SF and CPA readout architectures have been already introduced in Sec. 2.3. The CPA is designed as an universal pixel readout, meant for each wafer type since its signal is independent on a detector capacitance.

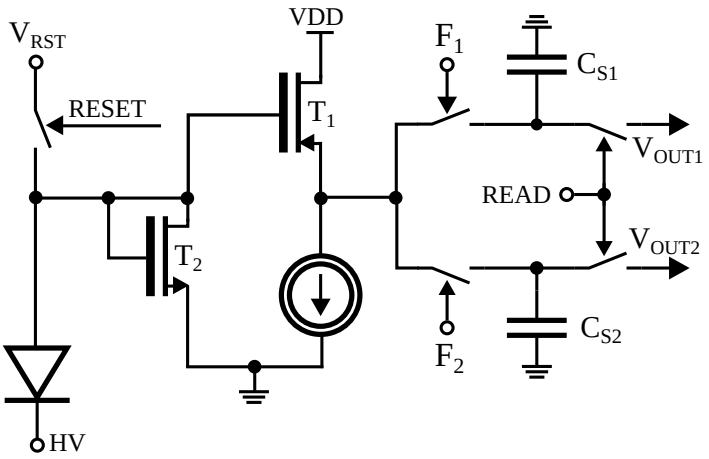

FIGURE 3.2: Scheme of the source follower pixel readout electronics.

It is especially the case for the DSOI, characterized by significantly larger detector capacitance than single SOI. As discussed in Sec. 1.3.3 on page 15, for the DSOI wafer there is no need to implement the BP(N)W, since the Mid-Si shields the electronics from high voltage coming from sensor polarization. Theoretically, the BP(N)W layer could be fully discarded, but the process developers advice to implement any BP(N)W layer at least of very small size. Thus, the CPAsmall, dedicated for the DSOI-p, has the BP(N)W size of $5 \times 5\,\mu m^2$. In order to keep the full functionality of the CPA also on the single SOI, a half of the matrix has implemented a large BP(N)W. It is covering nearly the whole pixel area of around $29 \times 29\,\mu m^2$ but it is non-regular shape. The non-square shape is a compromise between as small BP(N)W size as possible but still shielding all active electronics elements. As it has been found out later, this submatrix shows incomprehensible effects and one can suspect that the BP(N)W shape may be the reason for that.

For the SF architecture the signal is inversely proportional to the detector capacitance, thus this design was originally dedicated only for single SOI structures. The BP(N)W size is about $13 \times 13\,\mu m^2$. The expected benefit from SF matrix would come from its simple architecture and thus predicted low noise. The pixel readout electronics have not been designed by the author of this thesis, but theirs short introduction is made further in this section for better understanding the results presented in the last chapter.

Source follower

The source follower readout architecture is presented in Fig. 3.2. The design comprises a source follower, so common-drain amplifier, which is formed by input capacitor T_1 and current source. The T_2 transistor acts as protecting diode. The control $RESET$ signal resets the input node to V_{RST} voltage. There are two phases of working of the presented architecture, controlled by signals F_1 and F_2. The first phase is sampling the baseline value on C_{S1} capacitance. In the second phase the sum of signal and baseline is sampled on C_{S2}. This technique is known as Correlated Double Sampling (CDS) which allows for low frequency noise reduction and provides differential output signal. The readout of the outputs signals V_{OUT1} and V_{OUT2} is controlled by $READ$ signal. The detailed description of this design and

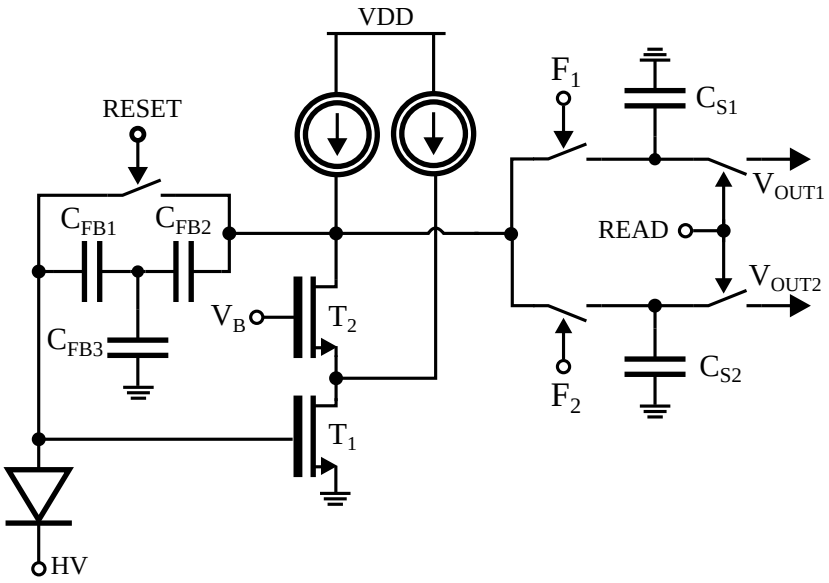

FIGURE 3.3: Scheme of the charge preamplifier pixel readout electronics.

its laboratory measurements can be found in [45]. The layout of the pixel readout is shown in Fig. 3.4.

Charge-sensitive preamplifier

The scheme of the second implemented pixel readout electronics is shown in Fig. 3.3. The charge preamplifier utilizes a telescopic cascode in the input stage, realized by T_1 and T_2 transistors. Since the signal amplification depends inversely proportional on feedback capacitance (see Sec. 2.3), the T-shaped capacitor structure ($C_{FB1,FB2,FB3}$) was implemented to minimise its effective value. The CDS technique was also used as in case of the source follower. The detailed simulations and design description can be found in [46].

3.2 Matrix readout

There are two popular modes of reading pixel matrix: the global shutter and rolling-shutter. In general for both of them two phases may be distinguished: integration time, when pixels are collecting charge generated by particles and readout phase, insensitive for projectiles. In the global shutter mode the integration phase is common for the whole matrix and followed by the readout phase. Since in the readout phase information from each single pixel in the matrix has to be processed it usually takes relatively long time. This leads to long dead time. Whereas in the rolling-shutter mode the matrix is read out partially. It means that only the part of the matrix is disabled in particular time period and the rest is active.

The rolling-shutter was chosen for readout mode of Cracow SOI prototypes, both from 2016 and 2017 year. In our case, where readout takes place row by row, only a certain row is during the readout phase, but the rest of the matrix is still in the integration phase. Thus, each row is active for equal time period, but different rows are active in different time. This mode reduces the dead time since major part of the matrix is always sensitive to incoming

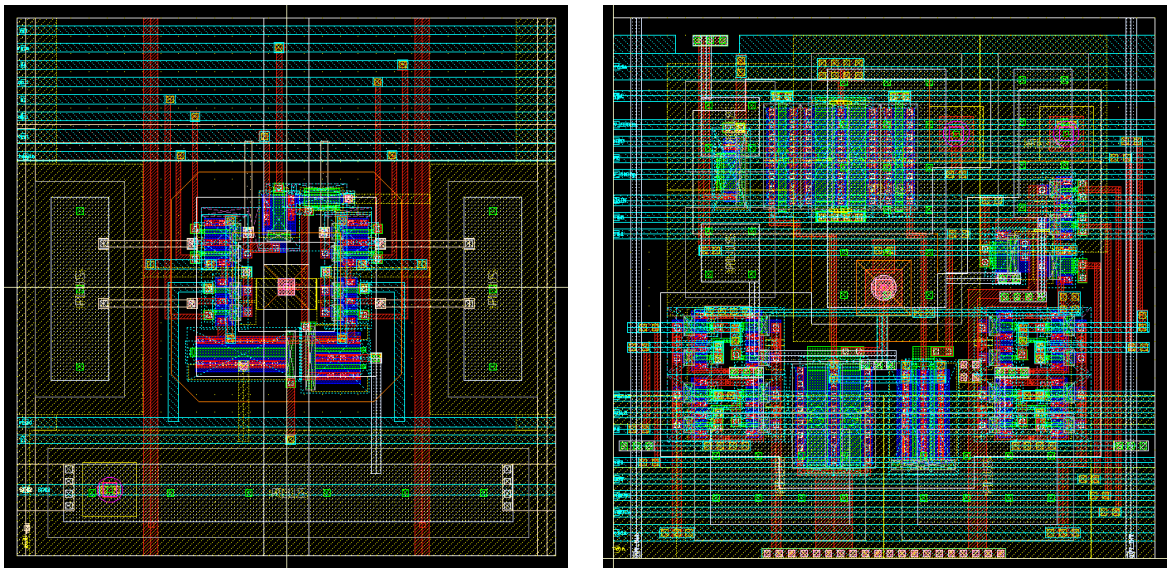

(A) Source follower (B) Charge-sensitive preamplifier

FIGURE 3.4: Pixel layout pictures.

particles. The disadvantage of the rolling-shutter is that a signal may be spread into two consecutive frames or may be partially lost. This issue is studied further in Sec. 4.7, since it has a significant influence on the data quality.

Only two external signals were needed for matrix reading control. This was a reset signal and readout clock. The readout clock period determined the length of frame integration time and also reset phase duration. In 2016 the frequency of readout clock was set to a constant value and it was around 5.91 MHz. In 2017 approach the frequency could be changed by an user and data were thus collected with the same clock as in 2016 and two times faster also.

An analogue signal is sent out from the pixels row by row. When a certain row is being read out, output signal of each pixel in that row is connected to the fully differential column amplifier, which buffers the signal. Later on the buffered signals are serialized and send out of the chip through the output amplifier. Then the signal is digitalized using an external 12-bit ADC.

3.3 Measurement setup

The custom Printed Circuit Board (PCB) containing an external ADC, biasing circuitry and decoupling capacitances was integrated with on mezzanine board, where the detector was bonded. The photography of the PCB from 2017 year is shown in Fig. 3.5A and 3.5B. The PCB board from 2016 and 2017 measurements setups were almost identical regarding the functionality, but differed in geometrical shape. The 2017 version was smaller in order to use it on rotating stage in CLICdp telescope box. The mezzanine board is presented in Fig. 3.5C. Bonding the detectors to the separate mezzanine boards simplify the system assembly, since

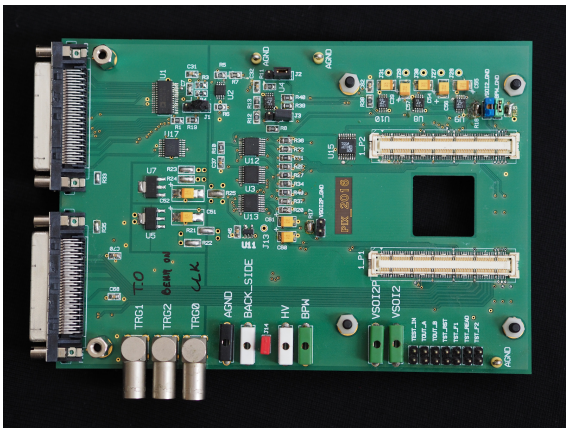

(A) Front side of readout board. On the right side there is hole for detector and connectors for mezzanine board.

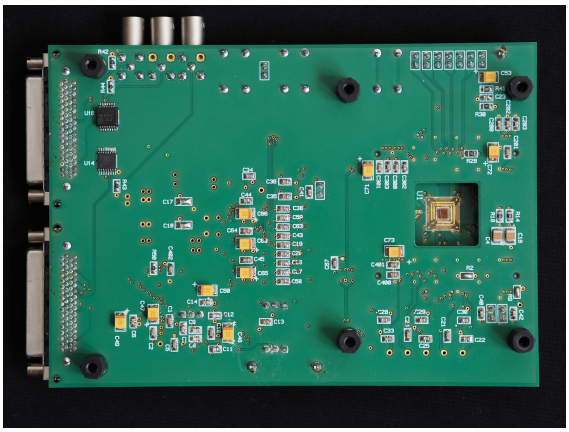

(B) Back side of the readout board with mezzanine board assembled. Detector unit is visible through the hole in the PCB.

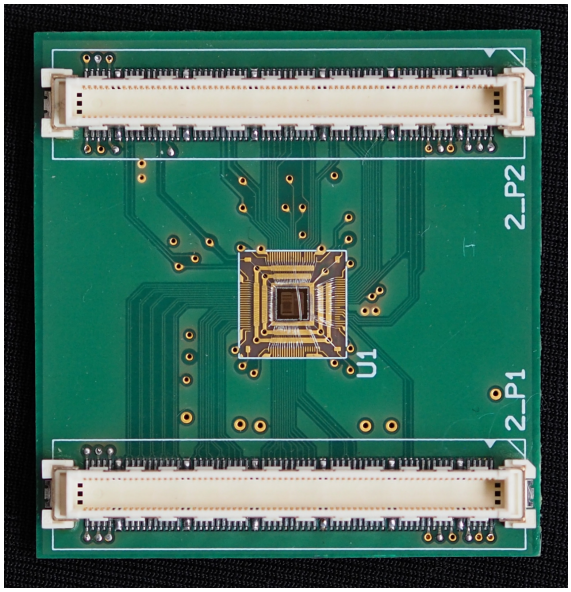

(C) Enlarged photo of a mezzanine board with detector bonded.

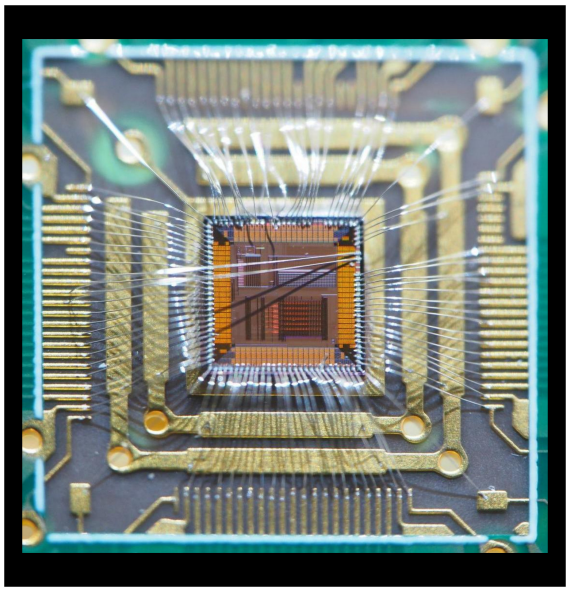

(D) SOI detector prototype photography. One can see matrices structure on the chip.

FIGURE 3.5: SOI detector from 2017 and its readout board.

only a small part has to be changed in the telescope box in order to change detector prototype. The photography of exemplary SOI detector is shown in Fig. 3.5D. The matrices structures, bonds and output pads are clear to see. The size of ASIC was 2.9 mm $\times$ 2.9 mm.

The data acquisition (DAQ) system was based on Diligent Genesys Virtex-5 FPGA Development Board. After digitalization the data were buffered, merged into frames and sent out from the FPGA via 1 GB Ethernet to an external computer. The framework controlling data acquisition was implemented using the ROOT6 [47] for Graphical User Interface (GUI) and C++ boost classes for the Transmission Control Protocol/User Datagram Protocol (TCP/UDP) and multi-threading. The output raw data were stored as a ROOT tree.

The only signals that had to be provided from the telescope to the DUT during the beam-test data collection were the reset signal and the beam-on control signal, corresponding to the presence of the particle beam. The data were collected only when the beam was

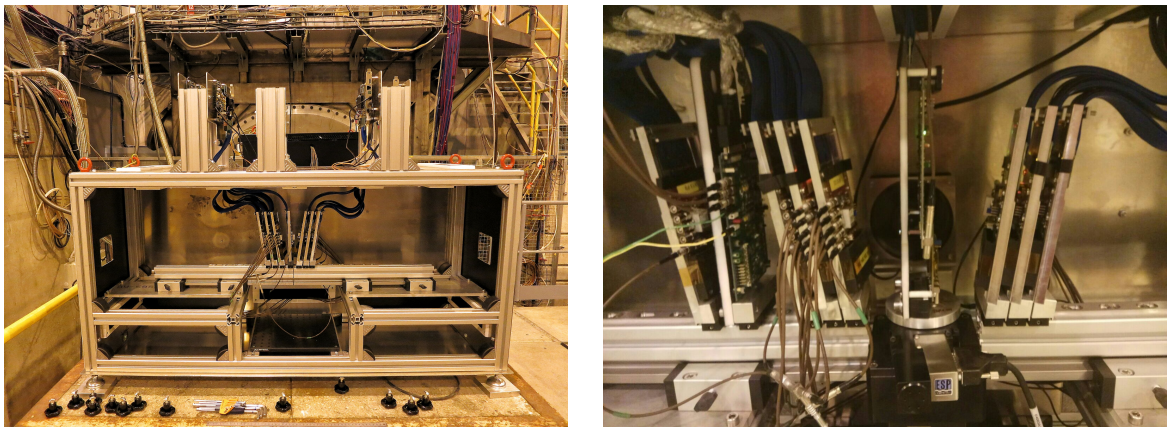

(A) Open telescope box with seven Timepix3 planes inside

(B) SOI detector assembled in telescope box (second last on the left side)

FIGURE 3.6: Test-beam infrastructure.

present. At reset signal, the time counter of any device in the whole detection system was reset what allows for the synchronization of the detectors. Due to an error in the 2016 readout version, the time counter was reset twice, once together with the other devices at the very beginning of the readout and second time after sending a command to begin a new measurement. The time between this two actions was arbitrary and thus each DUT dataset had a variable time-offset in relation to telescope time-stamping. Because of this issue the DUT hit and telescope track correlation were not straightforward and the time-offset had to be found in off-line analysis for each dataset separately. This problem was solved in the next readout version.

3.3.1 Testbeam infrastructure

The beam-test were performed in CERN SPS North Area at H6 beam line in collaboration with CLICdp group. A pion beam with an energy of 120 GeV was used. The CLICdp telescope provides seven detector planes, rotating centre-placed stage and since 2017 year the movable telescope box remotely controlled. The telescope box is shown in Fig. 3.6A with one of the telescope planes mounted at the DUT position. The 2017 SOI detector prototype assembled in the telescope box is shown in Fig. 3.6B.

The telescope is built of Timepix3 pixel detectors [48]. The pixel size is $55 \times 55\,\mu m^2$ and the detector was implemented on 300 µm thick wafer for the sensor matrix. The detectors are providing the information about deposited charge, basing on time-over-threshold (ToT) and also about the particle time of arrival (ToA). The telescope planes were tilted by 9° both in x and y direction (perpendicular to the beam), allowing to reconstruct usually three-pixel clusters and improve the spatial resolution thanks to charge sharing [49]. The tracking resolution at the DUT point was about 2 µm. The SPIDR (Speedy PIxel Detector Readout) readout system was used for DAQ of the telescope data [50].

Chapter 4

Analysis methods

There are several softwares available for particle detector data analysis, such as Modular Analysis and Reconstruction for the LINear collider (Marlin) [8]. These tools are usually very complex and often they are relatively complicated and time-consuming to modify and adapt for non-standard detectors. This might make the analysis non-efficient and also impede the DUT debugging if so is needed. As it was mentioned before, the used Lapis SOI technology is not well parametrized yet, so there were a lot of custom checks during data analysis, dedicated for these particular detector. Therefore, for the purpose of this work, the compound software for the SOI detector studies has been developed, incorporating several useful and novel analysis methods. Part of these methods is well-known and used in other similar projects. Nevertheless, also a new algorithms are proposed such as multi-pixel η-correction. A knowledge about how the proposed algorithms work is a crucial step for understanding the final results presented in the last part of this dissertation.

Two SOI detector prototypes, which designs were described in the chapter 3, were tested on beam at SPS H6 at CERN in summer 2016 and 2017. Since the 2016 test-beam was the first one of the Cracow SOI detectors, both design and analysis were less advanced and also less adapted to test-beam infrastructure than those from the 2017 year. For this reason, the following chapter includes detailed description of data analysis methods and partially results for the newer design. In case of important differences between used analysis algorithms for the 2016 prototype it is indicated in the text.

In order to keep clarity of the often used terms several definitions are presented in Tab. 4.1 .

4.1 Analysis flow

The analysis of test-beam data is performed using three separate tools: track reconstruction software, DUT cluster reconstruction software and post-clustering analysis tool merging the outputs of previous two. The first one incorporates telescope data to reconstruct full track and its position at the DUT plane. The two other frameworks are dedicated for the Cracow SOI silicon detectors analyses. Nevertheless, the implemented algorithms are universal for pixel detectors in overall and may be easily adapted to other devices.

Name	Definition
dataset	Single data collection. Each dataset is characterized by particular settings (such as back bias voltage, pixel amplification, readout clock frequency). The dataset is mainly built of structures containing frames and theirs time-stamps.
spil	Batch of particles of desired energy; usually over a dozen spils were collected among single dataset (the limitation came from the telescope dataset size). Typically, spil time was about 5 s with time gap between spils of about 15 s to 40 s.
frame	DUT data package containing each pixel signal.
frame time-stamp	Time-stamp from external counter attached to the particular frame.
frame time	Time interval between two consecutive resets of a certain row. Denoted further in this work by W. The frame time dependents on readout clock frequency.
readout clock	Clock controlling readout of the matrix. Two different readout clock frequencies were used: around 6 MHz and around 12.5 MHz.
row time-stamp	Time-stamp attached to particular row of the matrix, reconstructed in software (it is not the direct information from data acquisition system).
cluster	Group of pixels containing reconstructed particle signal.
DUT hit	Particle recorded by the DUT. Its position is extracted from related cluster and ToA is taken as a corresponding frame (or row) time-stamp.
track position	Telescope track position at the DUT plane.
track ToA	Telescope track time-stamp used as reference particle time of arrival (ToA).
residuum	Difference between DUT hit and track positions calculated separately for x and y direction.

TABLE 4.1: Definitions of frequently used terms in this chapter.

4.1.1 Track reconstruction framework

The track reconstruction is performed using EUTelescope software. It is based on a group of Marlin processors that are used for the telescope data analysis [8]. The components elements of EUTelescope are the event-based data format called LCIO, the geometry description tool-kit GEAR and the set of Marlin event processors. The processors take parameters via so-called steering files in XML format. The EUTelescope strategy is graphically shown in Fig. 4.1.

For each dataset following steps are done using particular Marlin processors [49]:

1. *Format converter* — optional step, required when a detector output is saved in other format than the LCIO and data format conversion is needed.
2. *Cluster search* — cluster reconstruction for each telescope plane.
3. *Cluster selection* — rejection of clusters suspected of low quality.
4. *Hit maker* — hit position calculation and performing the η-correction.
5. *Alignment* — telescope planes alignment using Millepede II algorithm [51].
6. *Track fitter* — track reconstruction from hits recorded on telescope planes. The track fitting method is based on χ^2 minimization.

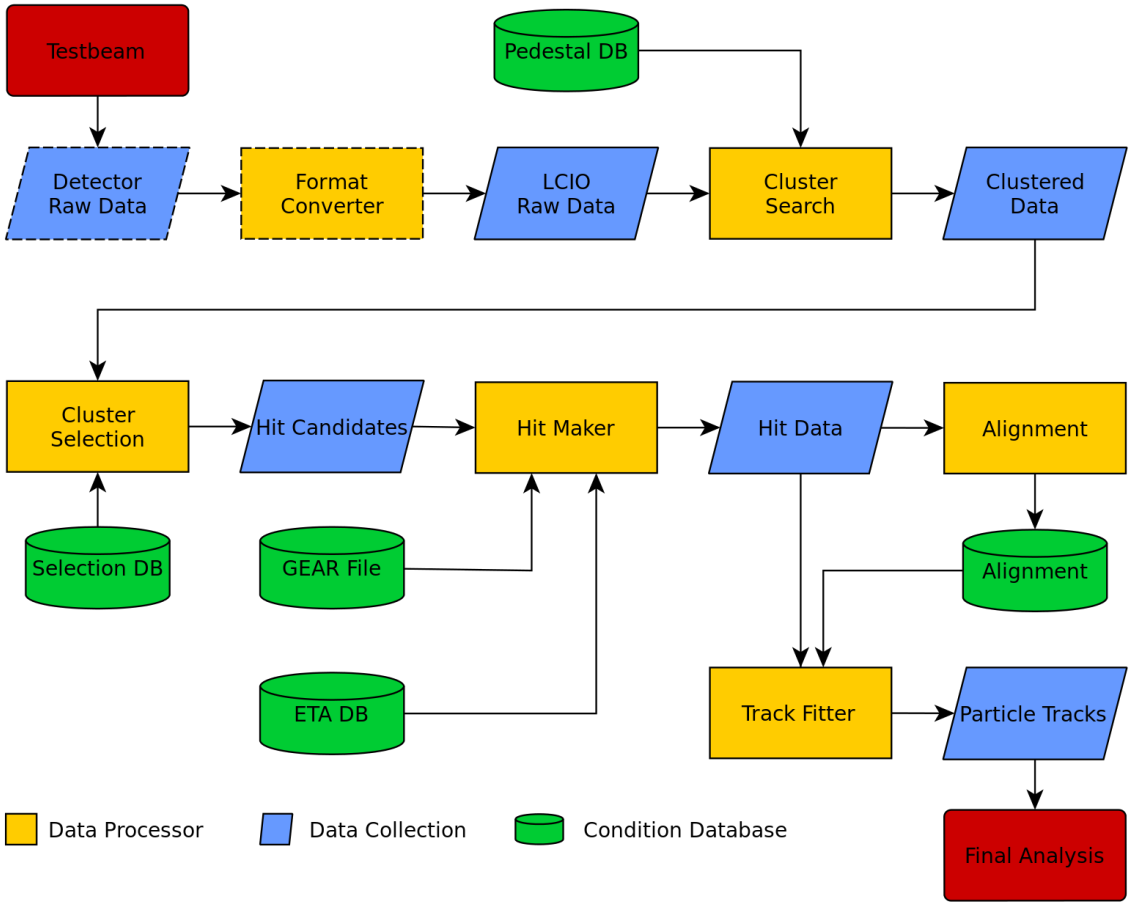

FIGURE 4.1: EUTelescope framework block diagram of working flow [8]. The dashed blocks presents optional steps of the analysis.

After tracks reconstruction, the output data collection is saved as the ROOT tree. It contains the tracks x and y positions at the point of the DUT plane together with other parameters regarding tracks quality.

4.1.2 DUT clusters reconstruction framework

The first major step in the DUT data processing is a clusterization procedure. The dedicated analysis software is a standalone tool which saves an output as the ROOT tree. This outcome might be used for test-beam analysis as well as for laboratory measurements with radioactive sources and lasers. There are several steps performed for each dataset:

1. *Preliminary hit rejection* — preparing the calibration file. It is optional step needed when there is no dataset with raw baseline. During test-beam data have been acquired only when beam was on. Thus, some part of the dataset has to be cleaned out from events with hits in order to calculate the baseline and noise of each pixel.
2. *Baseline and noise calculation* — baseline and noise calculation for each pixel separately.
3. *Area selection* — bad and hot pixels rejection if there are any. As a bad or hot pixels one can understand any pixel showing deviations from standard behaviour, such as

higher or lower baseline or noise than the average value. Also edge rows and columns are excluded from analysis.

4. *Cluster finding* — cluster reconstruction. For each dataset different clusterization methods are used and different criteria for signals extraction, as well.

4.1.3 Post-clusterization analysis framework

After the DUT hits and telescope tracks reconstruction, both data collections are being post-processed to match track-hit pairs coming from one particle. This allows for the spatial resolution and efficiency calculation. The post-processing is done using standalone framework. In this stage there are major differences between 2016 and 2017 analysis. The analysis flow is following:

1. *Time-offset finding* — time-stamping alignment of DUT hits and telescope tracks. In the 2016 prototype, because of hardware connected issues discussed already in Sec. 3.3, the DUT time-stamps were attached with variable time-offset in relation to the telescope time-stamping. In consequence, time correlation between the DUT hits and tracks was not direct and for each dataset there was a need to find a time shift. In 2017 this issue was fixed.
2. *Preliminary track-hit correlation* — preliminary matching of the DUT hits and telescope tracks which is done to find the translation vector from local coordinate system of the DUT to global coordinate system, defined by the telescope. During this preliminary correlation also reset-affected DUT hits are eliminated, but this upgrade is done only in 2017 analyses. The correlation is threated as preliminary, because since the telescope and the DUT coordinates systems are not aligned, a small sample of track-hit pairs may be randomly (wrongly) correlated. The correlation algorithm is the same as in case of proper track-hit matching.
3. *Coordinate system translation* — translation of the DUT hit positions from local coordinate system to the telescope global coordinate system.
4. *Track-hit correlation* - pairing tracks and DUT hits in time and in space. The correlation conditions are different for the efficiency analysis and for the spatial resolution analysis. There are modifications of this algorithm for 2016 and 2017 analysis, that are described in the following paragraphs.
5. *Multi-pixel η-correction* — correction of centre-of-gravity (COG) positions using modified algorithm of the standard η-correction. In overall, it could be also performed just after clusterization of the DUT hits because the procedure is track-independent, but after correlation with tracks the data sample is cleaner (no noisy entries, no strongly distorted delta electrons events, no reset-affected clusters). This increases the quality of proposed η-correction procedure.
6. *Alignment* — finding rotation angles if there are any and optionally rotating the DUT matrix. The rotation of the matrix is performed by minimising spatial resolution in function of rotation angles. If the rotation is needed, the translation vector is updated

Name	Definition
	TRACK COLLECTION
event number	event ordinary number
x and y position	positions of the track (x^T, y^T) given at DUT point
time-stamp	track ToA (t^T) given in counter units. Single counter unit corresponds to one period of telescope clock – 25 ns
χ^2	measure of goodness of track reconstruction obtained using χ^2 test
ndof	number of planes that were taken to track reconstruction
	DUT COLLECTION
event number	frame ordinary number
x and y position	position of the DUT hit (x^D, y^D) calculated using COG method in local coordinates system
time-stamp	time of the DUT hit (t^D), equal to the particular frame time-stamp, given in counter units. Single counter unit corresponds to one period of readout clock (in practice it was around 60 µs or around 130 µs)
cluster size	number of pixels in the cluster, given in total and also separately for x and y direction
cluster energy	sum of signals from all pixels in the cluster given in ADU
SNR	cluster signal to noise ratio
matrix seed	flag indicating if seed pixel is reconstructed on CPAsmall, CPAlarge or SF
matrix cross	flag pointing if the cluster is reconstructed on more than one submatrix
matrix border	flag pointing if the cluster is touching border of the matrix
seed x and y position	position of the pixel with the highest energy in the cluster in local coordinates system
seed energy	energy of the seed pixel given in ADU

TABLE 4.2: List of variables building the track data collection and DUT data collection.

and the track-hit correlation is performed once more since the correct alignment is a condition for precise hit-track correlation.

7. *Final analysis* — cluster size, spatial resolution, efficiency and other detector final performance studies.

As it was mentioned above, there are two independent data outputs available after tracks and DUT hits reconstruction called further tracks data collection and DUT data collection. The tracks data collection contains information about tracks, coming from Marlin environment [8]. In principle, a single entry to the track data collection is built of variables shown in Tab. 4.2. Marlin software provides more information but for this particular analysis only the set presented in the table is used. The DUT data collection entry is more complex and a single one keeps information useful also for debugging. The DUT event variables are also presented in Tab. 4.2.

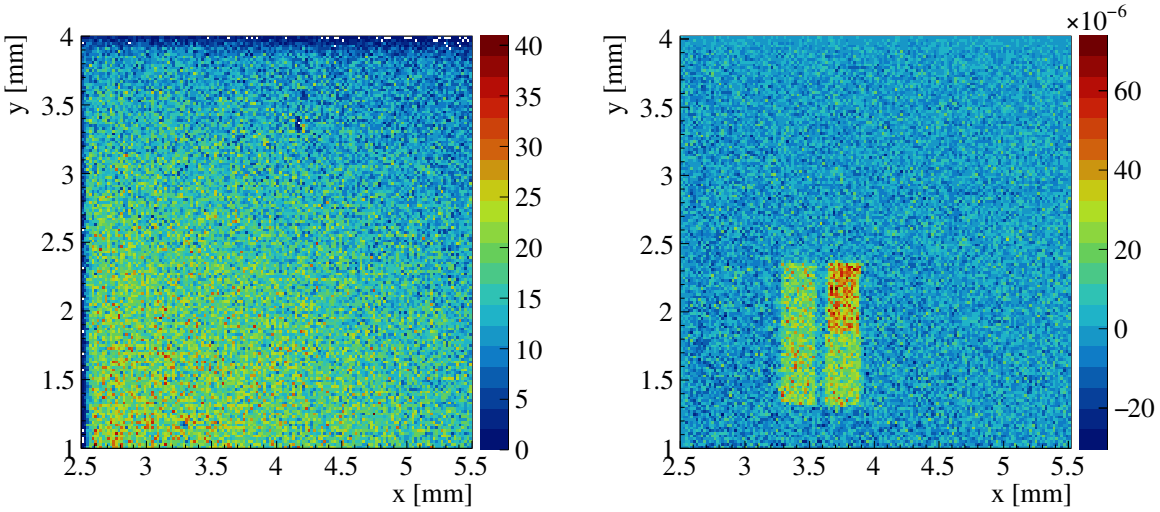

(A) Fragment of beam profile

(B) DUT location over telescope planes

FIGURE 4.2: Finding the DUT position during the test-beam data acquisition. The maps are created from tracks positions.

4.2 Online monitoring for DUT location

During the test-beam different DUTs assemblies were mounted several times in the telescope box. The beam position was changing and the telescope planes might have been rearranged, as well. Because of that there was a constant need of fast monitoring whether the DUT was placed in the beam's light. The proposed method is relatively fast, since it is using a small sample of data collections (about 100k events) and thus it may be used during test-beam data acquisition.

To find the position of the DUT over a telescope planes, the algorithm selects telescope tracks with ToA in the range of several frame times from any DUT hit time-stamp. It means, that track collection is limited to these entries, which occurred only when the DUT also had a hit recorded. Remembering, that part of these tracks have to come from the same particle that left a hit in the DUT, this procedure prefers tracks occurring in the area of the DUT detector. Using such a limited data sample the track position map is created. The beam profile is always subtracted, because it is dominating any other effect. The example of normalized beam profile generated from telescope tracks is presented in Fig. 4.2A. The map showing the DUT location over telescope plane obtained using described procedure is presented in Fig. 4.2B. Finding the DUT position allows also to reduce the area of track reconstruction that significantly reduces computing time.

4.3 Cluster formation methods

The compulsory step in the whole analysis is to find well working algorithm for cluster reconstruction, suitable for particular detector. The charge sharing effect, spreading a charge generated by an ionizing particle between several electrodes, depends on several parameters such as detector thickness, silicon resistivity, collecting electrodes pitch and applied

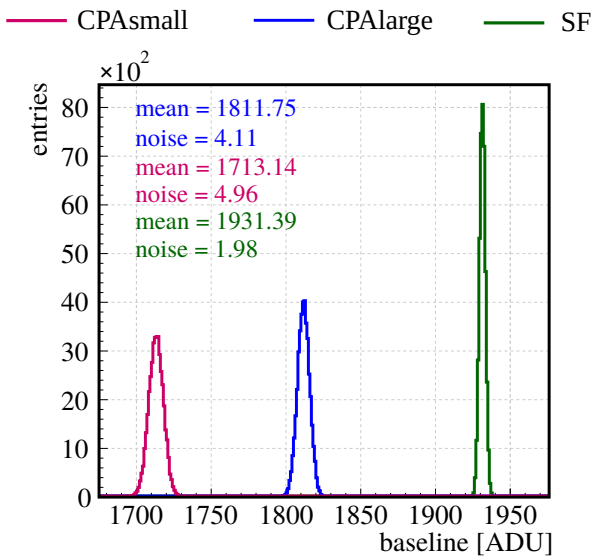

FIGURE 4.3: Single pixels baseline spectra for different matrices. The mean value of a spectrum is taken as a pixel baseline and its standard deviation as noise.

back bias voltage. Therefore, the charge distribution over detector volume may behave significantly different for various conditions. The clusterization procedure has to select pixels in the way that contribution of signal and noise among the cluster will be optimal in terms of assessing particular physical quantity resolution. This means that to obtain the best energy resolution and spatial resolution one may have to use different clusterization method. In this work mainly the spatial resolution is being considered and since the charge sharing effect is significant giving relatively large signal spread (on average three pixels in each direction) it is worth to study different clusterization methods.

First step of the analysis is to extract pixels baseline and noise. Using the calibration data sample, the baseline spectrum is generated for each pixel. The example of such spectra from the experimental data are presented in Fig. 4.3. The mean value of the spectrum is the baseline value B and its standard deviation corresponds to noise σ. The extracted signal S_i of the i'th pixel is defined as a difference between pixel's raw signal R_i coming directly from a detector output and its baseline value:

$$S_i = R_i - B_i \tag{4.1}$$

The default method for clusterization is a well-known algorithm using two thresholds, one for determining the cluster seed (pixel with the highest signal) and the second for its neighbours. Further in this work this method is called Two Threshold Method (2TM). When two threshold values are defined, the 2TM method is denoted as 2TM-th_{seed}-th_{neigh} for simplicity. The threshold values are expressed basing on signal to noise ratio. Thus, the first th_{seed} defines a signal to noise ratio that has to be exceeded to select pixel as a seed. The analogues condition is imposed on the second threshold th_{neigh} for selecting neighbouring pixels. The th_{seed} is always greater or equal to th_{neigh}.

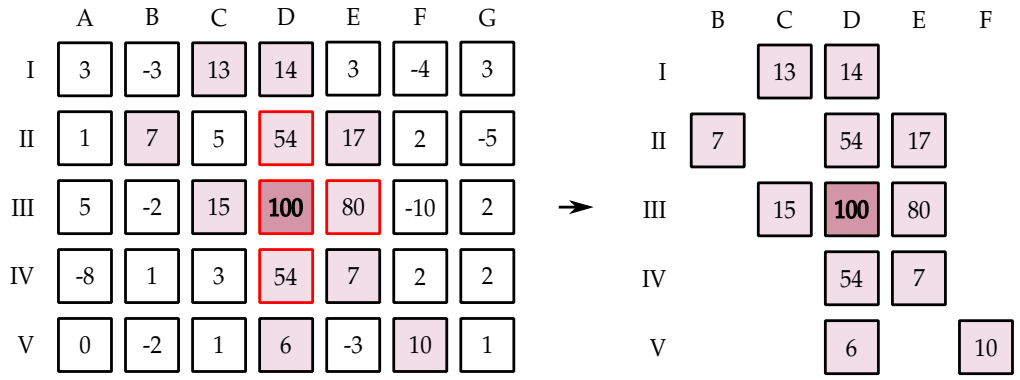

FIGURE 4.4: 2TM clusterization. The numbers in squares correspond to signal to noise ratio for particular pixel. Example is shown as for $th_{\text{seed}} = 20$ and $th_{\text{neigh}} = 6$. The seed is marked as dark violet and neighbours pixels on light colour. In red frame there are a pixels exceeding $th_{\text{seed}} = 20$.

In Fig. 4.4 an exemplary scheme of cluster reconstruction using 2TM method is shown. The seed-search is an universal algorithm for all clusterization methods. The search starts from finding any pixel with SNR greater than or equal to th_{seed}. If any is found, algorithm verifies if there are more pixels adjacent to it, that also fulfill th_{seed} condition. This step is repeated every time when any new pixel matching imposed condition is found. From all pixels selected (marked with red frame in Fig. 4.4), the one with the highest signal is chosen and this pixel is called the seed pixel. Its energy and position is always saved to the DUT data collection as a additional information about the cluster.

For 2TM method, after determining a group of pixels with SNR greater than or equal to th_{seed}, the algorithm searches for neighbouring pixels with SNR greater than or equal to th_{neigh}. For example in Fig. 4.4 the search is done around red-bordered pixels. It also could be done from scratch, starting the search from the seed pixel, but since the $th_{\text{seed}} \geq th_{\text{neigh}}$ the result would be the same, but the computing time would be longer. As in case of the seed search, if any new neighbouring pixel satisfying given condition is found, the algorithm repeats the search around it (also via diagonal). The procedure is completed, when no more pixels can be added. All found pixels build a cluster. It may happen that this method leads to non-physical cluster shape as in the example shown in Fig. 4.4 where separate pixel merging only via diagonal is also attached to the cluster. Such clusters appear very rare (individual cases) but they may occur. The position is finally calculated from such a cluster using COG method.

There are two modifications of 2TM clusterization method presented in Fig. 4.5 called Two Highest Lines Method (2HLM) and Three Pixel Method (3PM). The feature of these methods is that different pixels sets are taken for position calculations in x and y direction. The premise for developing both methods is choosing only two lines (or pixels) in the selected direction and thus keeping the charge sharing effect, but limiting the number of pixels with lower SNR.

The 2HLM takes the 2TM cluster and chooses two columns for x and two rows for y with the highest total signal. It means, that algorithm calculates sum of each pair of adjacent rows or columns and for position calculation choses the pair that gave the highest total signal.

The 3PM limits the number of pixels in cluster even further, taking only two pixels carrying summary the highest signal in particular direction. Therefore, cluster has 3-pixels, but the position is calculated only from two pixels.

The next cluster formation methods are characterized by the fixed shape of the cluster and also fixed number of pixels contributing to it. These are Nine Pixel Method (9PM), Cross Method (CROS) and Four Pixel Method (4PM). All these clusterization algorithms need only single threshold condition th_{seed}. In the first step the seed pixel is determined in the same way as described above for 2TM. The 9PM is adding to the cluster all eight surrounding pixels, as shown in Fig. 4.6 and therefore a square-shape cluster with edge of 3 pixels if formed. The CROS method is very similar to previous one, but it does not include pixels on diagonal in relation to the seed pixel. Thus, here the cross-shape cluster comprising in overall 5 pixels is formed. The 4PM adds to the seed pixel three adjacent pixels and finally reconstructs a two-by-two pixels square cluster. There are four options of creating such a square as marked with various colors in Fig. 4.6. The total signal is calculated for each option and the configuration with the highest value is taken as a final cluster.

Pixels once used for cluster reconstruction are never used to form other cluster. An additional problem may occur in 9PM, 4PM and CROS since the final cluster might not contain all pixels exceeding th_{seed} and theoretically the excluded pixels might become seed for another cluster. To avoid this problem, all pixels that passed th_{seed} in one seed-search procedure (marked in light violet in Fig. 4.6) cannot be a part of any other cluster.

4.4 Area selection

The clusters reconstructed on the edges of matrix may loose charge outside a detector. When detector is large enough several border columns and rows can be discarded from the analysis. In case of the tested DUT, detector size in x dimension is very small (8 pixels) per each matrix type. Rejecting any column reduces statistics significantly. Two different strategies were applied for area selection in 2016 and 2017 test-beam analyses, since the designs of the matrices differ. The sketches of both approaches are presented in Fig. 4.7.

Just to remind, in 2016 prototype the CPA matrix did not work, what is symbolically marked with the grey cross in Fig. 4.7A. In the prototype from 2016 the source follower matrix was further divided into smaller submatrices as already described in Sec. 3.1 and shown in Fig. 3.1A on page 37. Rejecting completely one column from each side would limit submatrices to area of effectively about three pixel sizes. In addition this area would contain pixels with different gains and clusters reconstructed on the cross of various submatrices may suffer more on spatial resolution distortion. Also the statistics would be then reduced significantly and it was already very low because of non-efficient data acquisition. Merging the datasets was not straightforward, because of time-stamp shift between the DUT and telescope readout. Due to that no border columns or rows were rejected from the clusterization for the 2016 prototype. The clusters were reconstructed from the whole 8×36 pixels and then these clusters that contained any border pixel were discarded from the analysis. This approach allowed to keep a minimum needed statistics.

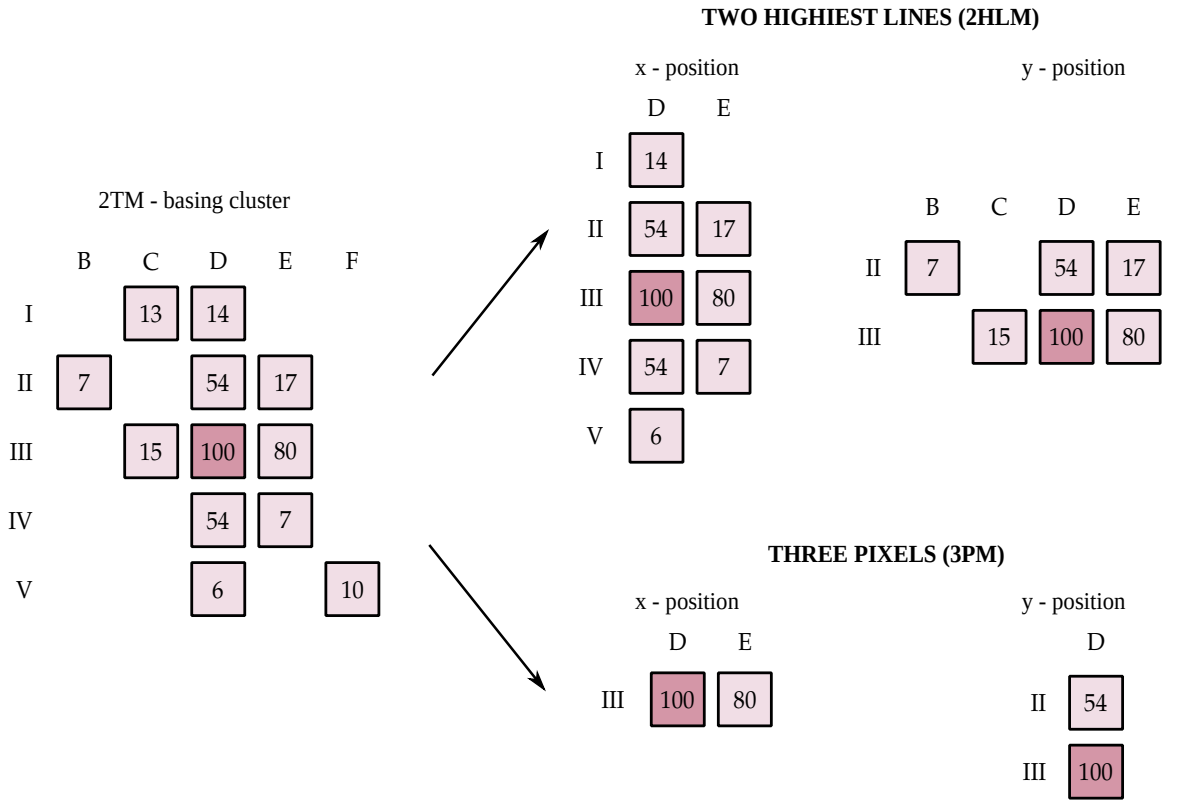

FIGURE 4.5: 2TM clusterization modification. Both of presented methods are reducing the 2TM cluster size and they are taking different pixels sets for x and y position calculations.

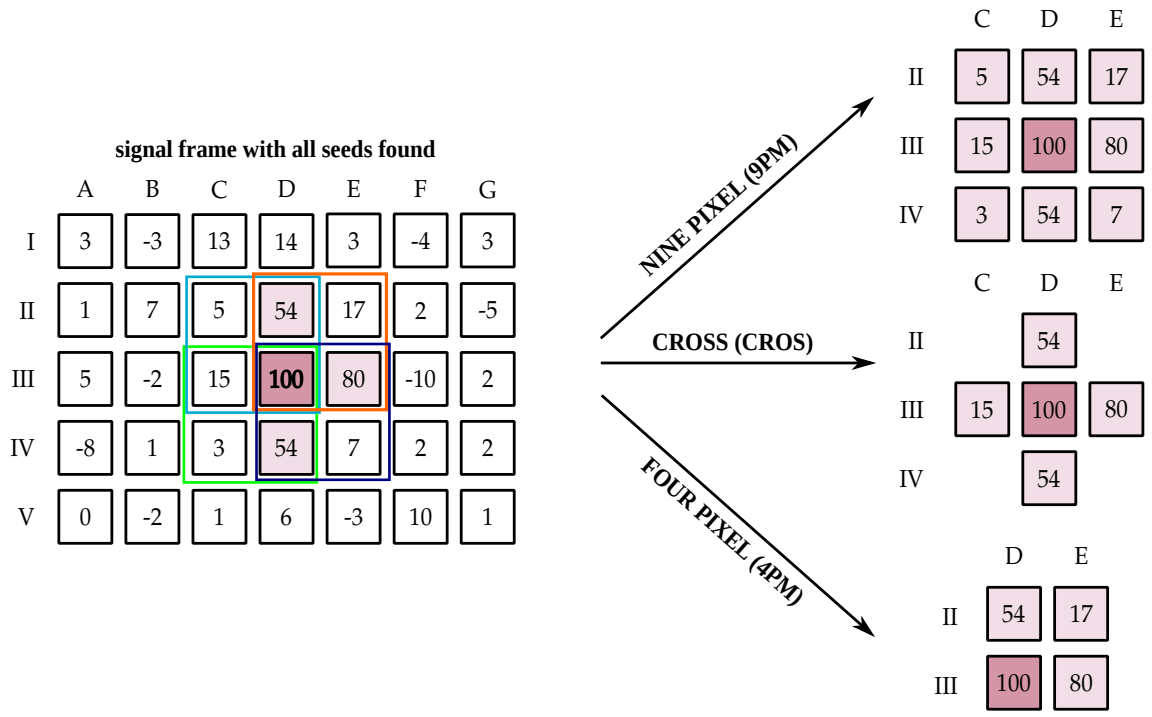

FIGURE 4.6: 9PM, 4PM and CROS clusterization algorithms with $th_{\text{seed}} = 20$. Pixels fulfilling this condition are marked on violet color with the darkest one as the seed. Colored squares corresponds to potential options for 4PM cluster forming.

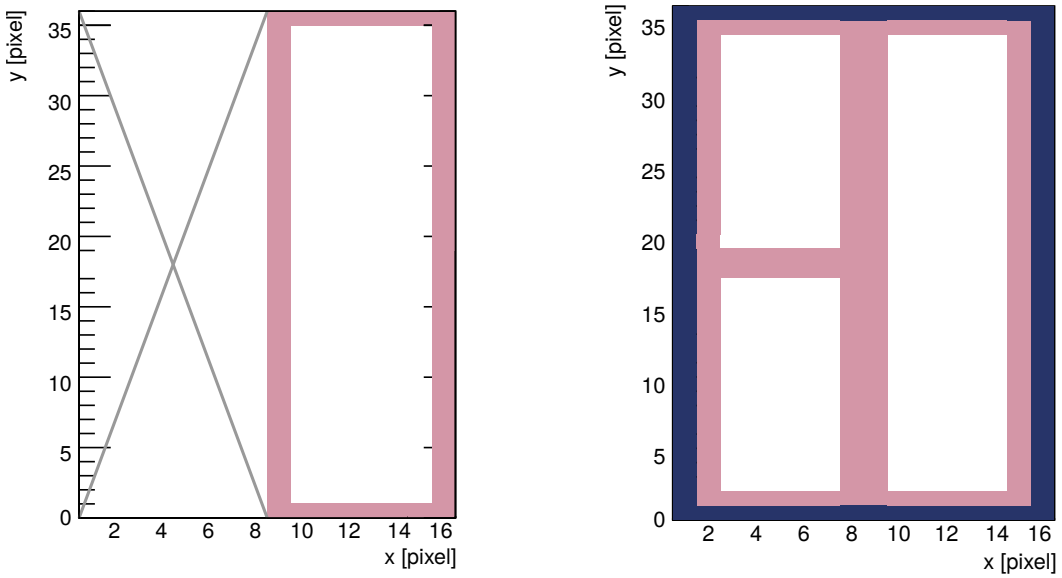

(A) 2016 year approach

(B) 2017 year approach

FIGURE 4.7: Area selection strategies. The violet area was an area of cluster reconstruction but when any pixel from this sector comes into cluster, the whole cluster was rejected from the analysis. The dark-blue area was completely discarded from the analysis.

In the 2017 design, the matrix was more homogeneous and the data statistics from test-beams was satisfactory. Because of that, edge columns and rows from whole matrix were completely discarded from the analysis as shown in Fig. 4.7B. The clusters that included any pixel from the remaining borders were also rejected, as in 2016 analyses.

4.5 Position finding algorithm and its correction

The charge spreading between several pixels known as a charge sharing effect is a major phenomenon allowing to improve spatial resolution performance of a detector. Thus, the charge distribution over neighbouring pixels is a crucial issue to be understood. First naive approach might assume that the charge distribution is linear. For such a case the COG position-finding algorithm would work properly. It is defined as:

$$x_{\mathrm{COG}} = \frac{\sum_{i=1}^{N_{cl}} x_i S_i}{\sum_{i=1}^{N_{cl}} S_i} \tag{4.2}$$

where sums go over all pixels in cluster N_{cl} and x_i is a position of i'th pixel and S_i denotes to its signal as defined previously Eq. 4.1. Nevertheless, experimental measurements show that charge distribution over neighboring pixels is far from linear. The diffusion phenomenon, earlier discussed in Sec. 2.2.2 on the page 24, is smearing out the charges trajectories.

Already in 1983, Belau et. al. have studied the charge distribution between two strips in a silicon detector and have introduced nowadays well-known η-variable [52]. Ten years

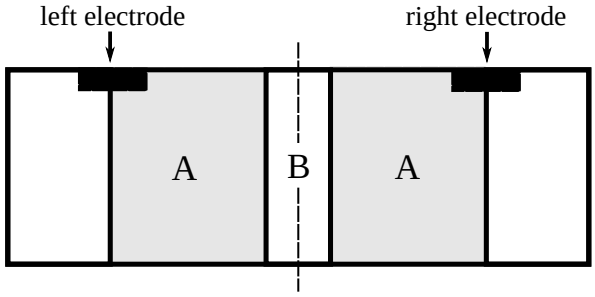

FIGURE 4.8: Sketch of two-electrode detector with definition of A region with no charge sharing and B with charge division [53]. Electric field forces charges on each side of the border to drift towards the closest electrode.

later in 1993, R. Turchetta has analysed the spatial resolution of silicon microstrip detectors and has proposed several position finding algorithms [53]. The short review of key points from these two works are presented below since presented there theoretical assumptions are permanently a groundwork of spatial resolution studies.

In the Fig. 4.8 two-strip case is presented with two electrodes and contractual areas labeled by A and B. A few decades ago the strip pitch was usually much bigger than the diffusion cloud, therefore one may consider the A region as an area where no charge sharing takes place and the B region where charges spread between two electrodes. Belau is defining η-variable as [52]:

$$\eta = \frac{S_r}{S_l + S_r} \tag{4.3}$$

where S_l and S_r are the pulse heights on left and right electrode respectively as marked in Fig. 4.8.

The Monte Carlo simulated η-variable distribution with no capacitive coupling and noise switched off is presented in Fig. 4.9A. The two peaks at $\eta = 0$ and $\eta = 1$ correspond to particle impact position falling on A region in Fig. 4.8. The middle part of this function comes from charge sharing between two electrodes. The shown η-variable distribution for non-ideal case differs in terms of peaks positions and widths. The electrode capacitive coupling moves peaks toward centre $\eta = 0.5$ and noise smears the peak out as shown in Fig. 4.9B.

Let us assume, for the beginning, linear charge sharing. Then hit position x_{COG} for two-electrode case using definition in Eq. 4.2 is:

$$x_{COG} = \frac{S_l x_l + S_r x_r}{S_r + S_l} = p \cdot \underbrace{\frac{S_r}{S_r + S_l}}_{\eta} + x_l \tag{4.4}$$

where:

p — pixel pitch

S_l, S_r — signal collected on the left and right pixel respectively

x_l, x_r — position of the left and right pixel respectively, while $x_r = x_l + p$

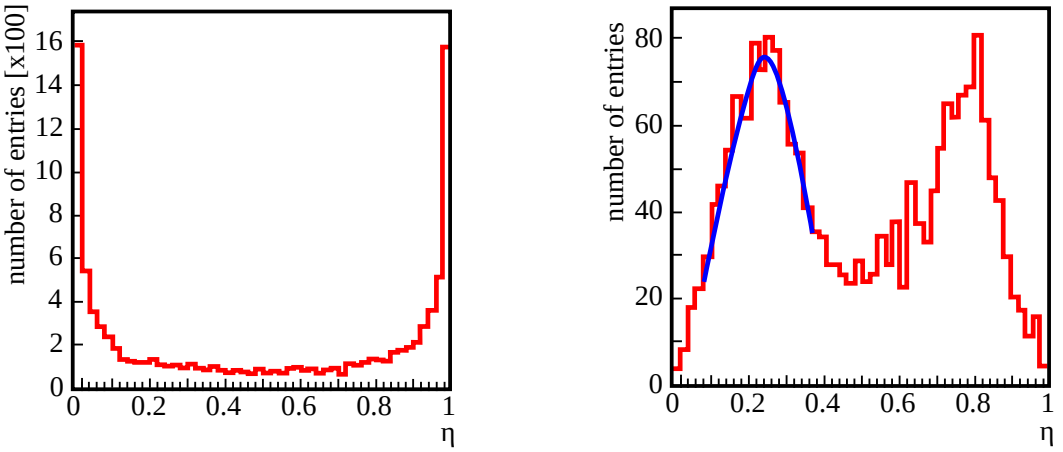

(A) Monte Carlo simulation in the absence of noise and capacitive coupling.

(B) Experimental distribution for 50 µm strip detector and SNR = 10.

FIGURE 4.9: Distributions of the η-variable from work [53].

As mentioned earlier, because of diffusion the position is not a linear function of energy distribution between two electrodes and COG algorithm does not provide precise result. Thus, the correction procedure, known as the η position finding algorithm [53], has to be applied. According to this method, the particle impact point x_η is as follows:

$$x_\eta = p \cdot f(\eta) + x_l \tag{4.5}$$

where $f(\eta)$ is an arbitrary monotonic growing function with $f(0) = 0$ and $f(1) = 1$, called further correction function. Assuming that hits are uniformly distributed over the detector, one can extend above equation to:

$$x_\eta = p\frac{\int_0^{\eta_0} \frac{dN}{d\eta} d\eta}{\int_0^1 \frac{dN}{d\eta} d\eta} + x_l = p \cdot f(\eta_0) + x_l \tag{4.6}$$

where $\frac{dN}{d\eta}$ is the differential η distribution. The Eq. 4.6 defines $f(\eta_0)$ as the normalized cumulative function of η-variable distribution. All above considerations regard the two-electrode case, what was obvious situation when the strip (pixel) size was relatively large.

4.5.1 Multi-pixel η-correction - standard algorithm modification

Nowadays, when pixel size goes smaller and smaller it is common to have a multi-pixel clusters, especially using clusterization method such as 2TM described previously. The following studies present the position finding algorithm for data sample containing clusters of various sizes. It is directly basing on η-position correction proposed by [52, 53] and thus it is further called a multi-pixel η-correction (mp-η). The modification concerns a form of correction function mentioned in Eq. 4.5.

Hence, define new variable ζ_{COG} as the COG position projected into a pixel pitch:

$$\zeta_{COG} \equiv x_{COG} \pmod p \tag{4.7}$$

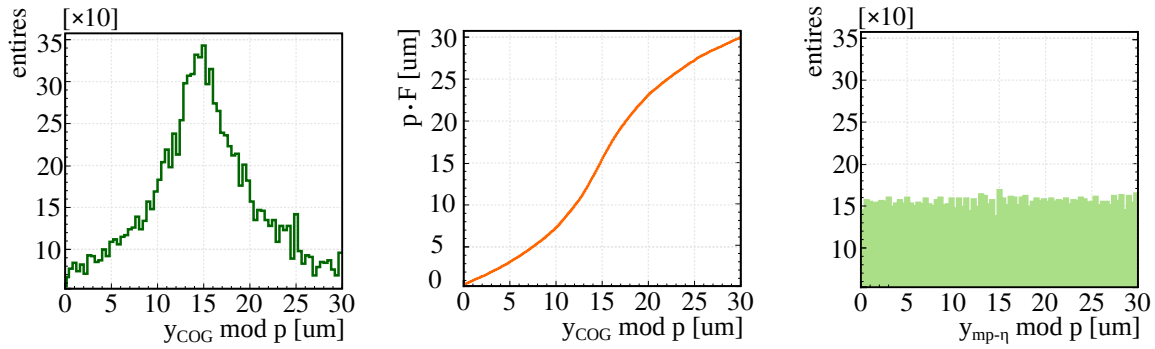

(A) COG-positions projected to pixel pitch

(B) Position correction function

(C) mp-η positions projected to pixel pitch

FIGURE 4.10: Example chain of analysis steps proposed for multi-pixel cluster η-correction for source follower matrix on the FZ-n wafer at 130 V for 2TM-10-2.

where $\zeta_{COG} \in (0; p)$. The ζ_{COG} distribution, which is simply in-pixel hit position distribution, is further denoted as $P(\zeta_{COG})$. The exemplary distribution from the test-beam data is presented in Fig. 4.10A. For the data sample containing clusters of different sizes, the proper assumption is that the particles impact points have to be uniformly distributed over the pixel pitch, when the detector was homogeneously irradiated. The proposed algorithm is basing on making uniform the $P(\zeta_{COG})$ by using the correction function defined in Eq. 4.8.

$$F(\zeta_{COG} = \zeta) \quad = \quad \frac{\int_0^{\zeta} P\left(\zeta_{COG}\right) \mathrm{d}\zeta_{COG}}{\int_0^{p} P\left(\zeta_{COG}\right) \mathrm{d}\zeta_{COG}} \tag{4.8}$$

It is easy to notice, that the proposed $F(\zeta_{COG})$ is a normalized cumulative of $P(\zeta_{COG})$. The exemplary correction function is shown in Fig. 4.10B with $F(\zeta_{COG})$ denoted as F for simplicity. To calculate the corrected position $x_{mp-\eta}$ one has to apply the proposed $F\left(\zeta_{COG}\right)$ correction function in the basic Eq. 4.5:

$$x_{mp-\eta} = p \cdot F\left(\zeta_{COG}\right) + x_l \tag{4.9}$$

The effect of proposed correction on experimental data, presenting in-pixel hit position distribution $P(\zeta_{x_{mp-\eta}})$ after mp-η correction, is shown in Fig. 4.10C.

The analogous plots to these in figures 4.10A–4.10C but shown for different detector types and both tested detector wafers are presented in Fig. 4.11. For the FZ-n wafer, for which the statistics is large and datasets contain all cluster sizes except one-pixel cluster, the proposed procedure successfully spreads the hit positions uniformly within a pixel pitch. For the DSOI-p wafer the presence of single pixel-clusters is resulting with a sharp peak in the middle of the distribution. The influence of this peak on correction function causes "gaps" on the in-pixel hit position distributions after mp-η correction. The non-symmetry of these gaps in relation to the pixel centre is mainly caused by cross-talk effect, suspected to affect data in x direction.

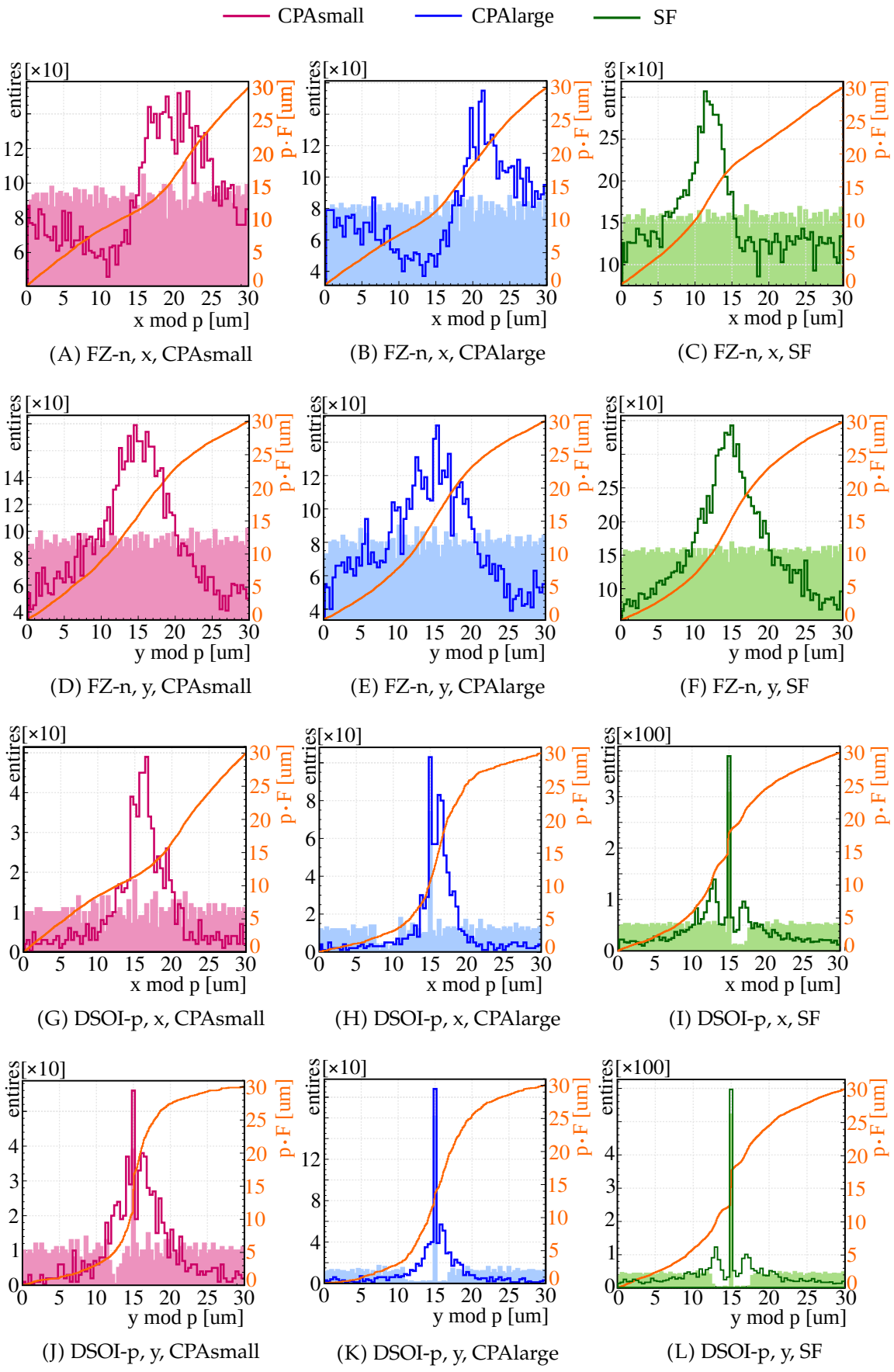

(A) FZ-n, x, CPAsmall (B) FZ-n, x, CPAlarge (C) FZ-n, x, SF

(D) FZ-n, y, CPAsmall (E) FZ-n, y, CPAlarge (F) FZ-n, y, SF

(G) DSOI-p, x, CPAsmall (H) DSOI-p, x, CPAlarge (I) DSOI-p, x, SF

(J) DSOI-p, y, CPAsmall (K) DSOI-p, y, CPAlarge (L) DSOI-p, y, SF

FIGURE 4.11: In-pixel hit position distribution for the FZ-n (top two rows) and the DSOI-p (bottom two rows) at 130 V and −70 V back bias voltage respectively (2TM-10-2). The middle point of the distribution corresponds to the centre of the pixel.

4.5.2 Cross-talk effect

The insight into plots in Fig. 4.11 provides important information about quality of the data and physical effects that are happening in the detector. The first observation is that for the FZ-n wafer the x coordinate shows a significant asymmetry in $P(\zeta_{\mathrm{COG}})$. This effect is most probably caused by the pixel layout-connected issues. The details on this topic would not be introduced here, since the author of this thesis have not designed the sensor and these studies are a part of another work. It is enough to say, that there are specific asymmetries in x direction in the pixel layout, that probably cause cross-talk effect.

The asymmetry revealed as a bump on one side of the distribution with respect to the centre of the pixel. In addition, direction of this distortion is opposite on the charge preamplifiers and source followers shown respectively in figures 4.11A, 4.11B and 4.11C. This is caused because the signal on source follower is positive and on charge preamplifier negative, therefore the layout-caused cross-talk effect is a mirror effect. The additional observation is that the cross-talk contributes much less the DSOI-p wafer than the FZ-n, but is still present, what can be seen in figures 4.11G, 4.11H and 4.11I.

4.6 Track-hit correlation algorithm

Before spatial resolution and efficiency studies, the telescope tracks have to be matched in pairs with proper DUT hits. Graphical representation of the proposed algorithm for pair correlation is presented in Fig. 4.12.

The track data collection is treated as the reference, so the algorithm is basing always on finding a proper DUT hit to each track, not opposite. In order to minimize track collection, the telescope area is limited to the DUT area enlarged of 5 pixel pitches (150 µm) from each side. For spatial resolution calculation, the DUT hits reconstructed on matrix borders are discarded from the analysis. Also the so-called reset-affected cluster, which might have been affected by the detector dead time, are rejected. However, this improvement is done only for 2017 data and it is in details considered further in Sec. 4.7.

For each track the condition of time correlation is verified and it is performed between particular track and all DUT hits. The track ToA (t^T) has to be in the range of two frame times (W) from DUT time-stamp (t^D). The value of W is known roughly from the readout firmware. The demand of taking two frame times comes from rolling-shutter specifications and is also explained further in this work. The time correlation condition for an i'th track is thus defined as:

$$t_j^D - W \leq t_i^T \leq t_j^D + W \tag{4.10}$$

Since there can be a small shift between telescope and DUT timing, the W value is extended by 10 %.

Here, it has to be explained that slightly different approach is applied in 2017 data. The off-line reset-affected clusters analysis allowed to improve the time-stamping of the DUT by attaching the time-stamp to each row of the matrix. In addition also the precise W value is extracted. To gain these improvements, the analysis is firstly run with condition given in

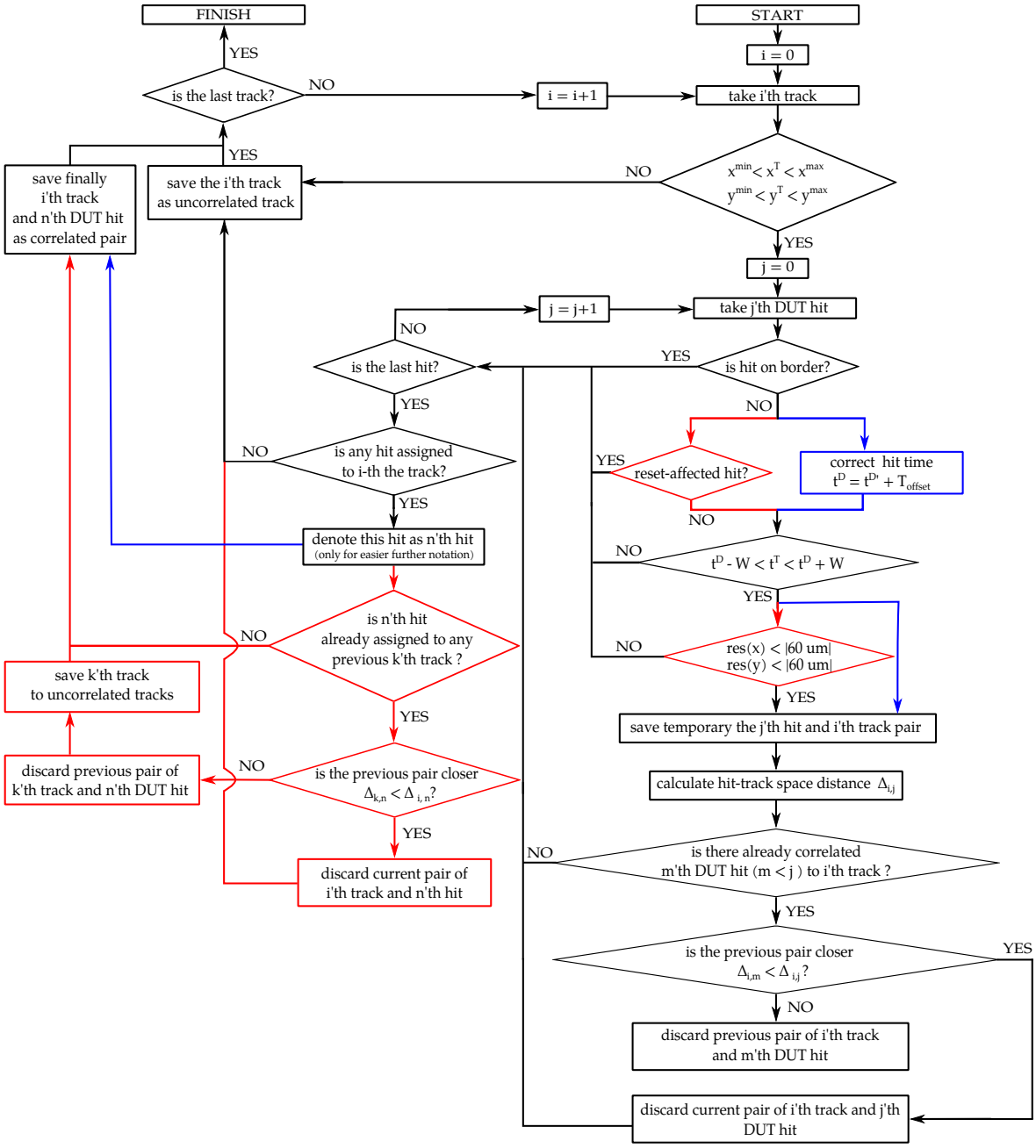

FIGURE 4.12: Graphical algorithm of telescope tracks and DUT hits pairing for spatial resolution studies. The blocks marked with blue color regards analysis only from 2016. There was a time-offset between telescope and DUT time-stamping and T_{offset} is a time correction needed to be applied for raw DUT time-stamp $t^{D'}$. The blocks in red frames regard analysis from 2017 year. The analysis was upgraded about reset-affected clusters rejestion and also there was no time-shift in detectors timing.
The used symbols denote to: $x^{min/max}$ and $y^{min/max}$ – constrains put on telescope area, discarding tracks being about 150 µm away from DUT borders, t^D - DUT time-stamp, t^T – track ToA, W – frame time, x^D and y^D – DUT hit x and y positions, x^T and y^T – track x and y positions, $res(x)$ and $res(y)$ – residuum value in x or y.

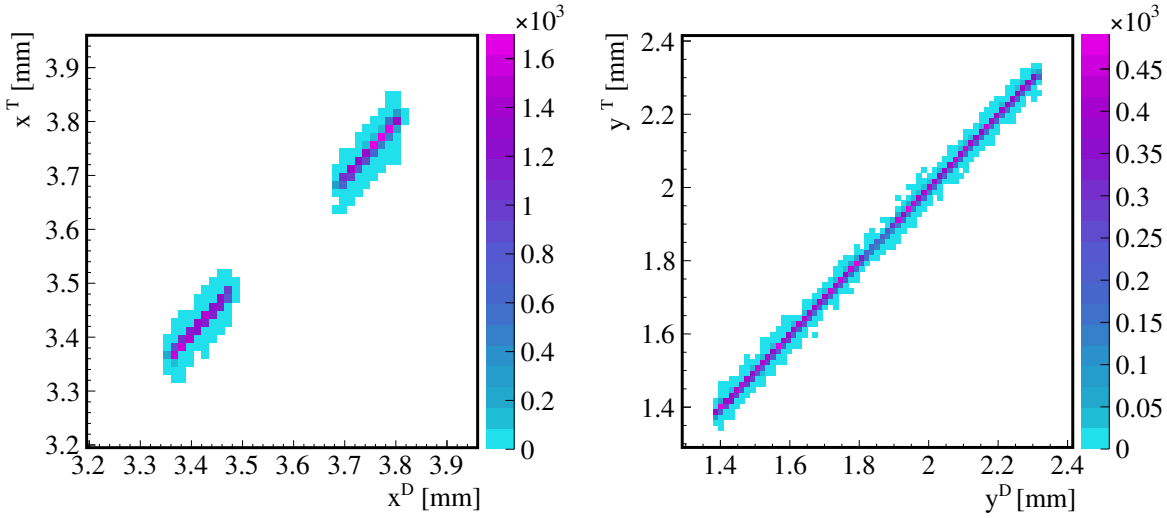

FIGURE 4.13: Track-hit positions correlation for x (left) and y (right) coordinate. Example shown for the FZ-n wafer. The gap in x is coming from physical gap between charge preamplifiers and source followers matrices.

Eq. 4.10. After this preliminary step, one obtains DUT hits row time $t^{D-\text{row}}$ and exact frame time W^{clock}. It has to be clearly explicated, that it is enough to perform this preliminary step only two times per whole analyses (once for each used readout frequency clock). All the next iterations for 2017 prototype are done using following condition:

$$t_j^{D-\text{row}} \leq t^T \leq t_j^{D-\text{row}} + W^{\text{clock}} \tag{4.11}$$

If a j'th DUT hit does not meet time correlation condition with i'th track, the next hit (j+1)'th is checked. When none of the DUT hits have passed time condition, the track is marked as the uncorrelated track. If the time correlation condition is fulfilled the spatial distance ($\Delta_{i,j}$) between track and DUT hit is calculated:

$$\Delta_{i,j} = \sqrt{\left(x_i^T - x_j^D)^2 + (y_i^T - y_j^D\right)^2} \tag{4.12}$$

where x_i^T and y_i^T correspond to i'th track positions in x and y respectively and x_j^D and y_j^D to the j'th DUT hit positions. The spatial distance $\Delta_{i,j}$ is used to find the closest DUT hit if there were more than one correlated in time. Finally, the closest DUT hit is matched with the track. In Fig. 4.13 the exemplary positions correlations between paired hits and tracks are shown.

In 2017 test-beam analysis the additional condition of residuum value less than 60 µm is introduced which corresponds to the distance between track and hit not larger than two pixel pitches. Also in 2017, for each track that was paired with the DUT hit, the algorithm verifies whether this particular DUT hit has been already assigned to any other track. In such a case the pair with smaller $\Delta_{i,j}$ is saved in the final data collection. This step may generate artificially uncorrelated tracks, because there might be other DUT hit matching this track that passed time condition, but was eliminated during finding the closest pair. This situation

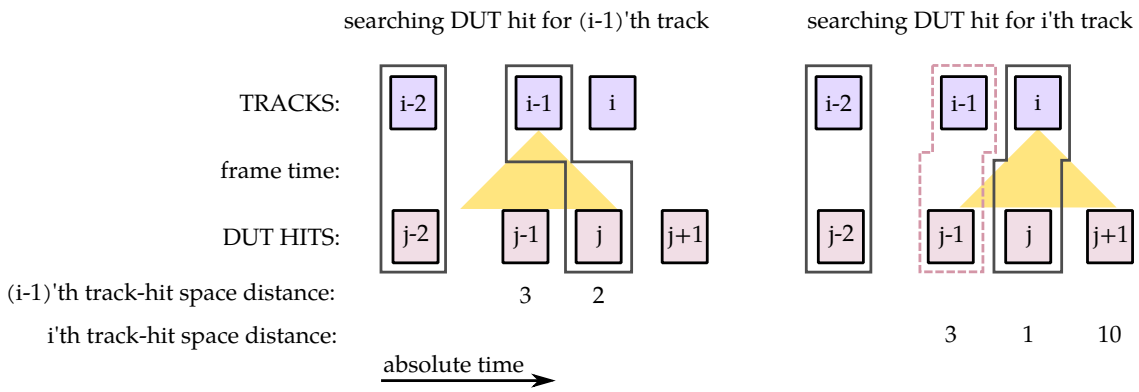

FIGURE 4.14: Graphical scheme presenting artificialy uncorrelated track source. The yellow color corresponds to frame time window. The pair in dashed violet curved is not correlated in stanard procedure of track-hit correlation, but it should be paired.

is graphically presented in the Fig. 4.14. To solve this issue, the correlation procedure as described above is done once more after the standard correlation procedure is finished. For this iteration, the algorithm is working on uncorrelated tracks and uncorrelated DUT hits data collections. The number of matching pairs from uncorrelated collections is on the level of about 0.01 % of full statistics.

As it was mentioned at the beginning of this paragraph, the correlation conditions are slightly different when efficiency of the detector is studied. However, these modifications are described when considering the test-beam results, since the justification of implementing these changes are then clearly visible.

4.6.1 Time-offset finding

For the 2016 test-beam there was no compatibility between the DUT and telescope events time-stamping. Moreover, the DUT had often breaks in the DAQ, because of data buffer overfilling. Both of these problems made the time correlation between track and hits not straightforward. In Fig. 4.15 the piece of spil structures for the DUT and the telescope are shown. The Fig. 4.15 shows in principle the hit rate in function of time. The time shift between spil structures as well as the data collecting breaks can be observed.

The naive approach would be to calculate time-offset via comparing a single-spil structure from the DUT and telescope and assess the shift between them. Nevertheless, since the data acquisition problem occurred also at the beginning of the spil, such a procedure cannot be applied. In addition, because of significantly larger area, the telescope records signals that are out of the DUT range, even after telescope area limitation which is a rough procedure. Thus the spil of the telescope may be wider than the DUT spil. Because of that, all spils from particular detector are merged together, what is presented in Fig. 4.16A. The strange shape of the DUT merged spils comes from problems with the DAQ. A difference of mean values of merged spils becomes a rough time-offset estimation. Nevertheless, as it was verified in the analysis, such a time-offset is not precise enough to successfully correlate the telescope tracks with the hits.

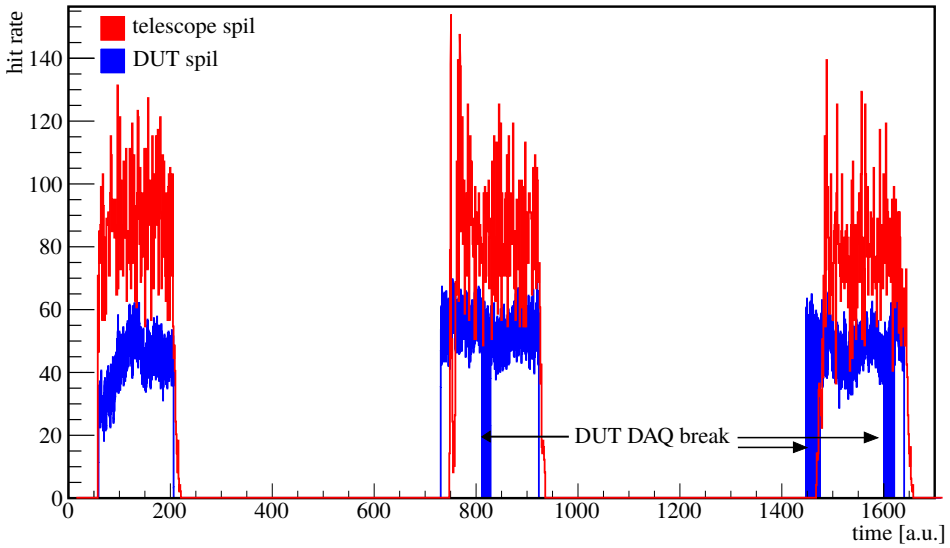

FIGURE 4.15: Fragment of spil structure for exemplary dataset. The DUT had a significant breaks in the DAQ and this effect is observed as a zero-entries on blue spil-structure.

To find the precise time-offset, let us consider a spil structure as a set of a square areas. It means that one spil is simply treated as a square of edges equal to the hit-rate value and spil duration time. If the time-offset between the DUT and telescope would be zero, a spil-squares for the DUT and telescope should overlap. Thus, if there is no time-offset, the parameter calculated as the product of spil-areas from DUT and telescope should give the maximum value. In order to find the time-offset, the DUT spils structure is shifted by a small time periods. After each shift, the product of spil-area is calculated. In practice, the hit rate values for each two corresponding bins from exemplary Fig. 4.15 are multiplied by each other and the sum of the products is calculated. The result of this procedure is shown in Fig. 4.16B. The time shift for maximum value on this distribution is a precise time-offset correction to the rough time-offset value. The sum of rough time-offset and its precise correction is a final time-offset that is applied for all time-stamp values of the DUT frames. The time-offset values are in the range from 0.5 s to 1 s.

4.7 Effects of rolling-shutter readout

The rolling-shutter readout connected issues significantly influence on quality of cluster reconstruction. It is important to understand deeply the mechanics of this problem because it may worsen the efficiency and spatial resolution performance.
Two phases are characteristic for the rolling-shutter readout for each row:

1. readout phase — during this phase the charge from pixels in a single row is transferred out from the matrix. Then the reset of the row is done and also everything connected with initial setting of the pixels electronics. This stage is generating a dead time since the whole row is insensitive to particles. The reset of the next row begins when the data from current row are sent out of the chip. Due to that there is a time gap between reset phases of two neighbouring rows.

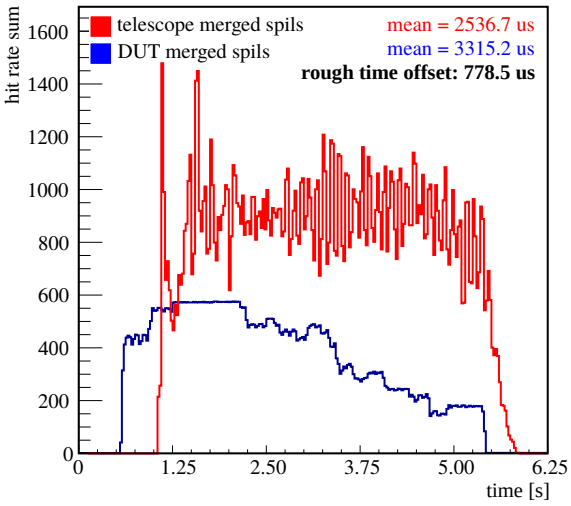

(A) Merged spil structure for telescope and DUT. The irregular shape of the DUT spil structure comes from break in the DAQ.

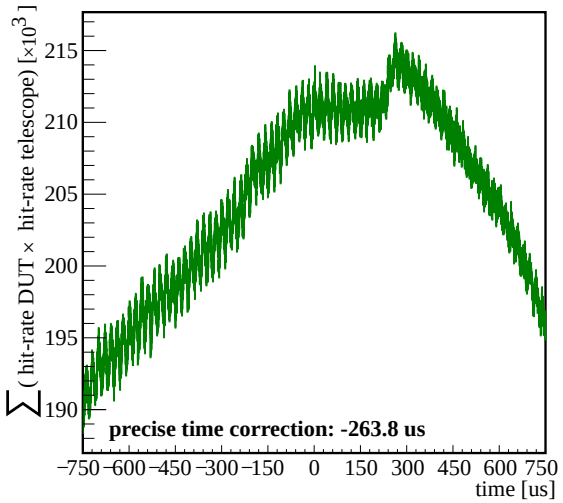

(B) Product of spil-area structures. The time-shift for maximum value corresponds to maximum overlapping of the DUT and telescope spil structure.

FIGURE 4.16: Finding time-offset between DUT and telescope time-stamping.

2. integration phase — it starts after resetting of particular row. Pixels are sensitive for incoming particles.

The disadvantage of rolling-shutter readout is a possibility that charge generated by one particle will be recorded in two consecutive frames with different time-stamps attached. Such a cluster may also have artificially reduced energy, because part of the charge can be lost due to dead time. In Fig. 4.17 the major unfavorable cases of reset-affected clustering options are graphically depicted.

In this simple example 3×3 pixel matrix is considered. The different colors (violet, blue) correspond to affiliation to frame with time-stamp T_0 or T_1. On the right side of each timing scheme the matrix picture is depicted indicating which pixels have collected charge and during which frame. Since the time diagrams are shown only for rows, on the matrix sketches the charge sharing is symbolically spread also into 3 columns in order to visualize real two-dimensional situation.

The simplest and most desirable situation is depicted in Fig. 4.17A, where charge is distributed over rows that have been already reset. In such a case entire cluster with full available energy is stored in a single frame. In the all next examples charge is spread between two frames. One has to notice that there is no possibility to divide single-particle charge between more than two frames.

In Fig. 4.17B a particle comes between reset phases of two neighbouring rows. Thus, although particle time of arrival t_{ToA} is larger than time-stamp T_0 part of its charge will go to frame with T_0 time-stamp and part to T_1. This is an unintuitive issue coming from rolling-shutter readout.

The next possible situations presented in Fig. 4.17C and 4.17D assume that the particle charge collection time is overlapping with the reset stage of a particular row. In such a case cluster is divided into two frames with different time-stamps as in the previous example. In

addition, a part of the charge is lost, since the charge is drifting towards the pixels that are insensitive for charge collection. The ratio of charge collection time to dead time determines how much charge is lost. For the case in Fig. 4.17C the seed pixel charge is lost so spatial resolution performance may suffer the most. Nevertheless, both consecutive frames have collected enough charge to reconstruct cluster. The specific feature of such clusters is that they are sharing the same row in both frames, which is also unintuitive effect. Slightly different effect is a result of the last scheme in Fig. 4.17D. The overall charge generation is smaller, thus the charge spreads only on two rows. In such a case only one cluster may be reconstructed (frame with time-stamp T_0) with significantly reduced energy in relation to true charge deposition. It may also happen that whole collected signal is too small to pass clusterization conditions and in such a case cluster will be completely lost.

Both cases 4.17C and 4.17D are especially unfavorable for the efficiency calculation. The first situation may introduce redundant clusters coming from one particle and thus, increasing artificially the efficiency. On the other hand, the second case may lead to losing clusters completely, decreasing the final efficiency value.

4.7.1 Reset-cluster rejection

In order to eliminate reset-affected clusters one has to reconstruct the reset time of each row. This timing information may be extracted from hardware side in the most straightforward approach. Although when this is not possible, there is a possibility to extract offline reset-timing using test-beam data.

The first step is to select the data sample containing only reset-affected clusters. The algorithm is basing on the fact, that reset-affected clusters have weak spatial resolution and artificially reduced energy.The clusterization procedure with the lower seed condition ($th_{\text{seed}} = 5$) is performed to reconstruct also clusters with very low energy. The second assumption is that the reset-affected hits have a weak spatial resolution, so they have to contribute to the tails of the residua distributions. Tail entry is defined as the DUT hit with spatial resolution above 10 µm:

$$|x^T - x^D| \geq 10\ \mu\text{m} \ \vee \ |y^T - y^D| \geq 10\ \mu\text{m} \tag{4.13}$$

where x^T and y^T are tracks position in x and in y and x^D and y^D are analogically DUT hit positions. Since the reset is going row-by-row, the y direction would be affected the most and in the further studies only the y tail entries are considered.

The energy spectrum plotted in Fig. 4.18A presents the comparison of the whole dataset spectrum (line) with the y tail entries (area). Low-energy peak on the spectrum is fully covered by the tail entries. Since only the track correlated DUT hits are used, one may be sure that there are no random entries and low energetic peak comes from the reset and not from noise. For further verification, also the cluster size in y direction is plotted in Fig. 4.18B. The smallest single-pixel size clusters come fully from the tail entries. Thus, applying cuts for residuum value in y direction and for cluster energy value allows to select the data sample containing only reset-affected clusters. For such a data sample the correlation between y position and their timing is expected, since the reset phase occurs periodically. To verify this

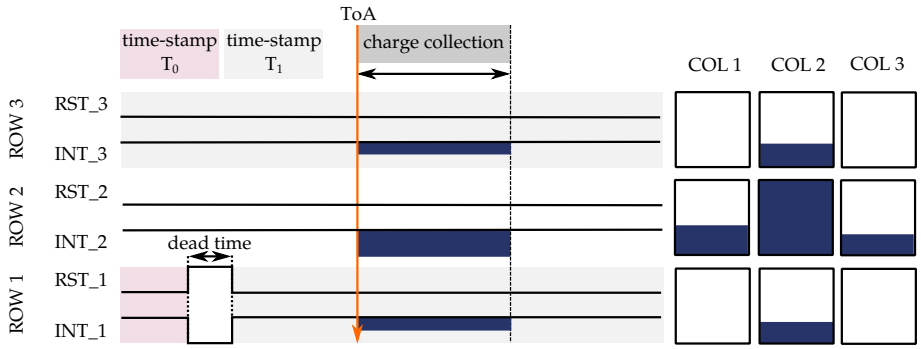

(A) Charge stored in the same frame.

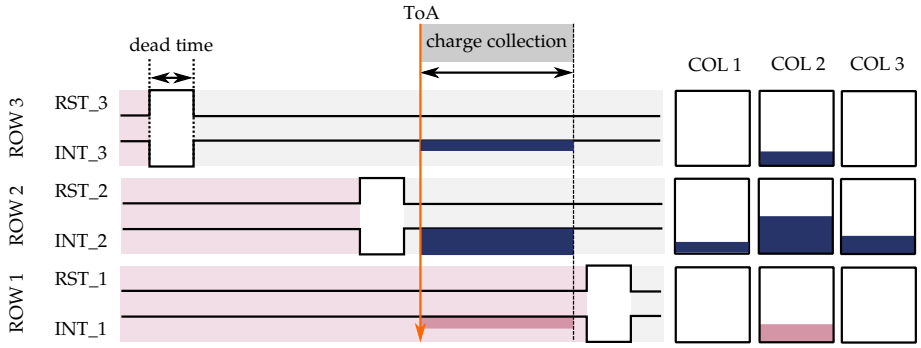

(B) Charge divided into two frames.

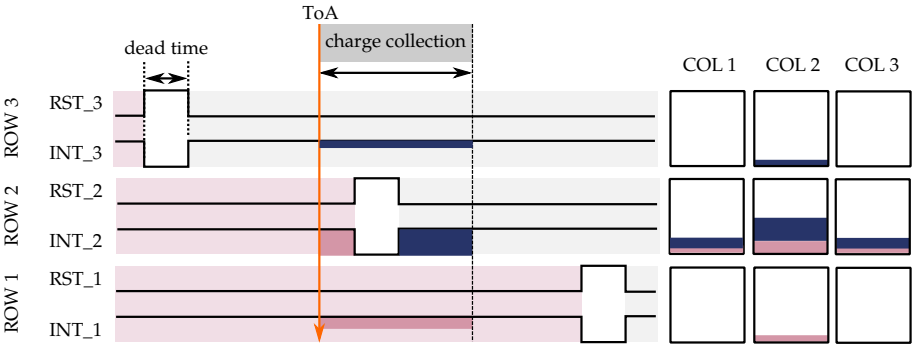

(C) Charge divided into two frames and seed charge partially lost.

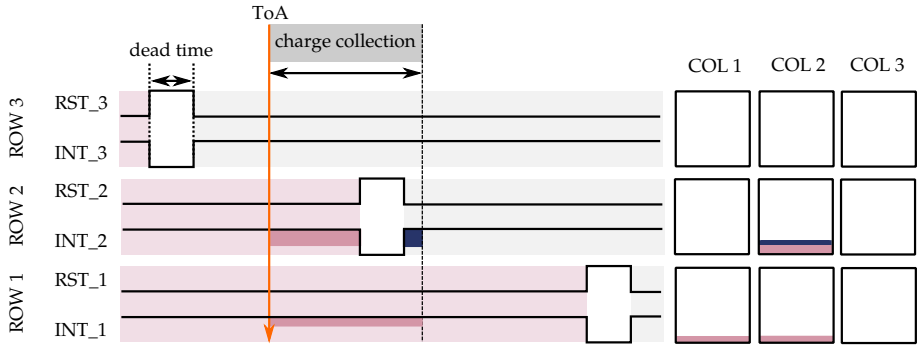

(D) Charge divided into two frames and almost all charge lost.

FIGURE 4.17: Specific cases of rolling-shutter readout infulence on cluster reconstruction distortion. Sketch is an ideological drawing, thus scales are not preserved. Different color (violet, blue) corresponds for frames with various time-stamping (T_0, T_1). High states of *RST* and *INT* correspond to active reset and integration time respecitively.

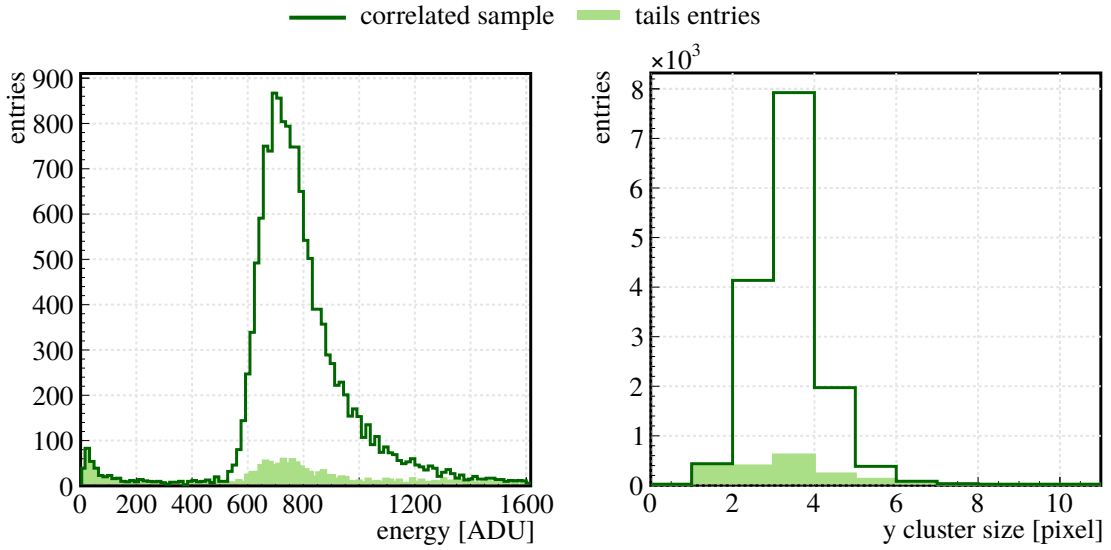

(A) energy spectrum (B) y cluster size

FIGURE 4.18: Comparision of whole data sample (line) and residua tails entries (area) for correlated track-hits collection. Example is shown for SF matrix on the FZ-n, but the same behaviour is observed for CPA.

theory, a new variable is introduced:

$$\tau = t^D - t^T \tag{4.14}$$

where t^D is DUT hit time-stamp and t^T is track ToA. Since t^D may be interpreted as a beginning of the reset phase of the first row in the matrix and t^T as a true particle arrival time, the difference of these two values τ has to be constant for each row, when only reset-affected clusters are analysed. The relation of τ versus DUT hit y position for data sample limited as mentioned above is presented in Fig. 4.19 and the strong linear correlation is visible. Since the reset-affected clusters are spread into two consecutive frames, the two lines in Fig. 4.19 correspond exactly to two different frames affiliation. Extracting τ versus y position relation allows to obtain an universal formula for finding the reset time of particular row. The linear fits to τ relation for specified readout frequency clock are given below:

$$\tau_1 = a_1^{6\text{MHz}} \cdot r + W_1^{6\text{MHz}} = -3.77 \cdot r + 3.45 \text{ µs} \tag{4.15}$$

$$\tau_2 = a_2^{6\text{MHz}} \cdot r + W_2^{6\text{MHz}} = -3.86 \cdot r + 139.2 \text{ µs} \tag{4.16}$$

where r denotes to row number (or y hit position in more exact approach). The bottom index correspond to particular frame time lines and top index to approximate readout clock frequency. The difference between $W_1^{6\text{MHz}}$ and $W_2^{6\text{MHz}}$ parameters allows to extract the frame time for 6 MHz frequency readout clock:

$$W^{6\text{MHz}} = W_2^{6\text{MHz}} - W_1^{6\text{MHz}} = 135.75 \text{ µs} \tag{4.17}$$

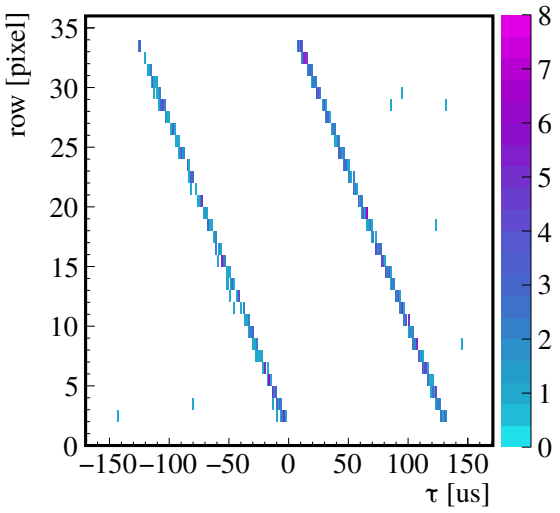

FIGURE 4.19: τ (hit time-stamp - track ToA) versus hit y position made for the y residuum tail entires of energy below 500 ADU. Example shown for SF on the FZ-n wafer and clusterization method 2TM-5-2.

Similar procedure is done for 12.5 MHz readout clock as follows:

$$\tau_1 = a_1^{12.5\text{MHz}} \cdot r + W_1^{12.5\text{MHz}} = -1.72 \cdot r + 2.72\ \mu\text{s} \quad (4.18)$$

$$\tau_2 = a_2^{12.5\text{MHz}} \cdot r + W_2^{12.5\text{MHz}} = -1.72 \cdot r + 63.14\ \mu\text{s} \quad (4.19)$$

$$W^{12.5\text{MHz}} = W_2^{12.5\text{MHz}} - W_1^{12.5\text{MHz}} = 61.42\ \mu\text{s} \quad (4.20)$$

These relations allow not only to remove the reset-affected clusters from the spatial resolution studies by applying a proper cut for τ variable but also to attach the time-stamps to each row of the DUT matrix. Thanks to that the correlation is performed using the row time not frame time which allows to obtain higher accuracy. All the low-energy entries and single-pixel y clusters are discarded after introducing the proposed procedure.

Removing the reset-affected clusters decreases the standard deviation of the residua distributions of about 25 % to 33 % but does not remove the tails completely. This step is made only for 2017 prototype test-beam analysis. In case of 2016 this was not done and reset-affected clusters may influence on final spatial resolution results. The main reason was that there were more difficulties and problems and such a detailed analyses have not been done.

The reset-affected cluster rejection is done only for spatial resolution studies. For this case removing reset-affected cluster is done after track-hit correlation phase and thus it only limits the statistics, but does not bias the data sample.

Detector dead time and the detector efficiency

For the efficiency calculation the proposed algorithm would not work properly. To calculate the efficiency one has to divide number of all correlated DUT hits by the number of all particles passing through the DUT, which is simply number of track reconstructed by the

telescope. Since the proposed algorithm may successfully clear DUT correlated data collection data sample from the reset-affected clusters, it is not obvious how to clear up the raw telescope data sample. One has to remove tracks falling on the DUT reset time periods but only for some telescope area corresponding to particular DUT row. Fixing this area cannot be clearly determined, since there is no straightforward relation where the track will occur in correspondence to DUT hit. Limiting too much or too little the telescope plane will artificially affect efficiency value. Thus, for efficiency analysis the reset-affected clusters are not removed from data sample.

Chapter 5

Beam-test results

There are several parameters that have to be considered to describe a detector performance. The most basic quantities are noise and signal to noise ratio (SNR). Depending on the application different properties are crucial but usually as low as possible noise is desired which also leads to the high SNR. In terms of the tracking detectors also a charge distribution is of the major interest. The studies of cluster size or in-pixel hit position allow to understand the charge sharing effect for a particular detector.

The most obvious particle detector parameter is its resolution, so the ability to reconstruct particular physical quantity. Since the tested DUT is targeted to fulfill the requirement of spatial resolution for the vertex detector for CLIC, the performed data analysis is highly focused on testing position reconstruction capabilities. Also the efficiency of a detector is always of high importance. It is expected that detector is able to restore information of all particles passing through its volume. This allows to properly reconstruct final state of physical events what is crucial in terms of elementary particle experiments.

Just as a reminder, the presented results were obtained with two wafer types: the Floating-Zone type n (FZ-n) and the Double SOI type p (DSOI-p). In addition, there were two different pixel readout architectures tested: source follower (SF) and charge preamplifier pixels (CPA). The charge preamplifier pixels were implemented with two different sensing diode sizes, therefore the results are shown for charge preamplifier with small sensing diode (CPAsmall) and with large sensing diode (CPAlarge). The matrix was 16×36 squared pixels of 30 µm size.

The test-beam allow to determine a spatial resolution and efficiency performance of the DUT, since a reference telescope data are available. This cannot be done in a laboratory environment when working only with radioactive sources or lasers. Thus, tests with beam provide a huge opportunity for in-depth detector performance studies. The data were acquired during tests with 120 GeV pion beam on the SPS at CERN. There were two test-beams done: in 2016 and 2017 year. As it was described earlier, since the 2016 prototype was treated as a preliminary test structure, the default results are shown for 2017 prototype. If the outcomes come from first 2016 test-beam it is clearly indicated in the text.

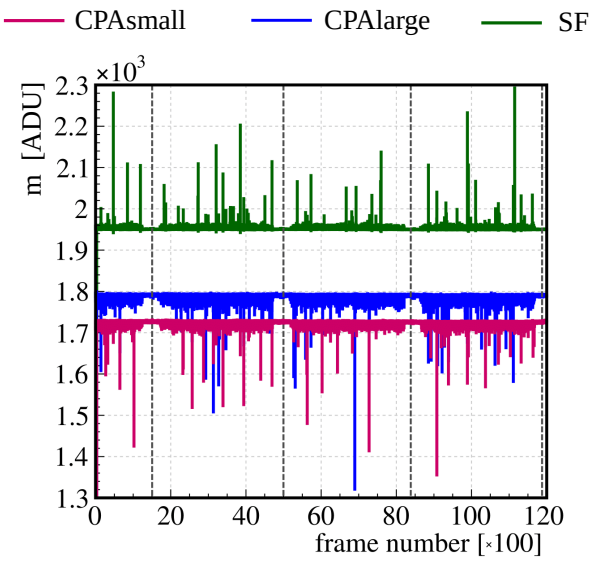

FIGURE 5.1: Frame baseline m with spil structure visible. The vertical dashed lines indicate time periods between spils. Since CPA is an inverting architecture and SF is not, theirs signals have opposite direction.

5.1 Baseline and noise

In the very first step of the analysis a baseline and noise are calculated for each pixel separately. Data were collected only when beam was present, so no calibration data sets are available. For this reason the calibration dataset has to be prepared off-line, basing on preliminary hits finding and rejecting frames with hits.

In order to find a frame that is suspected to have a pixel with signal induced by charged particle, let us define a frame baseline m. The frame baseline is a total raw signal calculated from particular frame divided by the number of pixels in the matrix. An example plot of frame baseline versus frame number is shown in Fig. 5.1. The mean $\overline{m}$ is the frame baseline averaged over 200 thousand frames. If any pixel in particular frame recorded a particle, this frame baseline m will deviate from $\overline{m}$. Thus, the frame is discarded from calibration sample, when its baseline m differs more than f_{disc} percentage from $\overline{m}$. The value f_{disc} is a parameter of the analysis and has to be adjusted to each matrix type since each pixel architecture may have a different baseline and signal values. Nevertheless, for 2017 beam-test data the condition of $f_{\text{disc}} = 2\,\%$ worked well for all matrices types allowing to successfully perform a preliminary hit rejection and to get a clean calibration sample. The described procedure of rejecting frames suspected to have a hit was performed iteratively to achieve high accuracy of the baseline and noise.

After getting a calibration dataset, the baseline spectrum for each pixel is generated as already shown for exemplary pixels in Fig. 4.3 on page 49. Mean value of the spectrum is taken as the pixel baseline and the standard deviation as the pixel noise given in ADU. Final exemplary maps showing baselines and noises are presented in Fig. 5.2.

The incomprehensible effect is observed on charge preamplifier matrix with large sensing diodes for the FZ-n wafers. The drop of the baseline together with the rise of the noise is

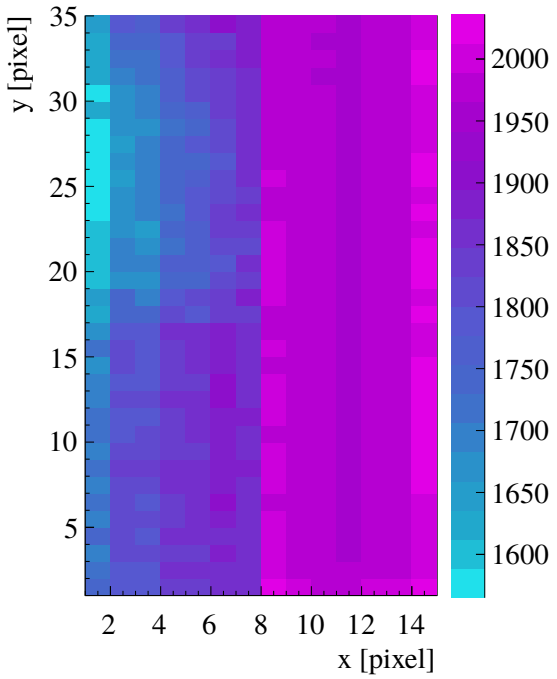

(A) baseline map for the FZ-n

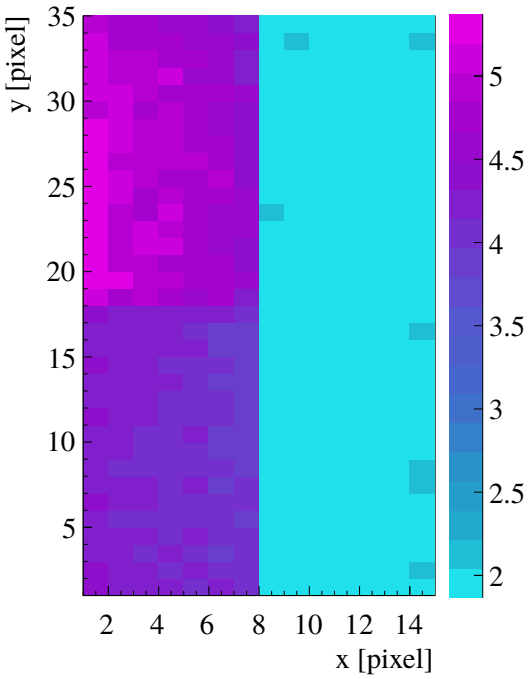

(B) noise map for the FZ-n

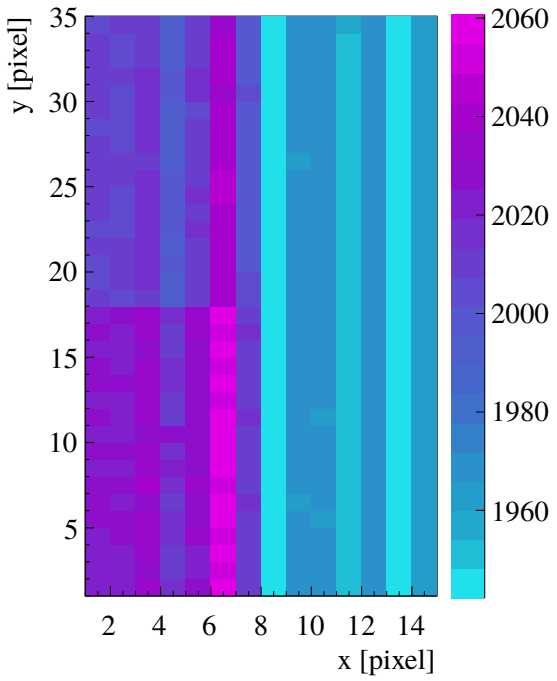

(C) baseline map for the DSOI-p

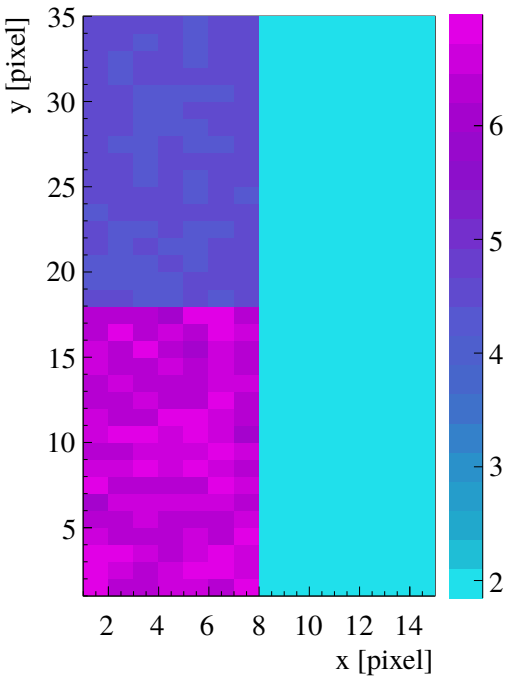

(D) noise map for the DSOI-p

FIGURE 5.2: Exemplary frame maps shown for the FZ-n wafer at 130 V back bias (top) and the DSOI-p at −70 V (bottom). The baseline and noise are given in ADU. The border pixels are not shown, because theirs levels differ significantly from mean value and showing them makes inner patterns not distinguishable.

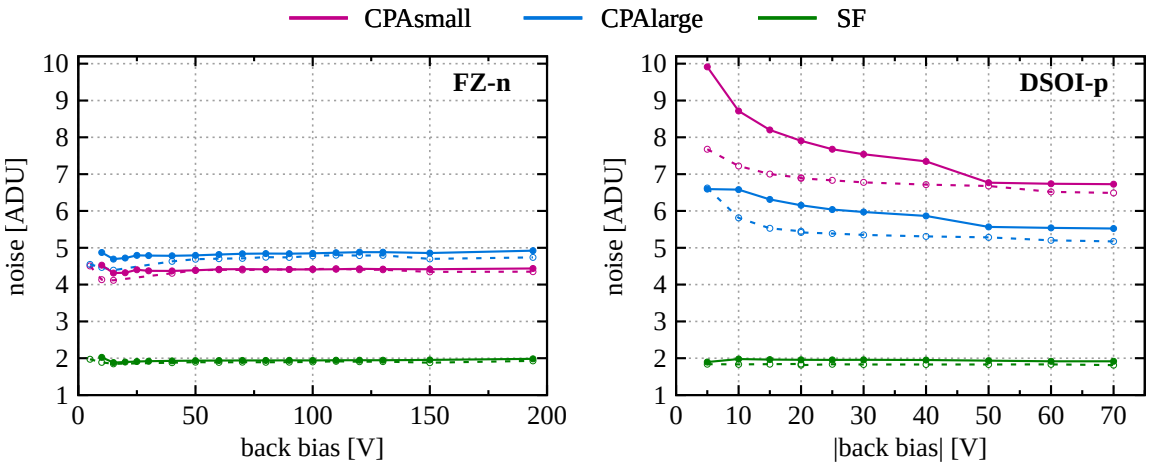

FIGURE 5.3: Mean noise versus back bias voltage for the FZ-n (left) and the DSOI-p (right). The solid line corresponds to readout clock frequency about 6 MHz and dashed 12.5 MHz. Uncertainty bars are not plotted for higher clarity.

observed from inside to outside pixels of the matrix. On the other hand this behaviour does not occur on the DSOI-p wafers what can be observed in figures 5.2C and 5.2D. For other matrices (SF, CPAsmall) both the baseline and noise maps are homogeneous over the entire detector. There are no hot or bad pixels observed for this assembly, buy if any appeared in other one, it was discarded from the analysis.

The mean noise versus back bias voltage is presented in Fig. 5.3. The noise was calculated for two different frequencies of readout clock. For about 6 MHz the relation is shown with solid line while for 12.5 MHz with dashed line. For faster clock the frame time is shorter and thus integration time, what might cause lower noise. In Tab. 5.1 the average noise values from plateau regions together with uncertainties are given.

For the FZ-n wafer the noise is constant in function of back bias voltage for all matrices. As expected, the best noise performance is observed for source follower matrix and it is about 2 ADU. The reason why the SF has much better performance is its simple pixel readout architecture, that does not introduce additional noise sources. The charge preamplifier pixels have the noise from 4 ADU to 5 ADU.

For the DSOI-p wafer the SF matrix show similar performance as for the FZ-n wafer. For CPA matrices the noise drops with increase of the back bias voltage and becomes flat over 50 V for 6 MHz readout clock reaching slightly above than 5 ADU for CPAlarge and 6.5 ADU for CPAsmall. The noise for 12.5 MHz readout clock is lower, especially for charge preamplifier matrices.

As it was mentioned before, in the 2016 prototype source follower matrix was not homogeneous and it contained pixels of slightly different layout and input transistor type. Since the gain of each submatrix was different, a significant distortion during clusterization procedure might have occurred. To alleviate this issue, a gain correction for each submatrix was applied. The gain measurements were not a part of this work, only the final values were

TABLE 5.1: Mean noise values ($\pm\sigma$) in ADU for different matrices, wafers and readout clock frequencies. Mean value is calculated from platau region from relation shown in Fig. 5.3.

	FZ-n		**DSOI-p**	
	6 MHz	12.5 MHz	6 MHz	12.5 MHz
CPAsmall	4.44 ± 0.63	4.35 ± 0.91	6.74 ± 0.50	6.56 ± 0.20
CPAlarge	4.92 ± 0.80	4.74 ± 0.99	5.54 ± 0.81	5.21 ± 1.12
SF	1.98 ± 0.05	1.93 ± 0.06	1.94 ± 0.04	1.83 ± 0.03

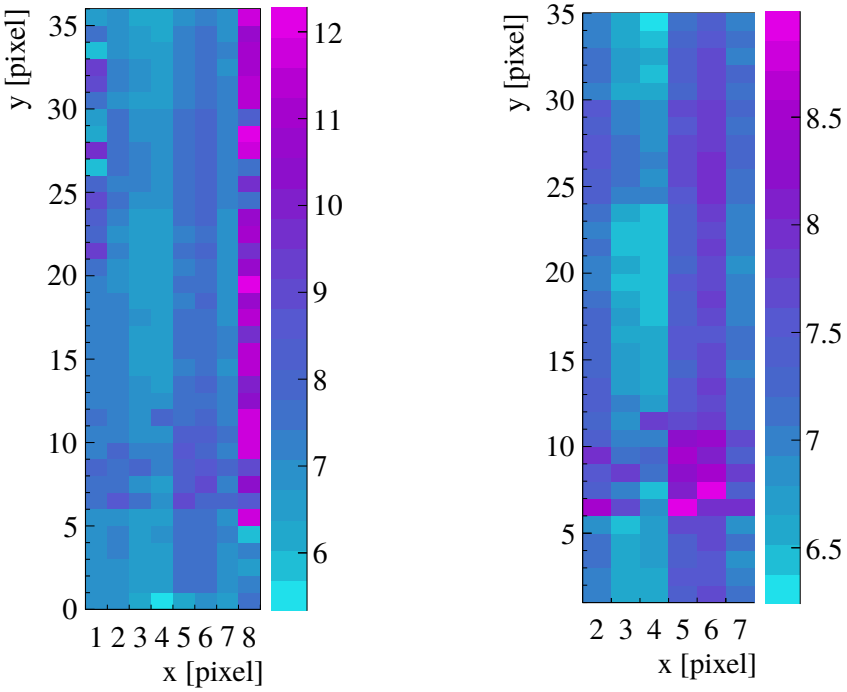

(A) entire matrix (B) without borders

FIGURE 5.4: Noise maps in ADU showing general performance of 2016 prototype for source follower on the FZ-n wafer. The noise values for 2016 and 2017 cannot be compared because of different configuration of amplifiers on the readout PCB.

used for data analysis. The gain calibration was done by measuring the response of each pixel to the 6 keV K_α peak of the Fe^{55} radioactive source.

The noise map for 2016 prototype is presented with and without borders columns and rows in Fig. 5.4 because then the inner-matrix pattern is clearly visible. In the horizontal direction a division between small sensing diode (right) and large sensing diode (left) designs is distinguishable. For the 2016 prototype the hit rejection for calibration dataset was not performed iteratively what may decrease slightly the accuracy of noise assessment in comparison to the 2017 year results, but the effect is below several percents. Since the noise was not recalculated on equivalent noise charge (ENC) and in 2016 and 2017 the configuration of amplifiers on readout PCB boards was different, the noise performance of these two prototypes cannot be compared directly.

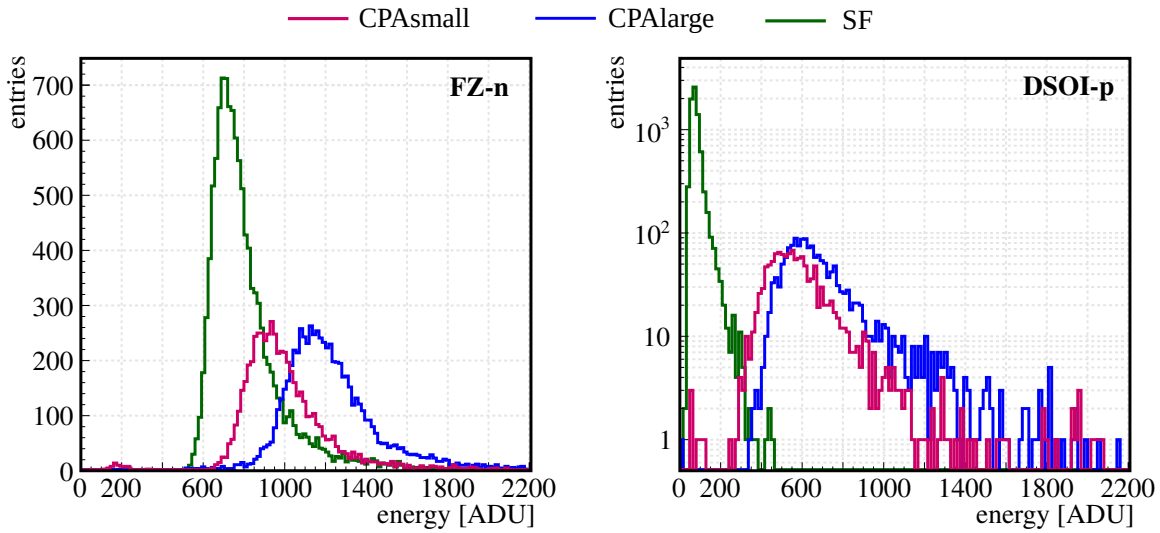

FIGURE 5.5: Energy spectra for the FZ-n at 130 V (left) and the DSOI-p at −70 V (right). The DSOI-p is shown in logaritmic scale for better clarity.

5.2 Signal analysis

The cluster energy is defined as a sum of energies of all pixels contributing to the cluster. Exemplary spectra for each matrix are shown in Fig. 5.5 for both wafer types at the highest back bias voltage. The presented spectra were generated using only the DUT correlated hits data collection and thanks to that random noisy entries were eliminated. The tails in a high energy region come mainly from events with delta electrons. A convolution of the Landau and Gaussian functions was fitted to each spectrum and then the Landau's MPV was taken as the signal value.

In Fig. 5.6 the signal versus square root of back bias voltage is shown. For the SF on the FZ-n wafer, signal is rising linearly with increasing depletion region and saturates when full depletion of the sensor is reached. The full depletion voltage for the FZ-n is thus around 70 V which is marked with orange line. After reaching the full depletion, charge preamplifiers signal is decreasing. This effect has to be investigated more, since it is not understood yet.

On the right plot in Fig. 5.6 the analogous relation for the DSOI-p wafer is presented. The maximal applied back bias voltage for this wafer type was −70 V. Because of unknown source leakage for the DSOI-p, a higher voltage had not been applied. Since the resistivity of the DSOI-p is much lower than for the FZ-n, the full depletion of the wafer was not achieved. The signal of the SF matrix is very small in comparison to the CPA pixels, because its amplitude depends inversely proportional on a detector capacitance as considered in Sec. 2.3 on page 28. The Mid-Si layer for the DSOI-p wafers causes that this capacitance is significantly larger than for single SOI wafers.

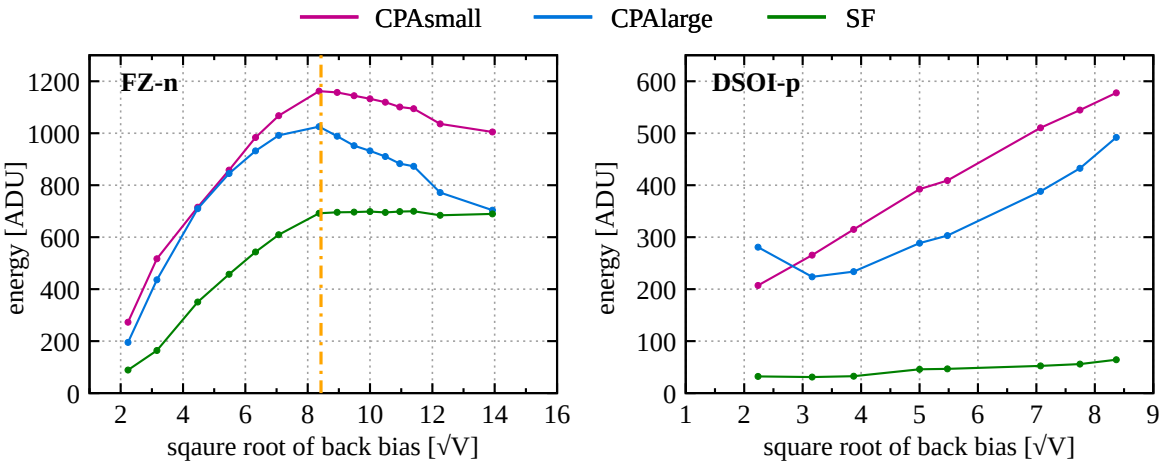

FIGURE 5.6: Signal versus square root of the back bias voltage on the FZ-n (left) and the DSOI-p (right).

5.2.1 Signal to noise ratio

Basing on the noise performance discussed previously the signal to noise ratio is calculated and presented in Fig. 5.7. The relations for SNR are similar as for the signal from Fig. 5.6 since the noise level is not changing significantly in function of the back bias voltage.

For the FZ-n wafer the best signal to noise performance of about 350 is shown for the source followers matrix. The SNR of charge preamplifiers with small sensing diode is about 250 after full depletion and for large sensing diode it is above 170.

Since the DSOI-p is not fully depleted, the SNR is much smaller. Charge preamplifier matrices achieve the SNR value close to 100. The source followers signal to noise ratio is very small in comparison to other cases and it is below 40 at -70 V back bias voltage.

In Fig. 5.8A the signal versus root square of back bias is presented for the first SOI detector prototype tested in 2016 year and in Fig. 5.8B the SNR is shown. The highest applied back bias voltage was 100 V. The maximal SNR is 140 which is almost 200 less than in newer prototype for this pixel type. The full depletion voltage is about 70 V, the same as for the 2017 FZ-n prototype.

5.2.2 Silicon resistivity

Knowing the full depletion voltage V_D one can estimate the wafer resistivity of thickness D basing on Eq. 2.19 on page 27:

$$\rho_d = \frac{D^2}{2\epsilon_s \mu_{e,h} V_D} \tag{5.1}$$

where $\mu_{e,h}$ denotes mobility of electrons or holes (majority carriers) and ϵ_s is absolute permittivity of silicon. The full depletion voltage for the FZ-n wafer of 500 µm thickness is estimated to be around $V_D = 70$ V. Thus, one can assess the resistivity of this wafer to about 12.3 kΩcm. As it was presented in Tab. 3.1 on page 35, the Lapis Semiconductor declares

the FZ-n wafer to be larger than 2.5 kΩcm. One has to notice, that the measured resistivity is around 5 times larger, that is a very significant difference.

5.2.3 Energy distribution within cluster

An interesting study regarding charge distribution is the energy division between pixels forming the cluster. In Fig. 5.9 information about the fraction of energy carried by pixels in a cluster is shown. The plot is made for 2TM-10-2 method, thus dataset is built of different cluster sizes. The pixel with the highest energy is labeled as "1", second highest as "2" and next pixels in analogous manner.

For both wafer types almost 95 % of the whole cluster energy is stored in four pixels. The distributions for the FZ-n and the DSOI-p differs. For the DSOI-p the charge is much more concentrated around seed pixel than for the FZ-n. This is expected since the DSOI-p is only partially depleted and has lower resistivity.

5.3 Cluster size analysis

Depending on clusterization method, the cluster size may be fixed or may vary as is the case for 2TM and 2HLM (see Sec. 4.3 on page 48). For these methods the cluster size is determined by threshold applied for neighbouring pixel discrimination.

The exemplary histograms of total, x and y cluster size distributions for the highest back bias voltage are presented in Fig. 5.10. The total cluster size corresponds to the number of all pixels building the cluster. The x and y cluster size corresponds to the largest dimension of the cluster in considered direction. For both wafer types the total cluster size is relatively large and a significant contribution comes from cluster built of $6-8$ pixels. For all considered cases except the SF on the DSOI-p there are no single-pixel clusters reconstructed. The slightly different histogram shape for x and y cluster size comes most probably from cross-talk effect that increase signal distribution in x direction.

In Fig. 5.11 the mean total, x and y cluster size dependences in function of the back bias voltage are plotted. Let us consider quantitatively the cluster size dependence on the back bias voltage. For the FZ-n wafer below full depletion the maximal total cluster size is around 15 for source followers and 13 for charge preamplifiers. For full depletion at 70 V it reaches $10-8$ pixels depending on the matrix type. For higher voltages it is slightly decreasing, because the electric field is rising. The mean x and y cluster size is not smaller than 2 for all back bias voltages, what benefits for spatial resolution performance. The differences between mean x and y cluster size comes most probably from two issues. Below the full depletion the cluster sizes are so large, that the physical size of the matrix in x direction is artificially limiting the mean cluster size value. Above full depletion the differences are caused mainly by cross-talk, as mentioned earlier.

For the DSOI-p wafer, that was not fully depleted, the mean cluster size is mostly constant in function of the back bias voltage and it is around 7 for charge preamplifiers and 4 for source followers. The mean x and y cluster size show similar trends.

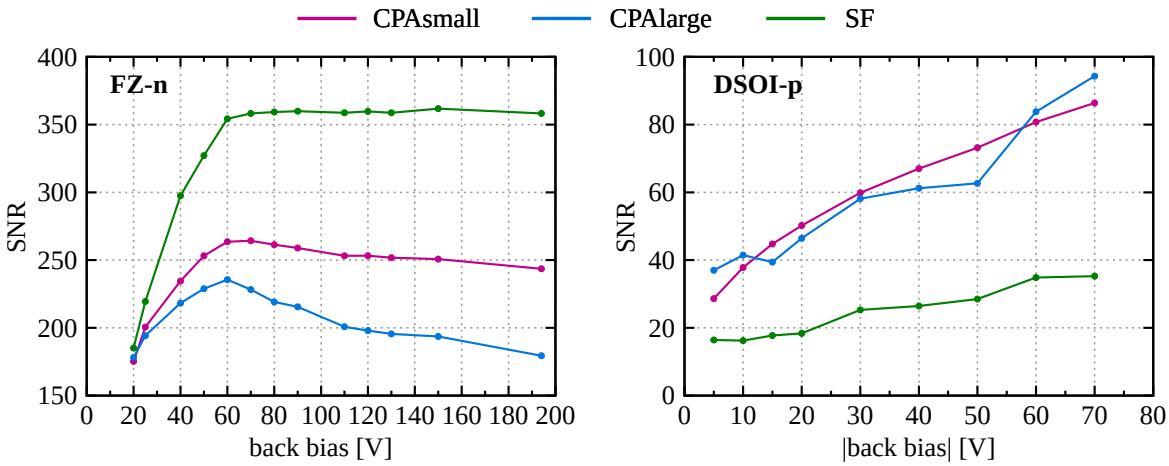

FIGURE 5.7: Signal to noise ratio in function of the back bias voltage at 12.5 MHz readout clock for the FZ-n (left) and the DSOI-p (right).

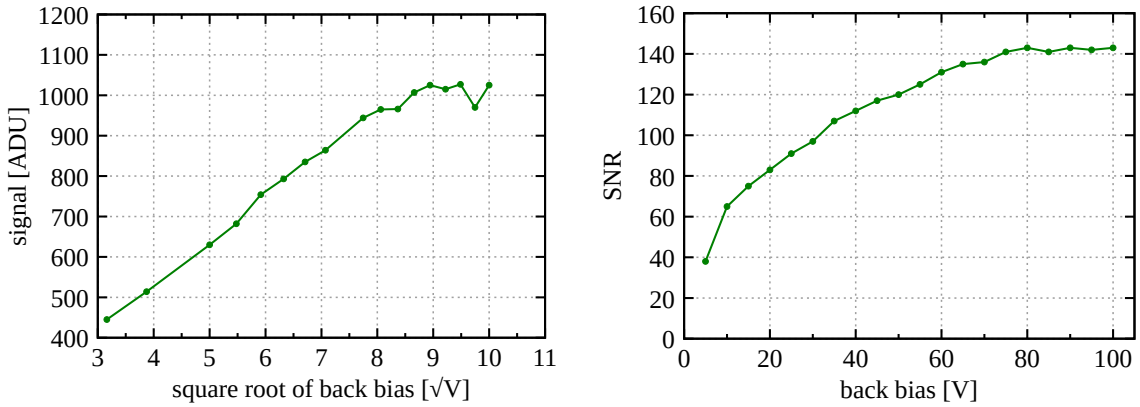

(A) Signal (B) SNR

FIGURE 5.8: Results for SF on the FZ-n from 2016 matrix.

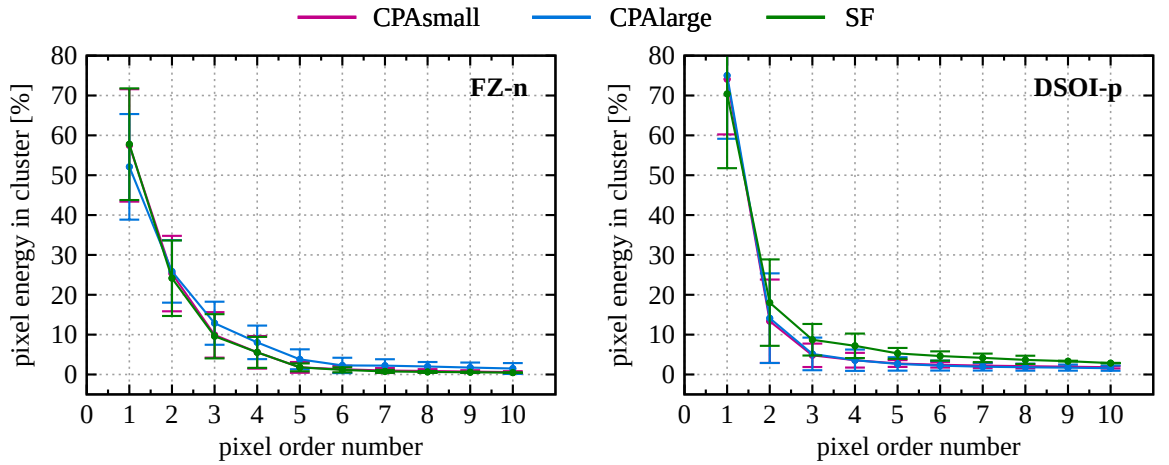

FIGURE 5.9: Distribution of pixel energy over cluster for the FZ-n (left) for 130 V and the DSOI-p (right) for −70 V. The 2TM-10-2 clusterization method was used.

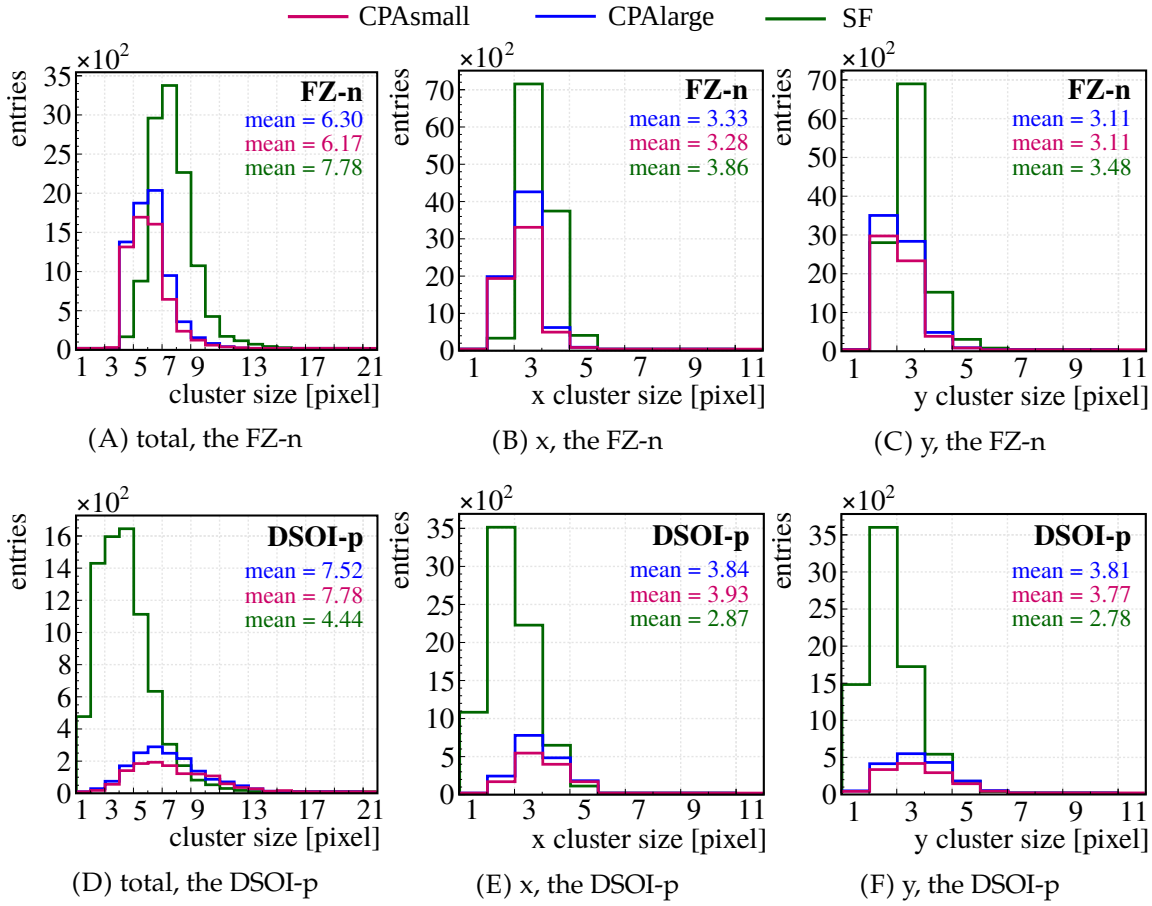

(A) total, the FZ-n (B) x, the FZ-n (C) y, the FZ-n

(D) total, the DSOI-p (E) x, the DSOI-p (F) y, the DSOI-p

FIGURE 5.10: Cluster size histograms made for 130 V back bias voltage for the FZ-n (top) and for −70 V for the DSOI-p (bottom). Clusterization method was 2TM-10-2.

Finally, let us consider the shape of the cluster size versus back bias relation. Intuitively, increasing the back bias voltage should cause increase of cluster size, since the depletion region grows. Because of that one could expect rise of the cluster size till full depletion of the detector. Further increase of the back bias voltage generates stronger electric field and thus drift time of the charges decreases. For over-depleted detector the cluster size may consequently slightly decrease.

However, the described behaviour is different for the measured FZ-n detector what is depicted in Fig. 5.11. The mean maximal cluster size is observed for about 20 – 30 V and then decreases with increasing the depletion region. This effect might be explained by the influence of charges induced in a non-depleted sensor region. A qualitative explanation is presented in Fig. 5.12 where sensor volumes at four different back bias voltages are shown.

On the left sketch half of the detector is depleted. When particle goes through the sensor, the charges are generated both in depleted and non-depleted regions. In non-depleted volume the charges mostly recombine and do not reach the depleted region. However, there is some region beneath the depleted volume from which the charges might diffuse into it and drift to electrodes. Those charges are symbolically marked with light violet in Fig. 5.12, while charges generated in the depleted region are in dark violet color. The cloud coming

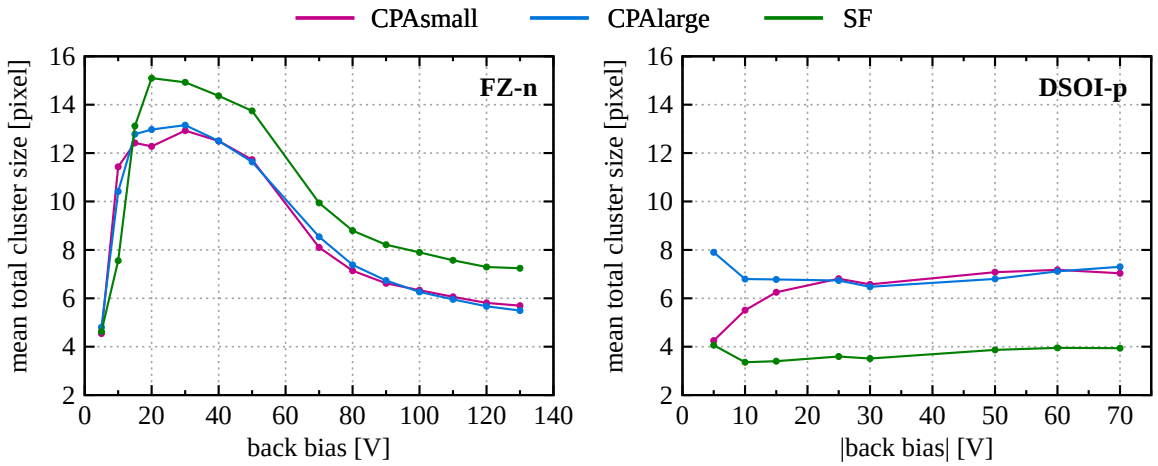

(A) Total cluster size

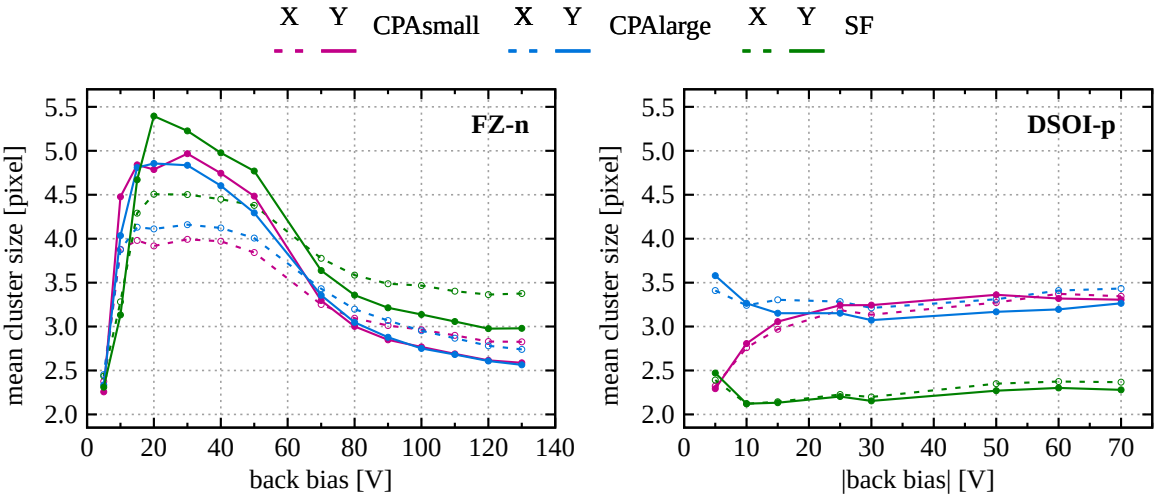

(B) x and y cluster size

FIGURE 5.11: Mean cluster size versus back bias voltage for the FZ-n (left) and the DSOI-p (right) for 2TM-10-2.

from non-depleted region may dominate the total cluster size. Going up with the back bias voltage, the width of the charge cloud coming from the non-depleted region is reduced as shown in middle sketches. Finally, for full depletion voltage (and above) this effect is completely eliminated and the diffusion cloud from the non-depleted region is not influencing the cluster size. Above full depletion the cluster size decreases, since the drift time is shorter and shorter.

A one more comment needs to be done for very low back bias voltages for the FZ-n wafer. Theoretically, the mean cluster size function should maintain a relatively large cluster size also for very low back bias voltages. Nevertheless, a sharp drop below 20 V is observed. Even for back bias voltages around 10 V the depletion volume is still relatively large, because it is estimated to be around 150 µm. As it is shown in further studies, the efficiency and spatial resolution for very low back bias voltages are reasonably good. Thus, it cannot be stated that for low back bias voltage the overall detector performance is distorted by some

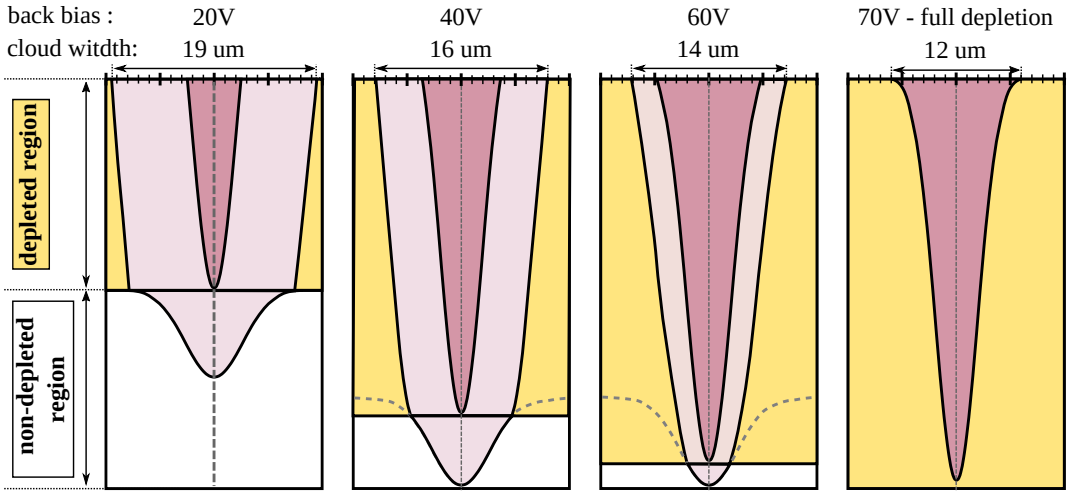

FIGURE 5.12: Ideological scheme presenting influence of the charge diffusion from non-depleted detector region. Light violet is the charge cloud comming from non-depleted region and dark violet from depleted region. Gaussian shape of the diffusion clouds is idealized. All number and scales are symbolic.

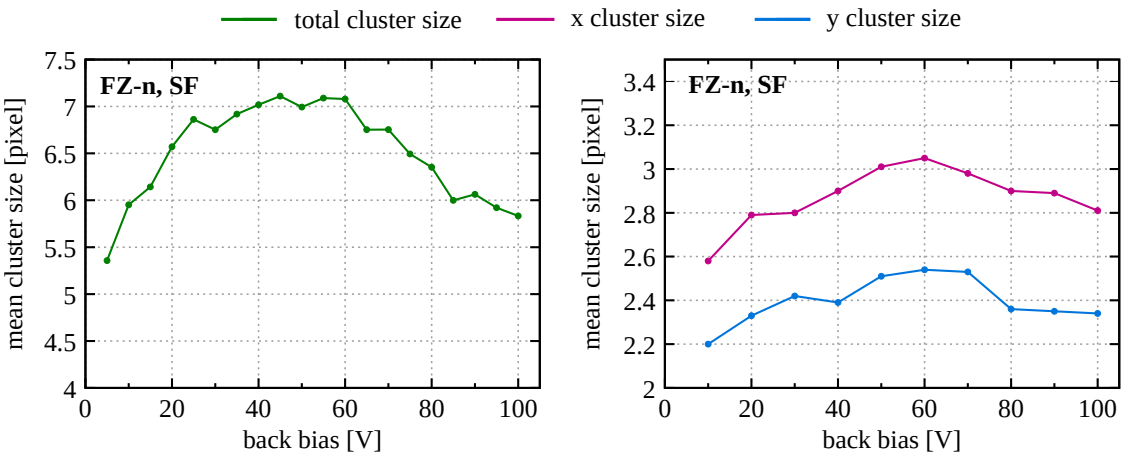

FIGURE 5.13: Mean total cluster size (left) and mean x and y cluster size (right) for SF matrix at 2016 prototype. The 2TM-30-3 method was used.

obvious reason. The behaviour of cluster size below 20 V has to be further studied and understood.

One has to notice, that the described effect depends on silicon wafer parameters since charge lifetime depends on wafer resistivity. The smaller silicon resistivity, the shorter lifetime and then the influence of charges from non-depleted region should be less significant. This might be an explanation why the cluster size relation in function of the back bias voltage is different for the FZ-n wafer and the DSOI-p wafer. The silicon resistivity of the DSOI-p is much smaller than the FZ-n. For the DSOI-p the cluster size is increasing with rise of the back bias voltage. Thus, this may indicate that diffusion cloud from non-depleted region is not influencing the cluster size. Nevertheless, to be fully conclusive, the DSOI-p wafer needs to be fully depleted and then measured.

In Fig. 5.13 the total cluster size (left) and in x and in y (right) are presented for the 2016 beam-tests. The clusterization method for this prototype was 2TM-30-3. Since the cluster

size mainly depends on the condition for neighbour pixel, the comparison between cluster size for 2016 and 2017 is not straightforward. In addition, the reset affected-clusters are not removed from the data sample, what is decreasing the mean cluster size. Despite this, the similar trend of the cluster size curve as in 2017 data is observed and the discussion may be analogous. The mean cluster size is in the range from 5 to 7 depending on depletion region depth. The mean cluster sizes in x and in y differ slightly, but not more than 15 %. This difference may also be caused by the cross-talk, since the pixel readout layout in 2016 and 2017 was similar.

5.4 Detector efficiency

The detector efficiency is one of the major detector performance parameters. In this work, the efficiency of a detector is defined as a ratio of the number of DUT correlated hits to all telescope tracks passed through its volume.

$$\text{efficiency} = \frac{\text{number of DUT correlated hits}}{\text{number of all tracks}} = \frac{\text{number of correlated tracks}}{\text{number of all tracks}} \quad (5.2)$$

As it is shown in Eq. 5.2, one can use the number of correlated tracks in the numerator, since it is equal to the number of correlated DUT hits. All constraints imposed during the correlation phase may influence on the DUT hits data collection and artificially decrease (or increase) efficiency value. The correlation procedure was already described in Sec. 4.6 on page 58, but just to remind a track is paired with a DUT hit when two conditions are met:

- track ToA and DUT hit row time-stamp difference is not larger than one frame time,
- track-hit residuum value in x and in y is not larger than two pixel pitches (60 µm).

In addition, the border-clusters containing any pixel from the edge of the matrix or being on submatrices intersection, are discarded from spatial resolution studies. This is done in order not to bias the results by the clusters that might have charge partially lost. The most reliable approach is to use the same correlation algorithm for the spatial resolution and the efficiency calculations. However, since for the efficiency the only required information is whether the DUT recorded a hit when the telescope did, the border-clusters are kept in the analysis. This allows to increase the statistics what is always important for the tested SOI detector because it is very small especially in x direction (8 pixels). The used clusterization method was 4PM-10 in order to keep relatively small cluster and thus decrease the probability of a pile-up. It should be noticed, that also 2TM-10-8 clusterization method was used for the efficiency calculation to verify whether clusterization algorithm might influence on the results. The final outcomes for these two clusterization approaches were almost the same and the differences were negligible.

The second condition mentioned above regarding the residuum constrain may exclude these DUT hits, that have for some reason poor spatial resolution. This might be the case when delta electrons occurred. Since space correlation demand cannot be removed completely to avoid random correlations, it is slightly modified for efficiency studies. If the DUT hit did not pass the 60 µm residuum constrain, the algorithm checked whether the

seed position of this cluster was passing it. If so, cluster was kept in the analysis. This allowed to solve the problem of hits with delta electrons or at least some part of them, that had a bad spatial resolution, but a seed of the hit was still near the true track. This modification increased the efficiency of about 1 %.

The efficiency is not calculated directly as the ratio of individual numbers as given in Eq. 5.2. The more conclusive results come from the efficiency maps, presenting the efficiency for particular detector areas. It allows to verify if there are some non-efficient regions in the matrix. Then the average value from efficiency map is calculated as a final detector efficiency value. To create efficiency map, the two following maps have to be generated:

1. Correlated tracks positions. The exemplary map is presented in Fig. 5.14B for 130 V back bias voltage for the FZ-n wafer.
2. All tracks positions from the region of the DUT detector enlarged by 150 µm from each side (5 pixel pitches). Example is also shown in Fig. 5.14A.

In practice, these maps present the number of tracks passing through the detector area. Thus, the ratio of mentioned tracks position maps creates the efficiency map, that is presented in Fig. 5.15 for both wafers at maximum available back bias voltage. The efficiency maps are homogeneous, thus there are no non-efficient pixels, rows or columns in the tested detectors. A drop of efficiency is observed at the matrix borders, which is caused by the clusters lost outside the detector. The average efficiency value was calculated without the non-efficient borders.

An incomprehensible effect occurs in the CPAlarge. In Fig. 5.16 the energy spectra are presented from all the DUT hits data sample and for correlated hits data sample. The observation is that the low-energy peak occurs on all spectra for the FZ-n. Although it is very small after correlation with tracks, it is still present and its source is unknown. It has to be noticed, that the correlated data sample was created in the same manner as for the spatial resolution considerations, so without cluster touching border pixels and without reset-affected clusters. Thus, the low-energy clusters coming from known sources are not present in the data sample. Also the noisy entries are not an explanation, since this peak also occurs after correlation with tracks, so they pass time and space conditions for matching with the track. It was verified, that the hits from low-energy peak are uniformly distributed among the matrix and are not characterized by poor spatial resolution or any other distinctive feature. Such an effect is not a case for other matrices (SF, CPAsmall). The DSOI-p also presented in Fig. 5.16 has smaller statistics than the FZ-n so it is hard to judge whether the described effect is less significant for the DSOI-p or it is a matter of number of entries. All these considerations lead to conclusion that these low-energy entries are increasing the CPAlarge efficiency value in comparison to other matrices. Since the source of the peak is unknown, one cannot assume that the results for CPAlarge are not biased somehow. Thus, some of the detailed efficiency analyses are shown only for the two other matrices.

In Fig. 5.17 the in-pixel efficiency for all matrices and for both wafer types are shown. The in-pixel efficiency is reasonable homogeneous among the pixel pitch and no specific patterns are observed. The effect is the same for the FZ-n and DSOI-p wafer and for all matrices, as well.

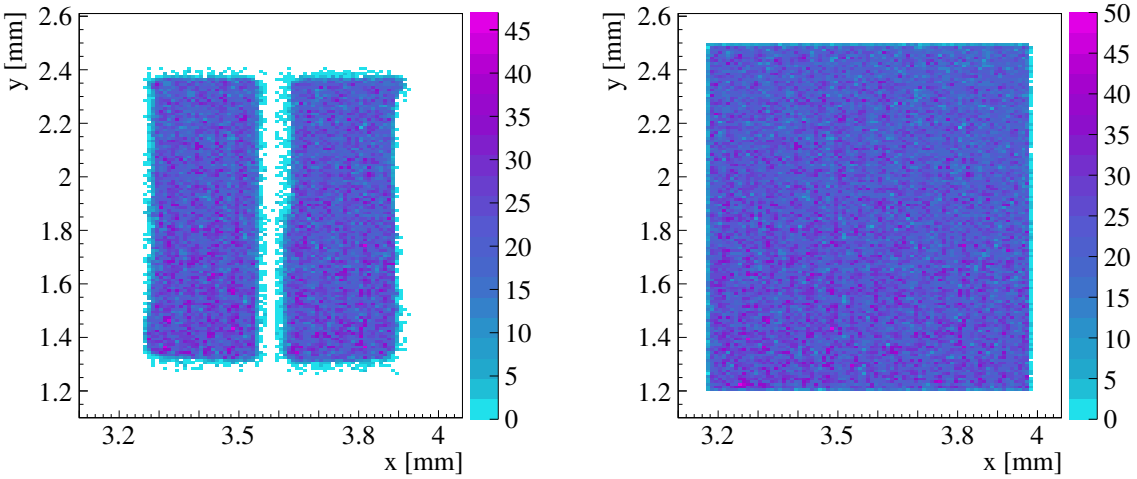

(A) correlated tracks (B) all tracks

FIGURE 5.14: Track position maps at 130 V for the FZ-n wafer. They present practically the number of recorded tracks in fuction of position.

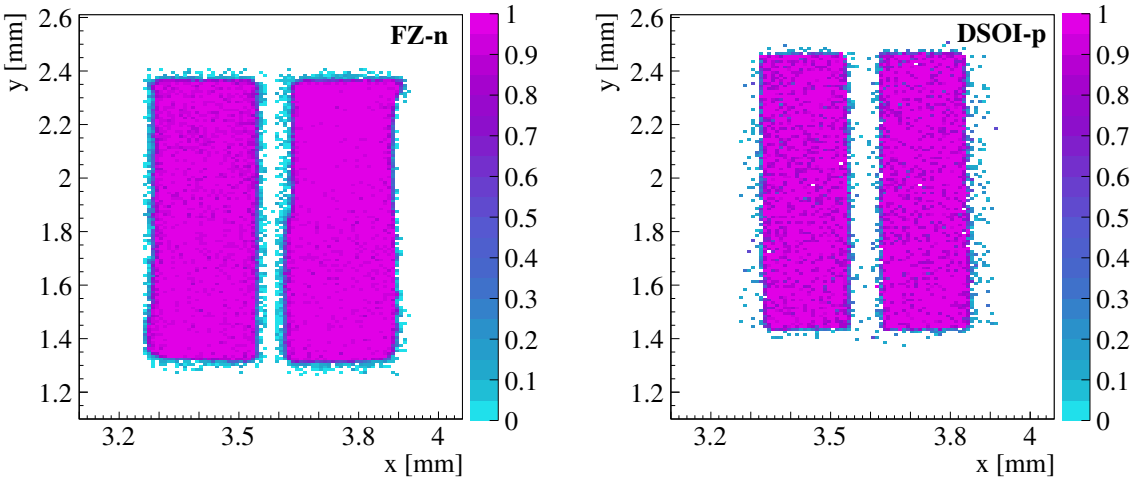

FIGURE 5.15: Efficiency maps. The FZ-n is presented for 130 V (left) and the DSOI-p for −70 V (right). Single bin size is 10 µm (one third of pixel pitch).

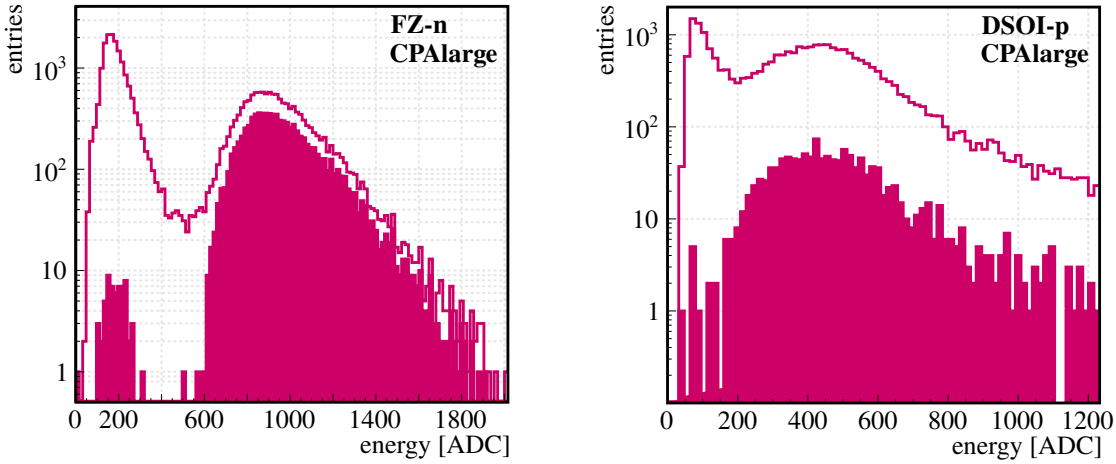

FIGURE 5.16: Energy spectrum for CPAlarge for all data (line) and for correlated hits without border-clusters (area) for the FZ-n at 130 V (left) and the DSOI-p at −70 V (right).

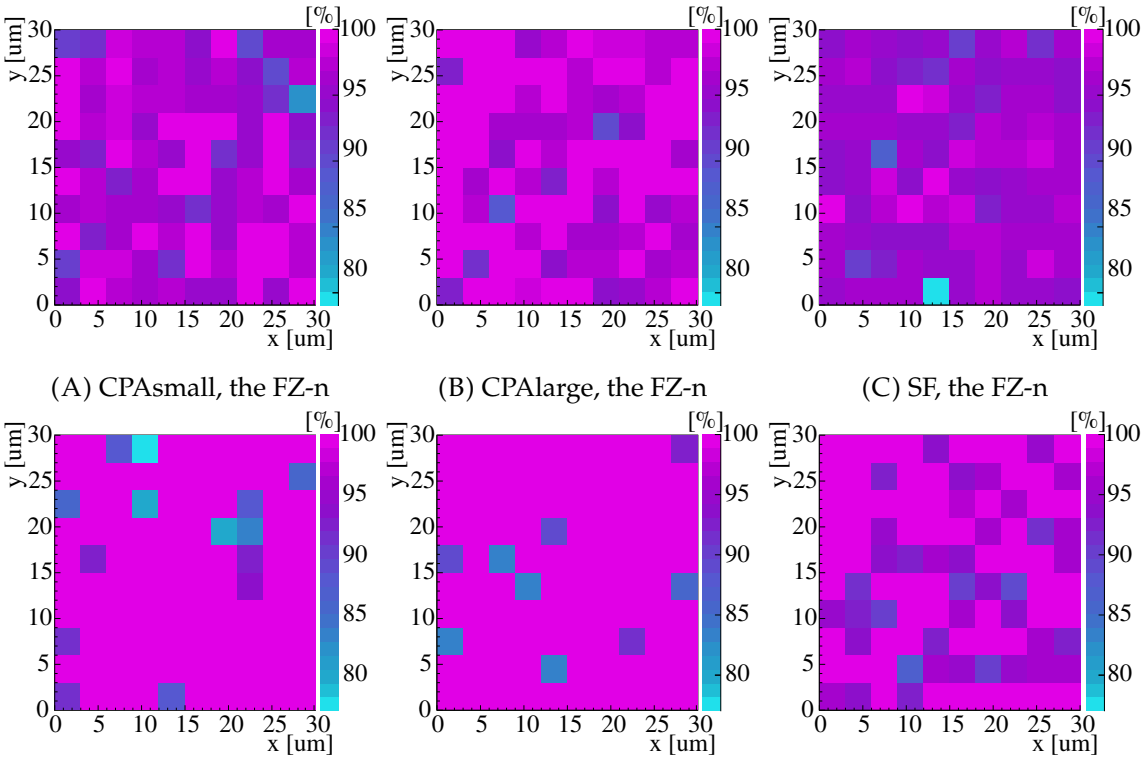

(A) CPAsmall, the FZ-n (B) CPAlarge, the FZ-n (C) SF, the FZ-n

(D) CPAsmall, the DSOI-p (E) CPAlarge, the DSOI-p (F) SF, the DSOI-p

FIGURE 5.17: In-pixel efficiency for the FZ-n at 130 V (top) and for the DSOI-p at −70 V (bottom).

5.4.1 Depletion depth influance

The efficiency versus the back bias voltage was calculated for different readout clock frequencies and for two various wafers of each type (two FZ-n and two DSOI-p). Theoretically, a faster readout clock may provide better efficiency performance since the probability of hits pile-up is smaller. This consideration is supported by the fact that measured average hit rate per frame is 1.66 for 6 MHz and 1.26 for 12.5 MHz readout clock. Basing on the analysis of hit rate per frame one can assess the pile-up probability for around 2.5 % to 3 % for slower and 1 % to 2 % for faster readout clock. The beam intensity for particular datasets might also affect pile-up probability and therefore influence on efficiency.

In Fig. 5.18 the average efficiency versus back bias voltage for all tested cases is presented. There are significant fluctuations up to 2 % between particular measurements and relatively strong interlacing of the curves is observed. For the FZ-n wafer the efficiency drops for very low back bias voltages when depletion region is below 150 µm (around 10 V back bias voltage), but still the efficiency is not less than 90 %. Above 10 V the efficiency is around 98 % but taking into account fluctuations from point to point, one can reasonably conclude that the efficiency is not less than 96 %. For the FZ-n wafer, the faster readout clock seems to have slightly better efficiency, what may be explained by the mentioned pile-up effect. However, there is a need to confirm this conclusion on more data, because only one dataset for 12.5 MHz have been already analysed.

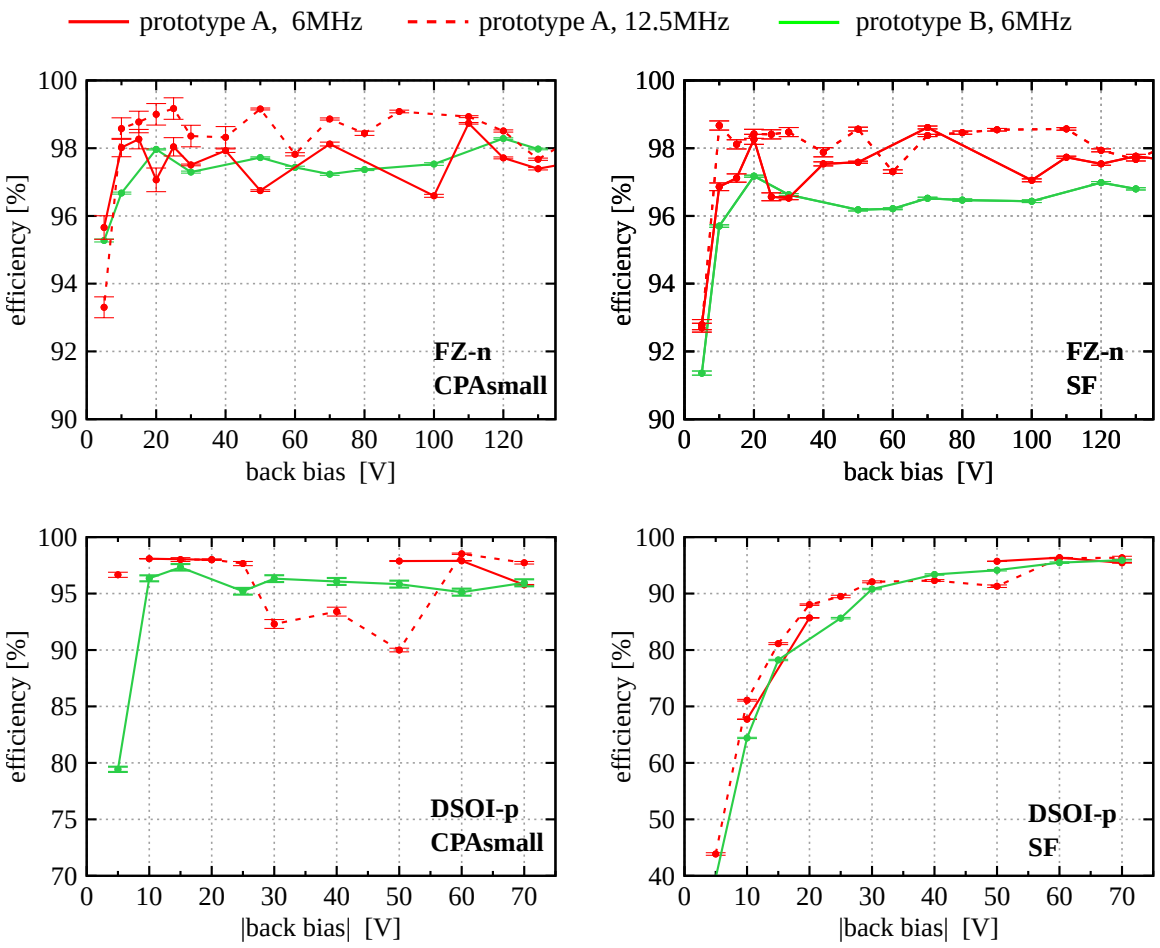

FIGURE 5.18: Average efficiency in function of the back bias voltage for the CPAsmall (left) and SF (right) for the FZ-n (top) and the DSOI-p (bottom). Results for two different readout clock frequencies and various prototypes are shown.

The results from the DSOI-p wafer are not so conclusive as from the FZ-n, since it is not fully depleted. The efficiency is rising with increase of the back bias voltage, because the depletion region is increasing. The signal on source followers is very small at low back bias voltages, thus the efficiency for this matrix type is even below 70 % for 10 V. However even for partially depletion, the DSOI-p efficiency is estimated to be not worse than 94 % for CPAsmall matrix, which is dedicated for this wafer type.

To sum up, there are two major effects suspected to be a source of non-efficiency. The first is pile-up effect, mentioned above. Also the detector dead time (reset phase) might cause that lost of particular DUT hits. As it was explained in Sec. 4.7.1 on page 68, the reset influence is not taken into account in the efficiency analysis. Both of these effects influence might be investigated in the data analysis, what has to be done in the future. Nevertheless, both pile-up and dead time should cause a constant drop of the efficiency. What is observed for the tested detectors, there are significant fluctuations between particular datasets measurements. Thus, one can suspect that there is some unknown inefficiency source that influences on final results.

5.5 Spatial resolution

The final DUT resolution σ_{res} can be calculated according to Eq. 2.32 on page 32. In the following section the σ_{DUT} means always a measured DUT resolution taken as a standard deviation from the residuum distribution. The residuum is a difference between the DUT hit position and its correlated track position. The σ_{res} is a final resolution, after telescope resolution σ_t subtraction. The telescope resolution at DUT plane was estimated to be on the level of 2 µm.

Since the DSOI-p wafer suffers from unknown source leakage currents and beause of that it was only partially depleted, the results for this wafer type are not fully conclusive. The detailed analyses of spatial resolution were performed for the DSOI-p in the same range as for the FZ-n wafer, but here in this section they are not always shown for greater clarity. For such cases the results are attached in appendixes. Despite the fact that presently the DSOI-p production process has to be improved by the manufacturer, one has to remember that the DSOI-p is more promising in case of radiation hardness than single SOI wafer. Thus, this wafer type studies are especially worth to perform, but it has to be done in details after process improvement.

As it is shown further in this work, the proposed mp-η correction algorithm introduced in Sec. 4.5.1 on page 55, improves the spatial resolution significantly. Thus, all the presented results are shown after this correction, otherwise it is indicated in the text.

Exemplary residua distributions for all matrices are presented in Fig. 5.19. For the FZ-n wafer the statistics of the datasets was significantly higher than for the DSOI-p and also the overall resolution of this wafer is much better. For the FZ-n there is a sharp peak centered around zero but also the non-Gaussian tails are clearly visible. The tails of residua distributions are comprising 10 % of the whole statistics. For the DSOI-p wafer the overall worse spatial resolution performance most probably covers residua tails. There are two obvious candidates for tail entries: pile-up hits and hits affected by the delta electrons. When two hits are merged together into one cluster as it is when the pile-up occurs, the calculated cluster position can be significantly distorted. As it was considered for efficiency studies, the pile-up probability is in the range from 1 % to 3 % of the whole statistics, depending on readout clock frequency.

To estimate how many events with delta electrons are in the tails, one has to determine the condition for such events selection. Assuming that they should have large cluster size, let us define the cluster length as:

$$L_{\text{cluster}} = \sqrt{l_x^2 + l_y^2} \tag{5.3}$$

where l_x is x cluster size and l_y is y cluster size. The cut for L_{cluster} is not obvious since delta electrons might generate in principle arbitrary cluster sizes. Hence, to have a reference point, let us consider exemplary dataset for SF matrix on FZ-n wafer. For the whole data sample the mean cluster size length is 4.5 ± 0.9. Thus, the clusters of L_{cluster} larger than 6.5 (exceeding 2σ criteria) are classified as delta electron entries. This condition is fulfilled by about 20 % of the residua tail entries and almost all of these entries (90 %) have a large energy (belong

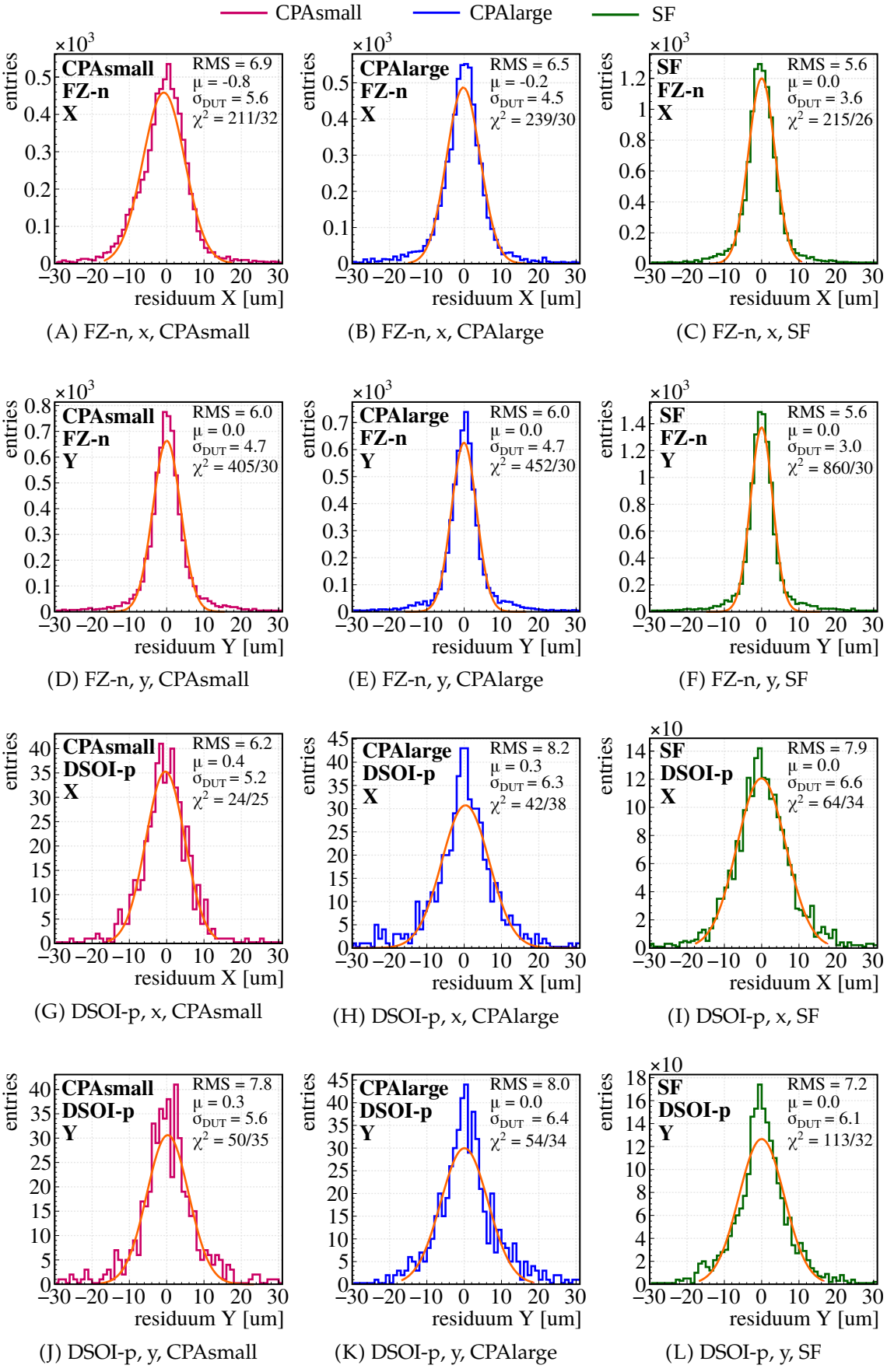

(A) FZ-n, x, CPAsmall (B) FZ-n, x, CPAlarge (C) FZ-n, x, SF

(D) FZ-n, y, CPAsmall (E) FZ-n, y, CPAlarge (F) FZ-n, y, SF

(G) DSOI-p, x, CPAsmall (H) DSOI-p, x, CPAlarge (I) DSOI-p, x, SF

(J) DSOI-p, y, CPAsmall (K) DSOI-p, y, CPAlarge (L) DSOI-p, y, SF

FIGURE 5.19: Residua distributions for the FZ-n at 130 V (top two rows) and DSOI-p at 70 V (bottom two rows) for 2TM-10-2. Fits are made for 95.5 % of the whole statistics. RMS corresponds to standard deviation of the distribution.

to tails of the Landau distribution). Large energy is also suspected to be characteristic for entries with delta electrons. Such consideration allows to roughly estimate, that only about 20 % of tail entries are hits with delta electrons (thus 2 % of whole data sample). The source of the remaining part of tail entries is unknown. All the tail entires are uniformly distributed via the matrix area. Also theirs cluster shape and energy distribution behave similar to the whole sample. There is no special feature that differs the remaining tail entries from normal good-resolution events.

The tails of the residua may also come from tracks quality and not from the DUT detector performance. The basic check of the track reconstruction goodness is expressed by χ^2 value. The distribution of tails tracks χ^2 is the same as for the whole track data sample. Still, in order to exclude the telescope influence on residua tails one has to perform the detailed analysis of telescope plane resolution (especially residuum shape). This analysis is not finished yet, but it is ongoing.

One can also notice, that telescope resolution is very close to the DUT resolution on the FZ-n wafer, where tails occurred. It might happen, that this issue is generating the residuum tails. The detailed analyses examining this effect also have to be done. Nevertheless, on this stage of the analysis, one cannot judge if the tail entries, that significantly contribute to residuum distributions, are coming from the DUT performance or from the telescope.

As it was considered in Sec. 2.4.2 on page 31, the basic approach for the measured DUT resolution σ_{DUT} estimation is a standard deviation of residuum distribution. For an ideal case, the standard deviation of a distribution should cover with the standard deviation of Gaussian fit to this distribution. Unfortunately, since the tails are present, they influence a lot the standard deviation values and are not reliable estimation of DUT resolution. Thus, the standard deviation values are given on residuum plots in Fig. 5.19 to give a general overview, but for the σ_{DUT} calculation the Gaussian fit parameters are used.

To extract the DUT resolution σ_{DUT}, Gaussian function is fitted to the 95.5 % of the residua distribution. It means, that under the fit curve, that is centered at maximal value bin, there is roughly 95.5 % of all residuum distribution statistics. The σ_{DUT} is a standard deviation of the Gaussian fit. Fitting to the 95.5 % is used in many high energy physics experiments. Such a criteria usually allows to cutoff delta electrons and also some unphysical random events that contribute to the residua distributions. In spite of that, the different shape of residua distributions causes that fitting Gaussian to 95.5 % is not always the solution for cutting the tails.

Assuming, that the tails are not coming from the detector performance one can consider how would be the spatial resolution without tails influence. In Fig. 5.20 the exemplary residua distributions are shown presenting the alternative fitting method. The SF on the FZ-n and CPAsmall on the DSOI-p were chosen since these matrices show the best performance on the particular wafers. Instead of single Gaussian the sum of two Gaussian is fitted, one covering the tails and the second covering the centre residuum peak.

Such a fitting method allows to assess what would be the σ_{DUT} when not taking into account tail entries. For the FZ-n, the $\sigma_{\mathrm{i-DUT}}$ of the inner Gaussian is almost 0.5 µm lower than for single curve fit. It means that after subtracting the telescope resolution the final

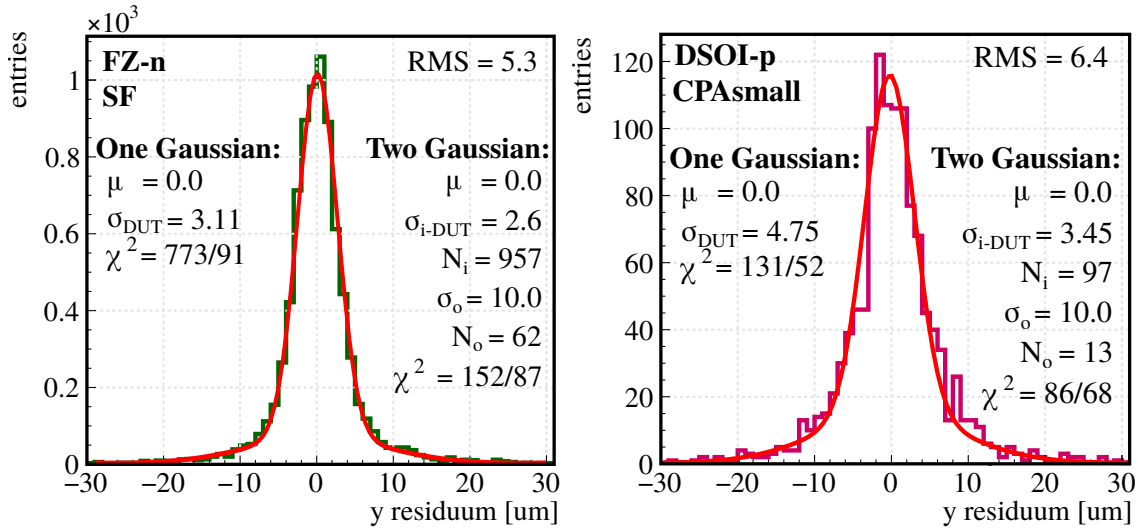

FIGURE 5.20: Example of the sum of Gaussian fit for SF on the FZ-n (left) and CPAsmall on the DSOI-p (right). Index *i* corresponds to inner (centre) Gaussian and *o* to the Gaussian that covers tails. Single Gaussian fit is not shown, but its parameters are plotted on the left side of the distribution. RMS corresponds to standard deviation of the distribution.

resolutuon σ_{res} would be 1.67 µm, whereas for the single Gaussian fit it was 2.38 µm. The difference in resolution is thus about 0.7 µm what gives the improvement of about 30 %. When considering such low resolutions, this upgrade is a very significant benefit especially when taking into account that the pixel size is 30 µm. Nevertheless, since the source of the tail entires is still unknown, making too far conclusions is not yet justified. Thus, the fitting method of the single Gaussian to 95.5 % of the statistics is a default method used further in this work.

At the beginning of the spatial resolution studies the summary results from 2016 prototype are shown since this detector was treated as a test ASIC. Thus, it is a good introduction before a detailed analysis performed for 2017 prototype, presented further in this chapter.

In 2016 to extract the spatial resolution the Gaussian fit was made to the whole residuum distribution as shown in exemplary Fig. 5.21. The used clusterization method was 2TM-30-10. The reset-affected clusters were not discarded from the analysis. The spatial resolution versus back bias voltage is presented in Fig. 5.22. The results are also shown before and after mp-η correction.

The mp-η correction does not improve the results for 2016 prototype. This is probably caused by the charge distribution distorted by the non-homogeneous pixel matrix, since the small 8×36 SF pixel matrix was built of nine pixel types. Probably despite the gain correction, the signal distribution was still significantly affected and the mp-η correction is then not improving the results. The detector performance is similar for x and y direction and in the best case it shows 4.5 µm of spatial resolution after subtracting telescope resolution.

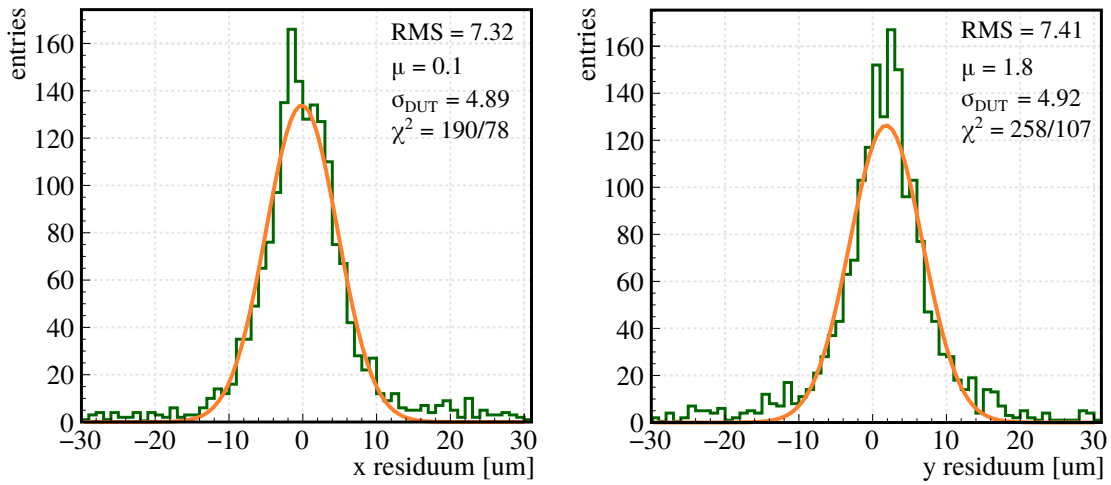

FIGURE 5.21: Exemplary residua distributions in x and y direction for 100 V of back bias voltage for SF matrix on 2016 prototype. Fit is made for the whole distribution. RMS corresponds to standard deviation of the distribution.

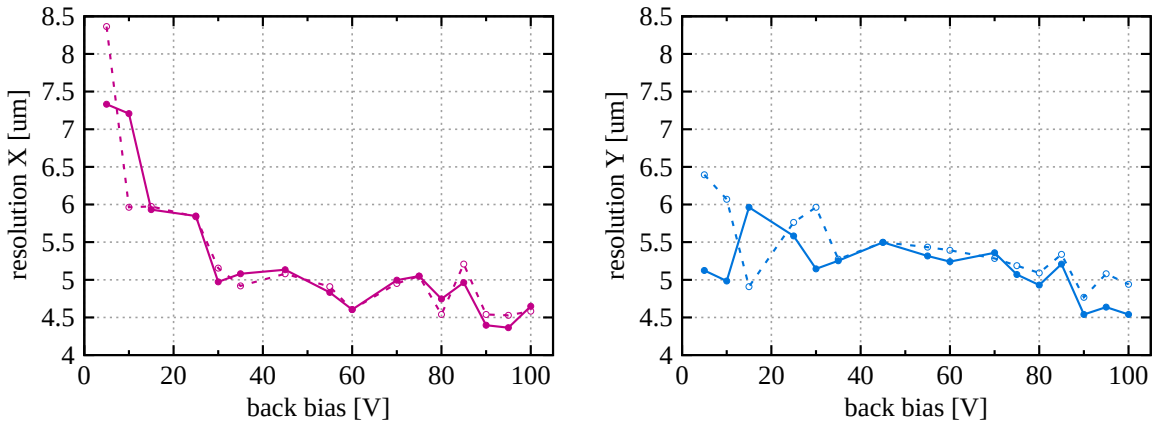

FIGURE 5.22: Final spatial resolution σ_{res} in x and in y at 100 V back bias voltage with COG position calculation (dashed) and after mp-η correction (solid) for SF matrix on 2016 prototype.

5.5.1 Seed and neighbour threshold dependence

The standard approach during the clusterization procedure is the 2TM method. Considerations in Sec. 5.2.3 show that the seed threshold is of a minor importance, because the seed threshold pixel signal is high enough to set relatively high th_{seed} without losing efficiency. Thus, it also should not affect the spatial resolution which is confirmed by the scan of the resolution versus seed threshold shown as the example in Fig. 5.23A for the FZ-n wafer. The resolution is completely independent from the seed threshold in the range 5 – 30 as expected.

A major importance during clusterization comes from the neighbour threshold, since it determines how many pixels are used in a position calculation. The behaviour of the resolution versus neighbour threshold is also shown in Fig. 5.23B. Increasing cluster size leads to visible spatial resolution improvement in 2TM method mainly for y direction. Thus, the minimum reasonable $th_{neigh} = 2$ was chosen for further analyses.

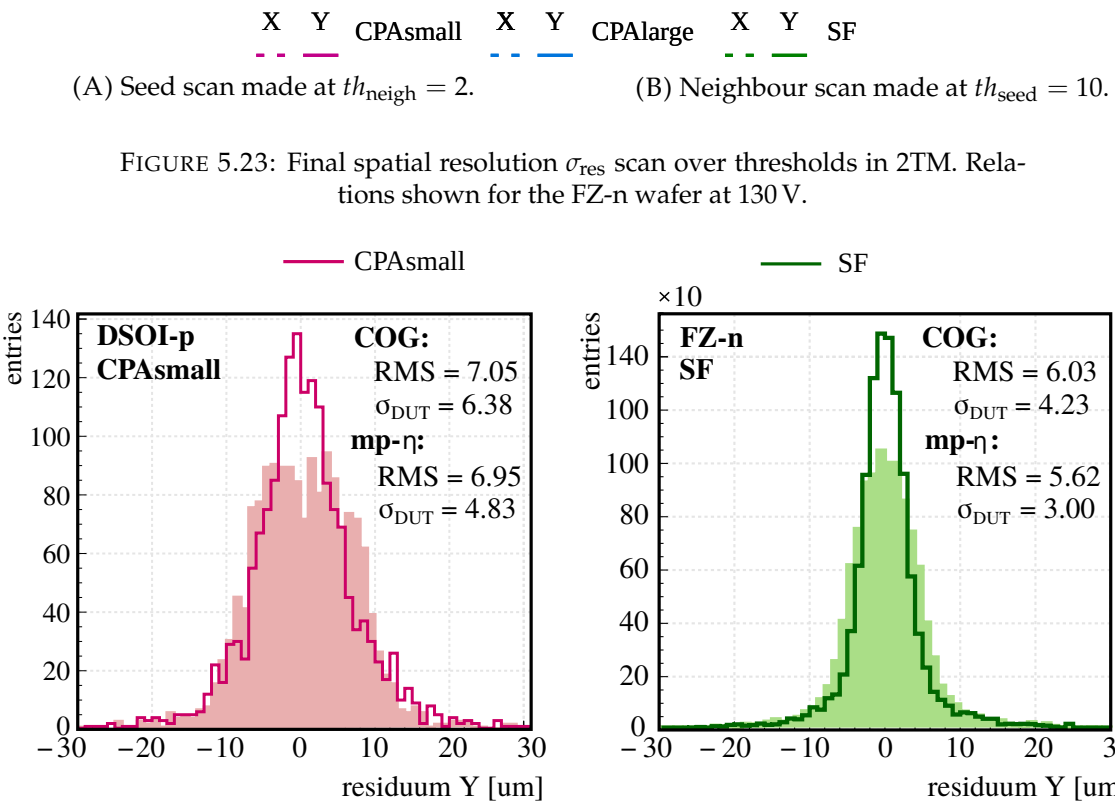

(A) Seed scan made at $th_{\text{neigh}} = 2$. (B) Neighbour scan made at $th_{\text{seed}} = 10$.

FIGURE 5.23: Final spatial resolution σ_{res} scan over thresholds in 2TM. Relations shown for the FZ-n wafer at 130 V.

FIGURE 5.24: Residua distributions for y direction with COG positions (area) and after mp-η correction (solid line). The examples shown for the DSOI-p (left) and the FZ-n (right). The 2TM-10-2 clusteriazaton was used. The Gaussian fits are not drawn for better clarity. RMS corresponds to standard deviation of the distributions.

5.5.2 Multi-pixel η-correction

The proposed method of mp-η correction was already widely described in Sec. 4.5 on page 53. In Fig. 5.24 the example residua distributions generated using COG positions and after mp-η correction are presented for different cases. The mp-η correction makes the distribution visibly sharper also with smaller standard deviation. The σ_{DUT} value of the fit (not shown for clarity) is even about 25 % – 40 % smaller for the presented examples.

In this work different cluster formation methods are studied. Each clusterization method reconstructs cluster in the different way. Thus, let us consider the influence of the proposed mp-η correction for different clusterization algorithms. Although the mp-η procedure is leading to making uniform the in-pixel hit position distribution for single dimension, one can study also the 2-dimensional in-pixel hit position. The exemplary maps are shown in Fig. 5.25 using COG hit position and mp-η corrected positions.

The only methods that allow hit position reconstruction along the whole pixel pitch using COG algorithm are the 2TM (Fig. 5.25A) and 9PM (Fig. 5.25H). The first one is not forcing the cluster size and it allows the cluster to be as large as possible if only pixel SNR is above th_{neigh}. The 9PM is a fixed-size clustering method and it takes always 9 pixels which is usually enough to cover almost all generated particle charge. The 4PM is forcing always

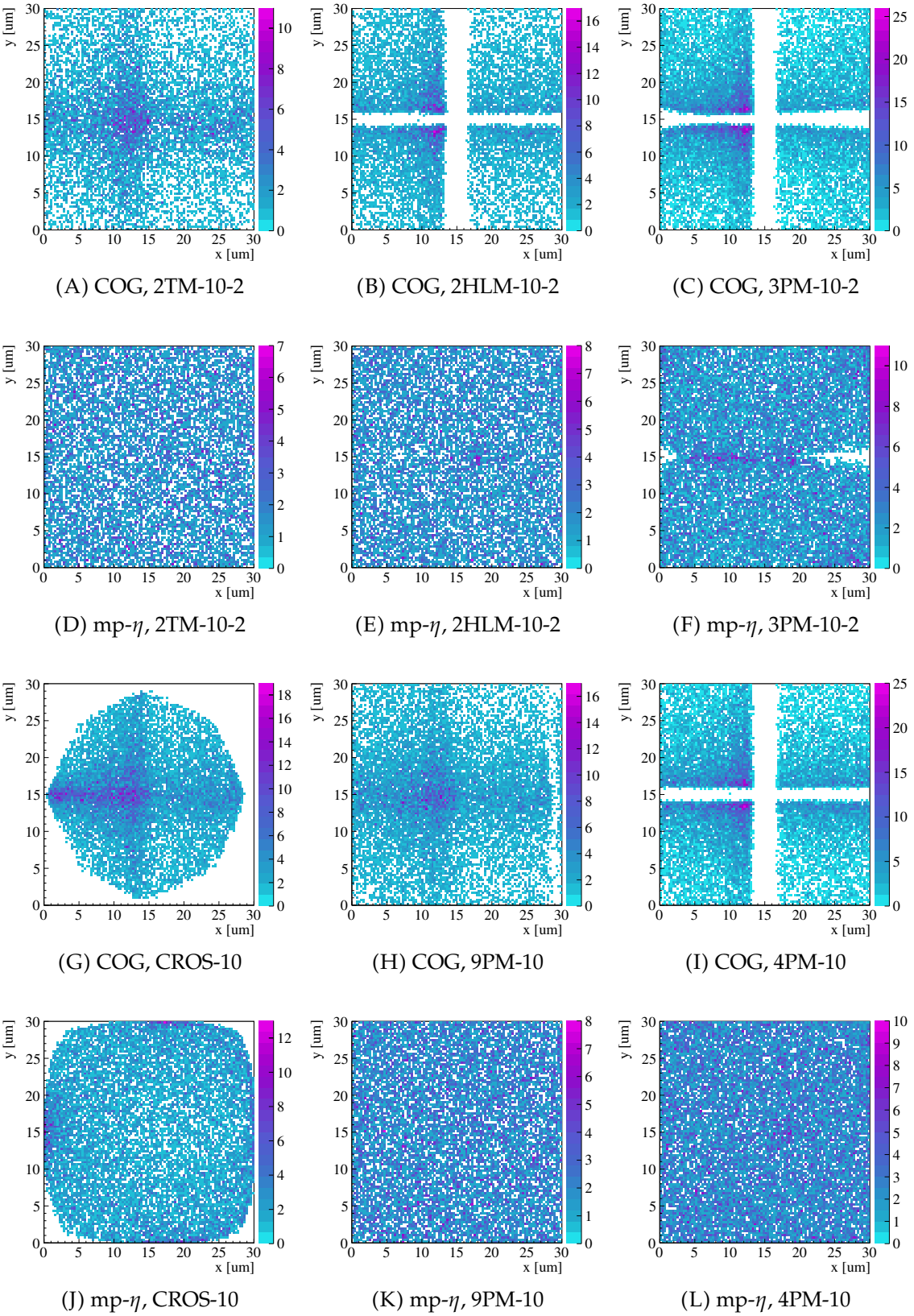

(A) COG, 2TM-10-2 (B) COG, 2HLM-10-2 (C) COG, 3PM-10-2

(D) mp-η, 2TM-10-2 (E) mp-η, 2HLM-10-2 (F) mp-η, 3PM-10-2

(G) COG, CROS-10 (H) COG, 9PM-10 (I) COG, 4PM-10

(J) mp-η, CROS-10 (K) mp-η, 9PM-10 (L) mp-η, 4PM-10

FIGURE 5.25: In-pixel hit position distribution for different clusterization methods with COG position reconstruction and after mp-η correction. Example shown for SF matrix at 130 V back bias for the FZ-n wafer.

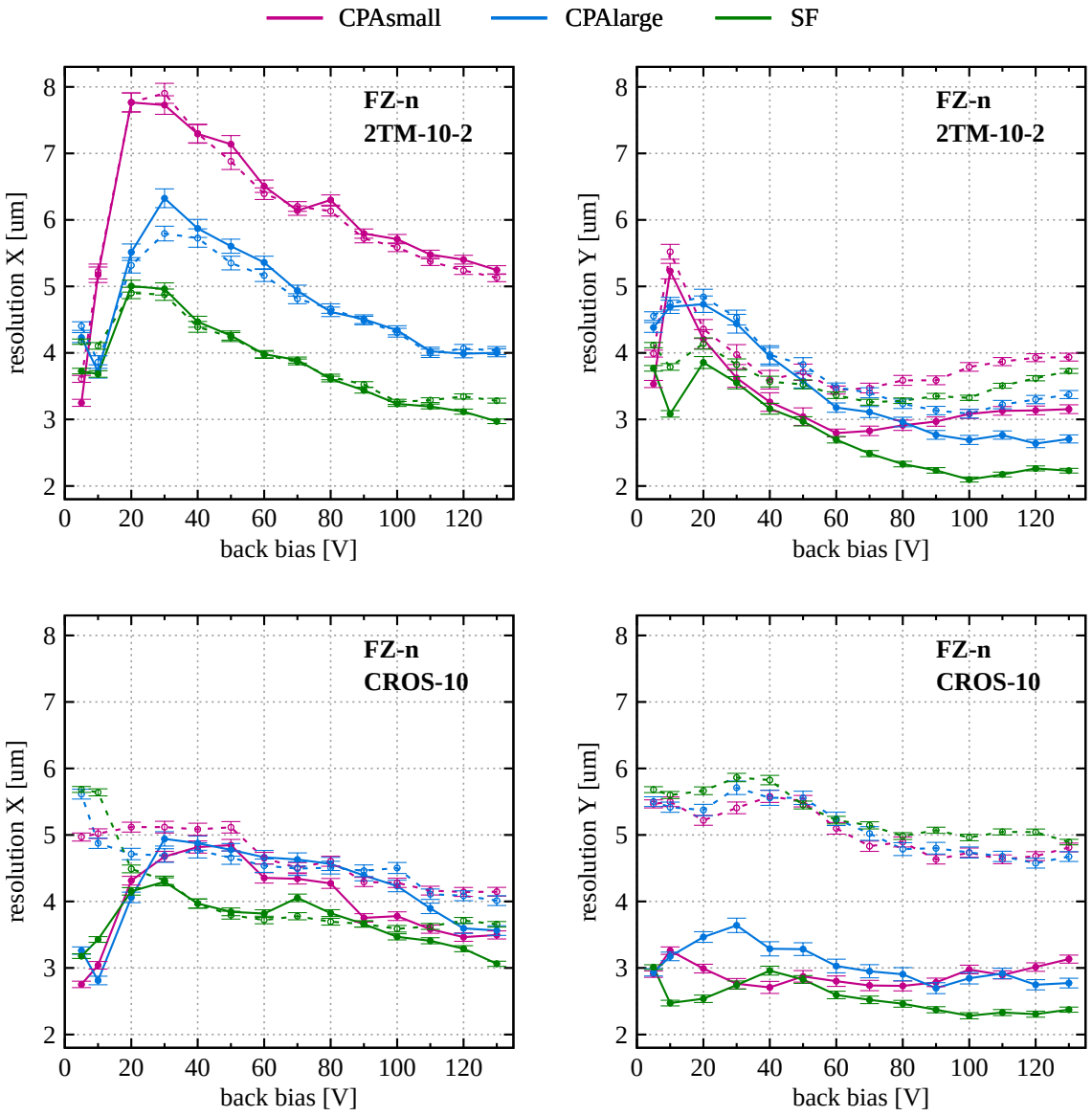

FIGURE 5.26: Comparison of final spatial resolution σ_{res} using 2TM-10-2 and CROS-10 for COG (dashed) and mp-η corrected positions (solid) for the FZ-n.

2 pixels in each direction, thus there is almost no possibility to reconstruct hit in the centre of the pixel which is observed in Fig. 5.25I. Similar behaviour is shown for the 2HLM and 3PM methods, that are also limiting the cluster size. The CROS method, contrary to 4PM, prefers centre of the pixel as it takes odd number of three pixels in each dimension and it does not allow for the hit position reconstruction around the seed pixel corners.

The proposed mp-η makes the in-pixel hit distributions uniform which should move the reconstructed position closer to the true particles impact points. One can notice that for two presented methods, 3PM and CROS, the full uniformity of in-pixel hit position after applying mp-η correction is not obtained. Small deviations are still observed in the most vulnerable regions.

The 3PM is taking small cluster (only 2 pixels in each direction) and the cross-talk in x influences on the results. The interesting case is CROS method. For this cluster formation algorithm, there are no entries towards the corners of the pixel. CROS binds the x and y positions relation in a circle-like shape as shown in Fig. 5.25G. Therefore it is not possible to restore two-dimensional uniformity of the in-pixel hit position by separate, independent x and y transformations. The similar effect is observed for other voltages. Despite the fact that CROS does not provide full uniformity of two-dimensional in-pixel hits distribution, it shows the best spatial resolution performance as presented in the further studies. It is especially observed for low back bias voltages but also above full depletion the cross-shape cluster provides not worse outcomes than other methods.

In Fig. 5.26 the final spatial resolution in function of the back bias voltage for 2TM-10-2 and for CROS-10 algorithms is presented for the FZ-n wafer. The analogous relations for the DSOI-p can be found in appendix A in Fig. A.1. For the x direction, where cross-talk occurs, there is no significant influence of mp-η correction on the results, except very low back bias voltages for the CROS method. The cross-talk effect introduces unphysical distortion, thus mp-η correction is not able to improve the results.

The meaningful differences are observed for y direction, which is more conclusive. There are two cases that have to be considered when analysing Fig. 5.26. The first one is the spatial resolution performance using only COG position calculation approach. One has to notice that in such a case, the 2TM method provides much more accurate position reconstruction than CROS. This is simply explained by comparing Fig. 5.25A and Fig. 5.25G. CROS is significantly limiting the area of hits position reconstruction, because of binding x and y positions as described above, whereas 2TM allows the hits to be reconstructed along whole pixel. Another conclusion may be drawn when comparing CROS and 2TM results after mp-η correction. In this case the meaningful improvement of the CROS method is observed for the whole range of back bias voltages, whereas for the 2TM the enhancement is visible mainly for the higher back bias voltages. For lower back bias voltages the cluster size is large, as shown in Fig. 5.11 on page 78, what causes the reduction of non-uniformities in the in-pixel hit positions distribution. Therefore, the final spatial resolution for lower back bias voltages is less sensitive for mp-η position correction. Additionally, the 2TM final performance for low back bias voltages is distorted by the boundary pixels in the cluster, which signal is relatively highly affected by the noise. This effect is even more intensified, since the boundary pixels are the farthest from the seed pixel and thus they influence significantly the reconstructed cluster position.

Summarizing the mentioned issues, the proposed mp-η correction improves the spatial resolution performance independently on the clusterization method, which can be especially observed above full depletion. This is caused by the fact, that mp-η correction always strives to uniform the in-pixel hit position distribution. However, in order to achieve a good spatial resolution even for large clusters, one can use the CROS method, that is reasonably limiting the cluster size in comparison to the 2TM. Thus, the CROS method with mp-η correction is a good candidate as a universal approach for precise position estimation.

5.5.3 Cluster sizes dependance

In the 2TM clusterization method the clusters of different sizes occur. In Fig. 5.27 the final spatial resolution using COG and mp-η correction is shown, separately for samples of different cluster sizes. The example is shown for the FZ-n wafer but analogous plots for the DSOI-p are presented in the appendix A in Fig. A.2. The data sample was divided into four parts: 1-pixel clusters, 2-pixel clusters, 3-pixel clusters and larger than 3-pixel clusters. Since the resolution is considered separately in x and in y direction, the dimension of the cluster is considered only in particular direction. For example 3-pixel clusters for y resolution always contain events of y clusters size equal to 3, but x dimension is arbitrary. If there is no point on the plot, it means that the data sample was too small to successfully fit a Gaussian function (less than 200 entries). On the presented plots the spatial resolution calculated for entire data sample is also shown in order to compare particular cluster size performance with overall outcome.

The global observation for conclusive y direction is that the 2-pixel clusters always show the best spatial resolution performance of about 0.5 µm better than the whole data sample. The 3-pixel clusters are usually dominating the data sample, thus the resolution of 3-pixel clusters is most often very close to the overall resolution. The large clusters, containing four and more pixels, worsen the overall spatial resolution performance, what might be caused by delta electrons.

For 2-pixel and 3-pixel clusters the proposed mp-η correction provides an improvement of the results for almost all back bias voltages. This is not always observed for large clusters. Only for the SF above full depletion one can say that the positive influence of proposed algorithm is visible. For CPAsmall the curves interlace for several back bias voltages but in overall the results after mp-η correction are better than using COG positions.

Thus, all the mentioned considerations show that the mp-η correction algorithm improves the spatial resolution performance in comparison to standard COG position calculation method. Although the level of improvement is different for various clusterization method and different cluster sizes, applying the proposed correction on position calculation significantly benefit on final results.

5.5.4 Clusterization methods studies

Already in the previous studies it has been observed that the clusterization method may significantly influence on detector spatial resolution performance, especially for partially depleted sensor. It was also investigated that 2-pixel clusters usually show the best spatial resolution performance. Hence, one may suspect that forcing the proper cluster shape also might significantly influence the resolution. In Fig. 5.28 the spatial resolution σ_{res} is presented in function of the back bias voltage for different clusterization methods for the FZ-n wafer.

For the FZ-n wafer the full depletion is achieved above 70 V back bias voltage. The y spatial resolution, that is free from cross-talk effect, is almost independent from clusterization

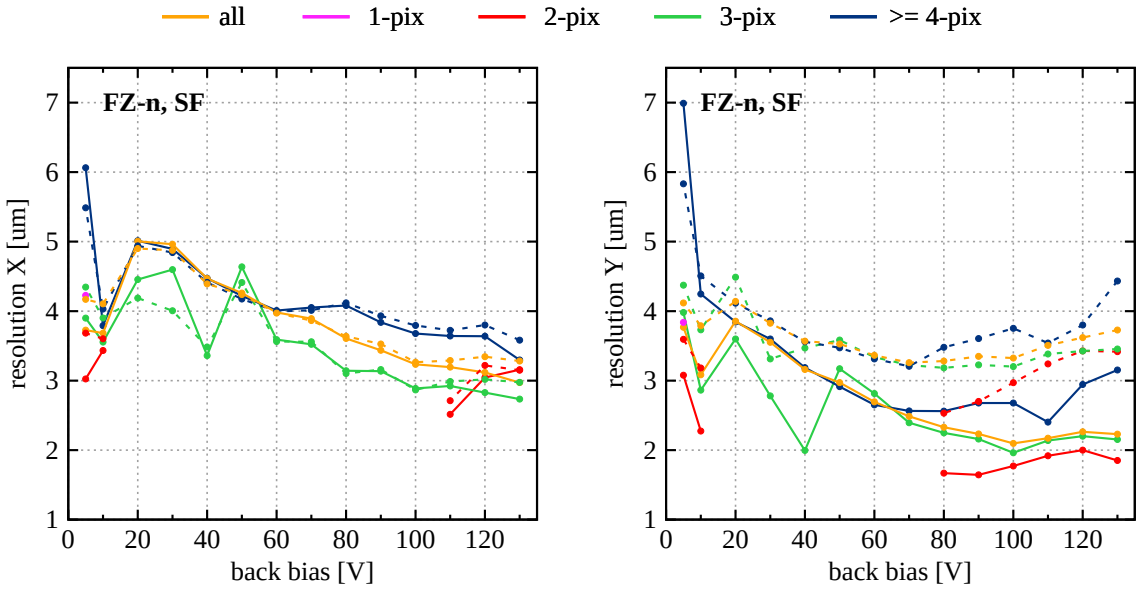

(A) Source followers

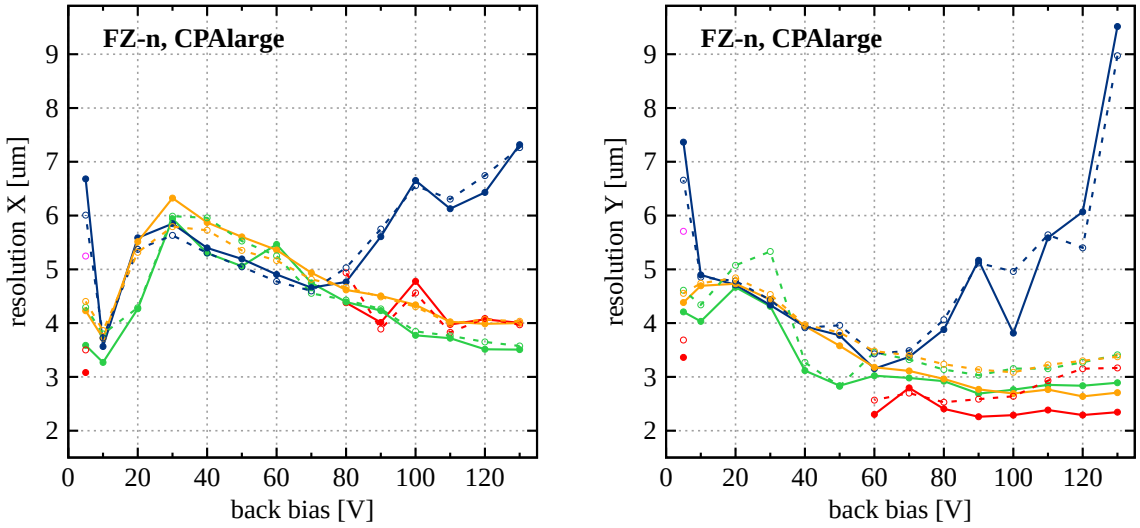

(B) Charge preamplifier with large sensing diode

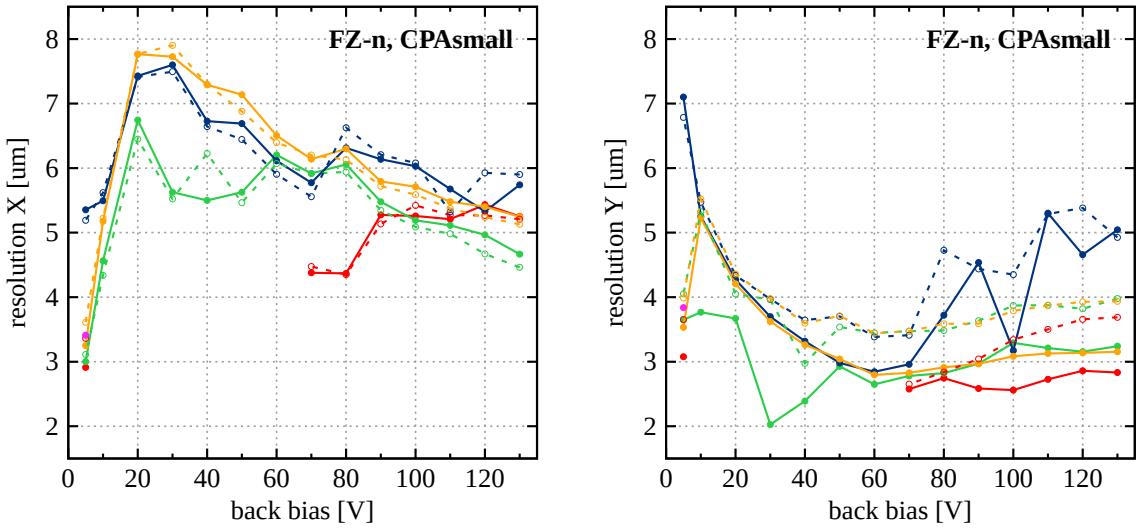

(C) Charge preamplifier with small sensing diode

FIGURE 5.27: Final spatial resolution σ_{res} versus back bias voltage for different cluster sizes at the FZ-n wafer for COG-positions (dashed) and mp-η (solid). The used clusterization method was 2TM-10-2.

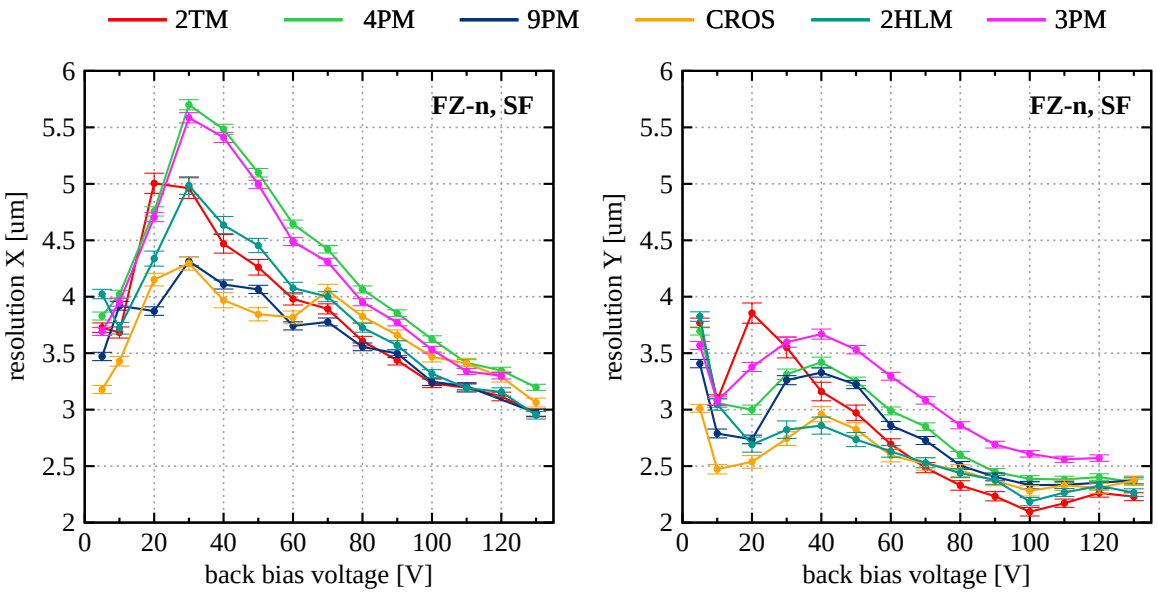

(A) Source followers

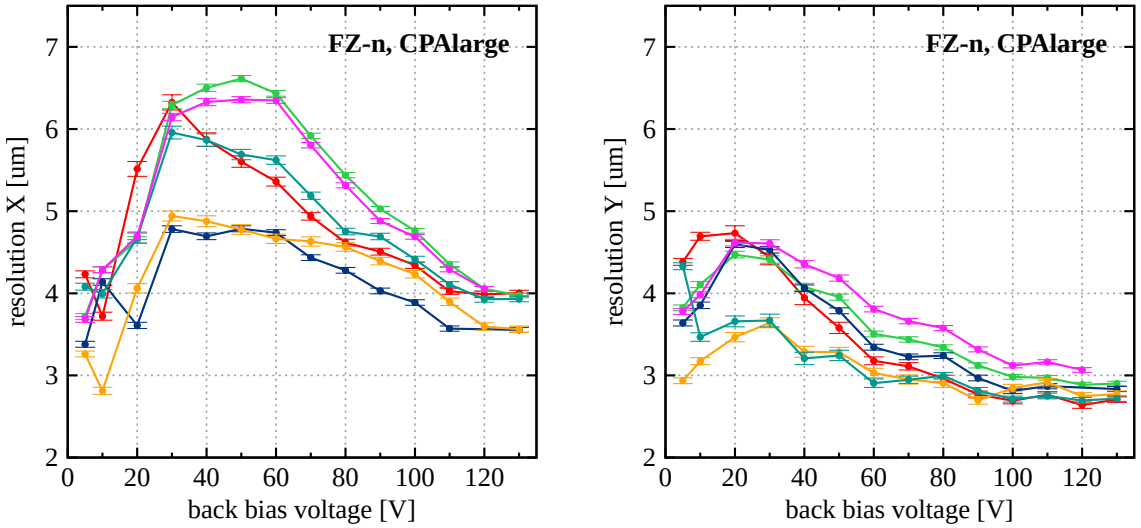

(B) Charge preamplifier with large sensing diode

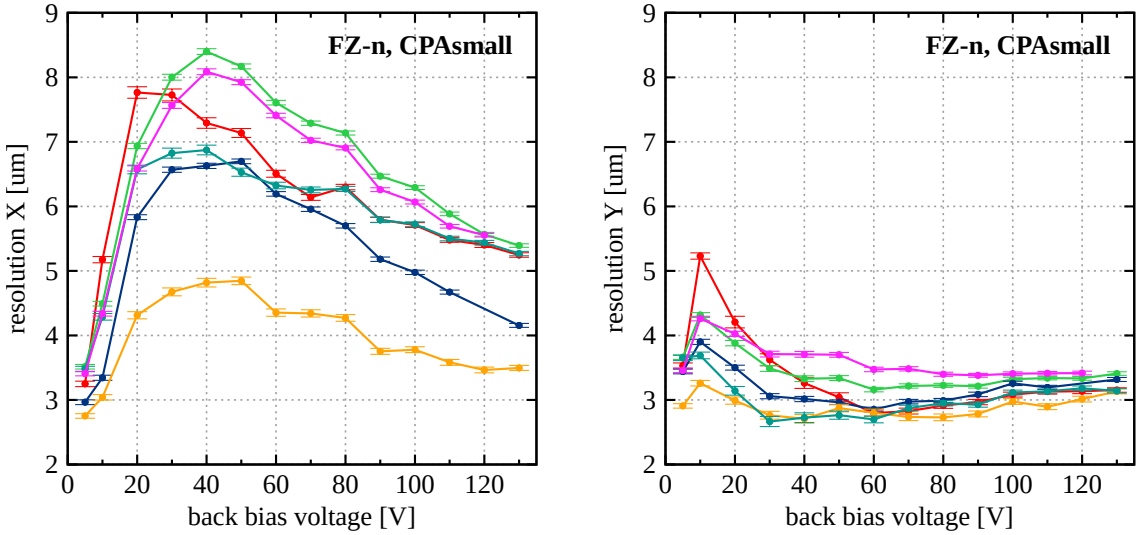

(C) Charge preamplifier with small sensing diode

FIGURE 5.28: Final spatial resolution σ_{res} for the FZ-n wafer in function of back bias voltage for different clusterization methods ($t_{\text{seed}} = 10$ and $t_{\text{neigh}} = 2$).

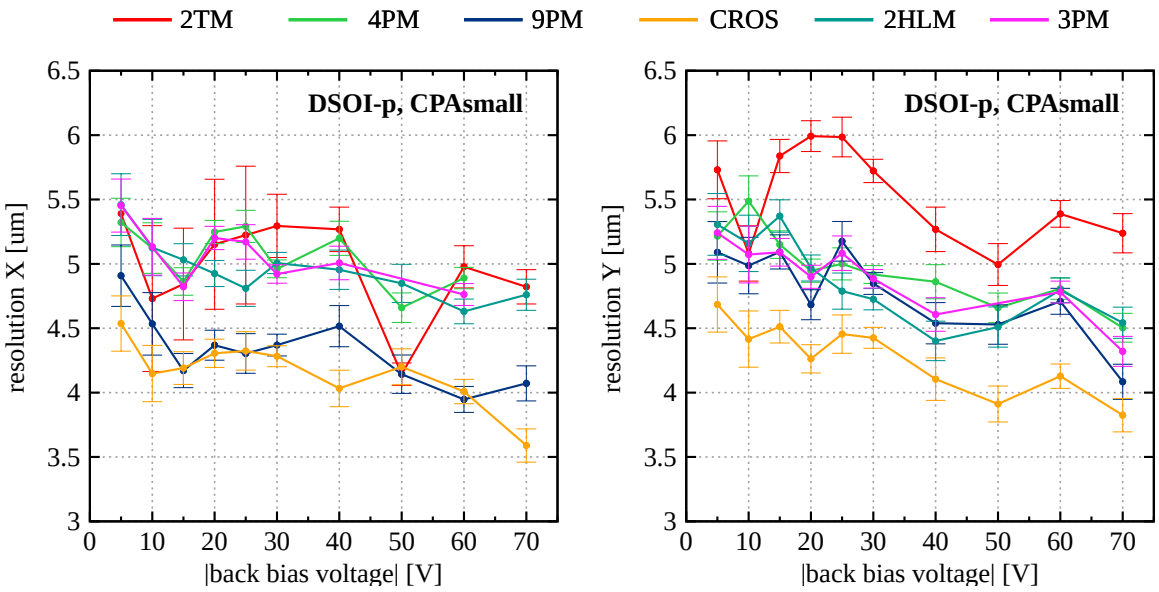

FIGURE 5.29: Final spatial resolution σ_{res} for CPAsmall on the DSOI-p wafer in function of back bias voltage for different clusterization methods.

method when the sensor is fully depleted. For lower back bias voltages reducing the cluster size in comparison to standard 2TM (what is for example done using 2HLM) or taking a fixed-size symmetric cluster (CROS, 9PM) provides better results. Although, decreasing the cluster size too much, as in 3PM and 4PM does not benefit on the spatial resolution for the tested detector. The results for 4PM and 3PM show, that it is better to take more energy to the cluster, than artificially decrease its size and force 2 pixels in one direction. Especially 3PM, that is truly taking two pixels to calculate the hit position gives the worst performance.

For x direction, where the cross-talk affects the signal distribution, using the CROS and 9PM allows to improve significantly the spatial resolution performance. For high back bias voltage it is even possible to be close to resolution obtained in the y direction. Thus, to limit the cross-talk effect one can most probably use the clusterization method that takes an odd number of pixels in particular direction to alleviate charge distribution distortion.

For the DSOI-p only the best behaving matrix is shown here in Fig. 5.29 while the results for other matrices can be found in the appendix A in Fig. A.3. The CPAsmall on the DSOI-p wafer performs roughly as matrices on the FZ-n at low back bias voltages. Thus, almost for all back bias voltage the 2TM shows the worst performance. The best behaviour is again observed for the CROS in y and CROS and 9PM in x as in the case of the FZ-n.

5.5.5 Different prototypes comparison

In order to verify whether the presented results are not biased, the analysis was made for several wafers. For the two FZ-n and two DSOI-p wafers the analysis were repeated in details and for the third wafer only few datasets were checked. The comparison of spatial resolution for the FZ-n wafers are presented in Fig. 5.30. The similar plots for the DSOI-p can be found in the appendix A in Fig. A.4. The results are shown for the CROS-10 method, as for the previous cases. The differences between different back bias voltages are in the

range from 10 % to 30 %, except CPAsmall in x direction. However, one has to remember that x coordinate is not conclusive since the cross-talk occurred. The curves have a similar trends, thus one can conclude that the obtained results are coherent.

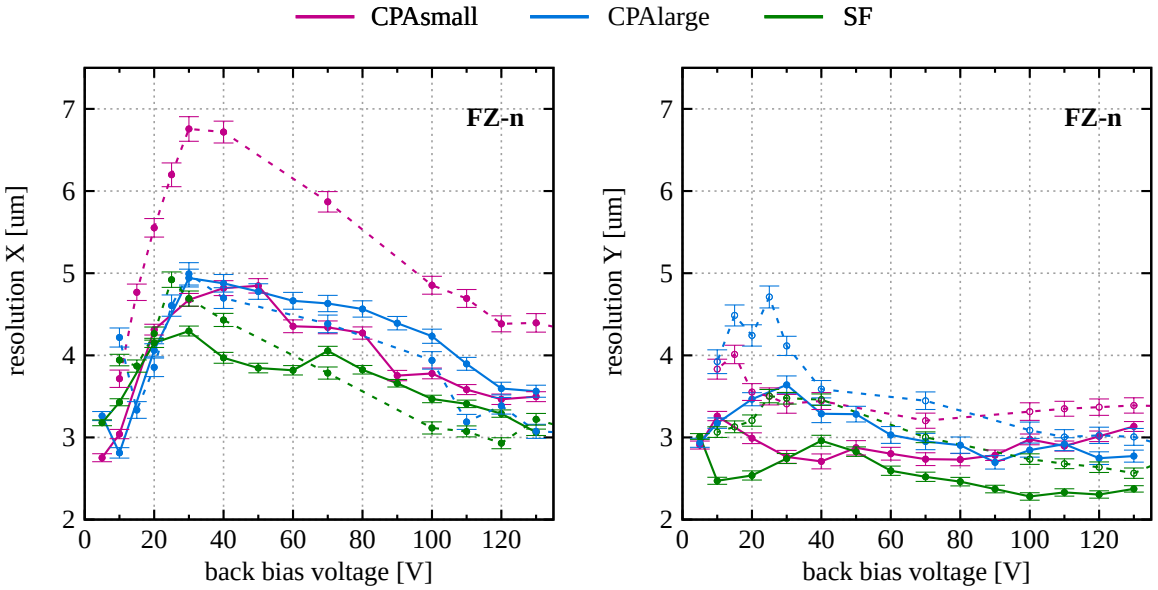

FIGURE 5.30: Final spatial resolution σ_{res} for two different FZ-n detectors. The CROS-10 method was used. Soild line corresponds to the prorotype previously shown in this work.

5.5.6 Spatial resolution summary

In Fig. 5.31 the summary plot of the final spatial resolution is presented, showing the x and y results for the FZ-n and DSOI-p wafers and all matrices obtained using the CROS clusterization method. The x direction is affected by cross-talk effect, thus the results for this coordinate are usually significantly worse.

For the FZ-n wafer both source followers and charge-sensitive preamplifiers show a very good performance. Both CPAlarge and CPAsmall achieve about 3 µm of spatial resolution above full depletion. Nevertheless, also on the FZ-n CPAlarge behaved not always understandable, for example considering baseline performance or the efficiency studies. Thus, it is reasonably not to use too large BP(N)W layers in comparison to the pixel pitch. In this work, it was also shown that CPAsmall matrix (with small BP(N)W size) is working well on the FZ-n wafer, although it was not obvious from theoretical point of view. Finally, the best performance is observed for the source followers matrix on the FZ-n characterized by the highest SNR of 350 above full depletion. The y spatial resolution for this matrix is in the best case 2.1 µm at 100 V. Moreover, the source followers spatial resolution is below 3 µm starting from 10 V of back bias voltage. This voltage value corresponds to about 150 µm of depletion region, which can roughly translate to the CLIC vertex detector material budget demand. Although, one has to remember, that the significant influence from non-depleted volume is suspected to occur, enlarging the cluster size at low back bias voltages. This means, that the thinned wafer might show different performance than the tested 500 µm thick FZ-n wafer

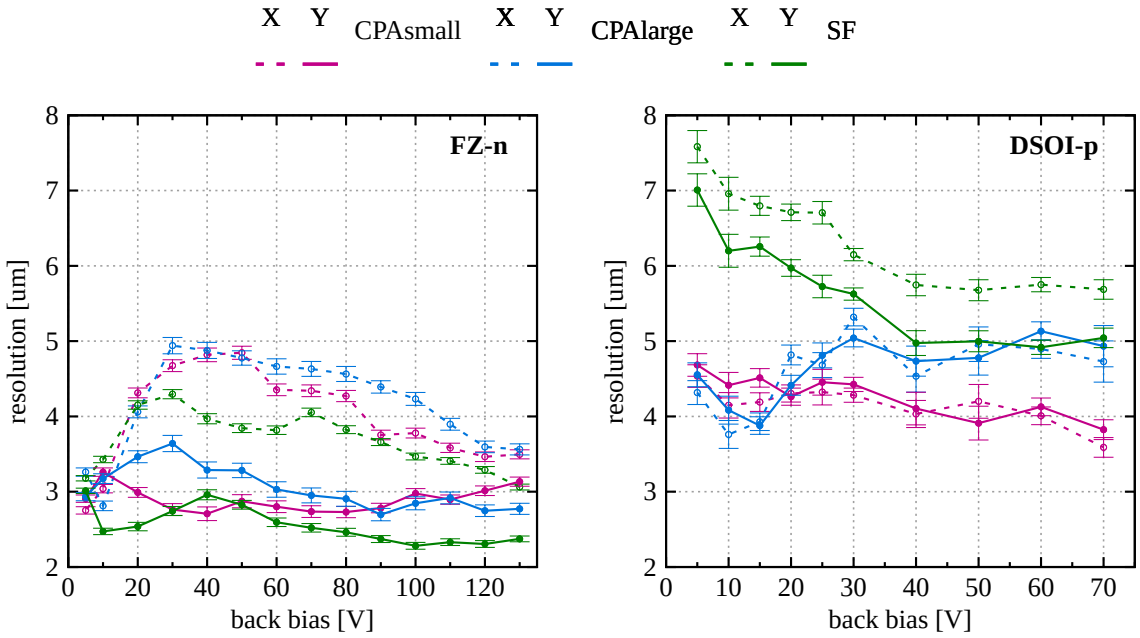

FIGURE 5.31: Summary final spatial resolution σ_{res} for the FZ-n (left) and the DSOI-p (right) in function of the back bias voltage. The CROS-10 method was used.

at 10 V back bias voltage. Nevertheless, the source followers matrix shows state-of-the-art performance achieving very good spatial resolution.

The spatial resolution for the DSOI-p wafer is significantly worse than on the FZ-n, mainly because of the fact that the wafer is not fully depleted. The SF matrix has a poor SNR and thus the spatial resolution is in the best case only around 5 µm. Still, it is better than binary systems resolution prediction. The best performance has a dedicated for the DSOI-p CPAsmall matrix achieving the spatial resolution of 3.6 µm in x and 3.8 µm in y direction in the best case. When the DSOI-p process will be improved by the manufacturer and the structure can be fully depleted, the CPA pixels with relatively small sensing diodes should be considered for this wafer type.

Conclusions

The aim of my doctoral studies was the R&D in the field of monolithic pixel detectors development in the Lapis SOI CMOS technology, targeted at meeting the requirements of the CLIC vertex detector. I participated in the design of detectors, simulations, laboratory measurements and beam tests. However, the main goal of this dissertation was to carry out a comprehensive, complex analysis of test-beam data from SOI pixel detector focused on the spatial resolution requirements of the CLIC vertex detector.

During my PhD studies, I have participated in four ASICs design in SOI technology. In the first two projects, I was responsible for preparing the SAR ADC for future use in the SOI detectors. In the third project, I was a co-creator of the self-triggering pixel detector design, and my task was to design and simulate blocks of control logic and pixel matrix readout system. Most effort was put into the final and fourth work – CLIPS detector project, focused on fulfilling the spatial resolution, time resolution and material budget requirements of the CLIC vertex detector. In the case of CLIPS, I was mainly responsible for the circuitry of the matrix reading control, but also for the preparation of pixel test structures.

I was involved in two test-beams carried out in the SPS at CERN, in 2016 and 2017 respectively, when two of the designed prototypes of the SOI detectors were measured. During the test beams, I was responsible for the verification of the quality of collected data, as well as for ongoing data analysis.

Detector assemblies, tested during the test beams, were fabricated on the 500 µm thick FZ-n wafer and the DSOI-p 300 µm thick wafer. In addition, two architectures of pixel readout electronics have been implemented, source followers pixels and charge-sensitive preamplifiers. To achieve the goal of the CLIC vertex detector spatial resolution demand (below 3 µm), several dedicated analysis methods have been developed, such as mp-η correction or various cluster formation algorithms. The detailed process of analysis flow and full results were presented in this dissertation.

In my work, it has been shown that the best performance is obtained for the FZ-n at source follower pixel, for which the spatial resolution of 2.1 µm for $30 \times 30\,\mu m^2$ pixel pitch is obtained. The FZ-n charge preamplifier pixels are also characterized by a very good position reconstruction accuracy of about 2.7 µm. These results are promising as regards the CLIC vertex detector requirements, but it should be remembered that the measurements were done for 500 µm thick wafer, while CLIC requirements were 200 µm or less, including cables and other necessary infrastructure.

There are no unambiguous conclusions for the DSOI-p wafer type pixels because it was not fully depleted due to unknown currents leakage. Since this type of wafer is more promising in the case of radiation hardness, it can be expected that the manufacturer will improve

with upgrading of the production process in the near future. However, the obtained DSOI-p results, even on a not fully depleted sensor, are already reasonably satisfactory. The best performing charge preamplifier matrix with small sensor diodes achieves the spatial resolution of approximately 3.6 µm.

As shown in this dissertation, the obtained spatial resolution results could be even better if understanding the non-Gaussian shape of the residua distributions. Since various issues related to the DUT have already been investigated in the case of this problem, the quality of the telescope data should be studied more. It is possible that some telescope parameters affect the final performance results of the DUT.

The efficiency remains also a matter of future research. The measured efficiency is around 96 % – 98 %. There is a suspicion that a few percent of inefficiencies may result from the merged problems with the detector dead time and the pile-up effect, which is assessed to be between 1 % and 3 %. Nevertheless, both mentioned sources of inefficiency should be further investigated at the level of data analysis.

The performed analyses provide a broad knowledge of Japanese Lapis SOI CMOS technology in terms of its application for monolithic pixel detectors. It has been proven that Lapis SOI CMOS 200 µm gives us great design options of state-of-the-art performance devices. In this way, the main goal of my thesis was achieved, because it was experimentally verified that the tested prototypes are able to meet the requirements of highly demanding detectors intended for high energy physics experiments, in particular the CLIC vertex detector. The presented work reveals the areas of research that should be further studied, at the same time it also provides a very promising basis for future research. Direct continuation of the R&D tests carried out will be the measurement of the CLIPS detector. As mentioned above, CLIPS has been designed to meet most CLIC vertex detector requirements, especially 3 µm spatial resolution (on 20 µm pixel pitch) with detector wafer not thicker than 100 µm. Time-stamping is also anticipated better than 10 ns. CLIPS has already been fabricated and the preparation of its measurement setup is in progress.

Appendix A

Double SOI detailed results

COG and mp-η correction comparison on 2TM and CROS

In Fig. A.1 the spatial resolution for the DSOI-p wafer is shown before and after mp-η correction for 2TM-10-2 and CROS-10.

Spatial resolution dependence on cluster size

In Fig. A.2 the final spatial resolution is presented using COG and mp-η correction shown separately for data samples of different cluster sizes for the DSOI-p wafer. The data sample was divided into four subsamples: one pixel clusters, two pixel clusters, three pixel clusters four and more pixel clusters.

Spatial resolution dependence on clusterization method

In Fig. A.3 the final spatial resolution is presented for various clusterization methods the DSOI-p wafer. The results are shown after mp-η correction.

Different prototypes comparison

The comparison of final spatial resolution using CROS-10 method after mp-η correction for the two different DSOI-p detectors are shown in Fig. A.4.

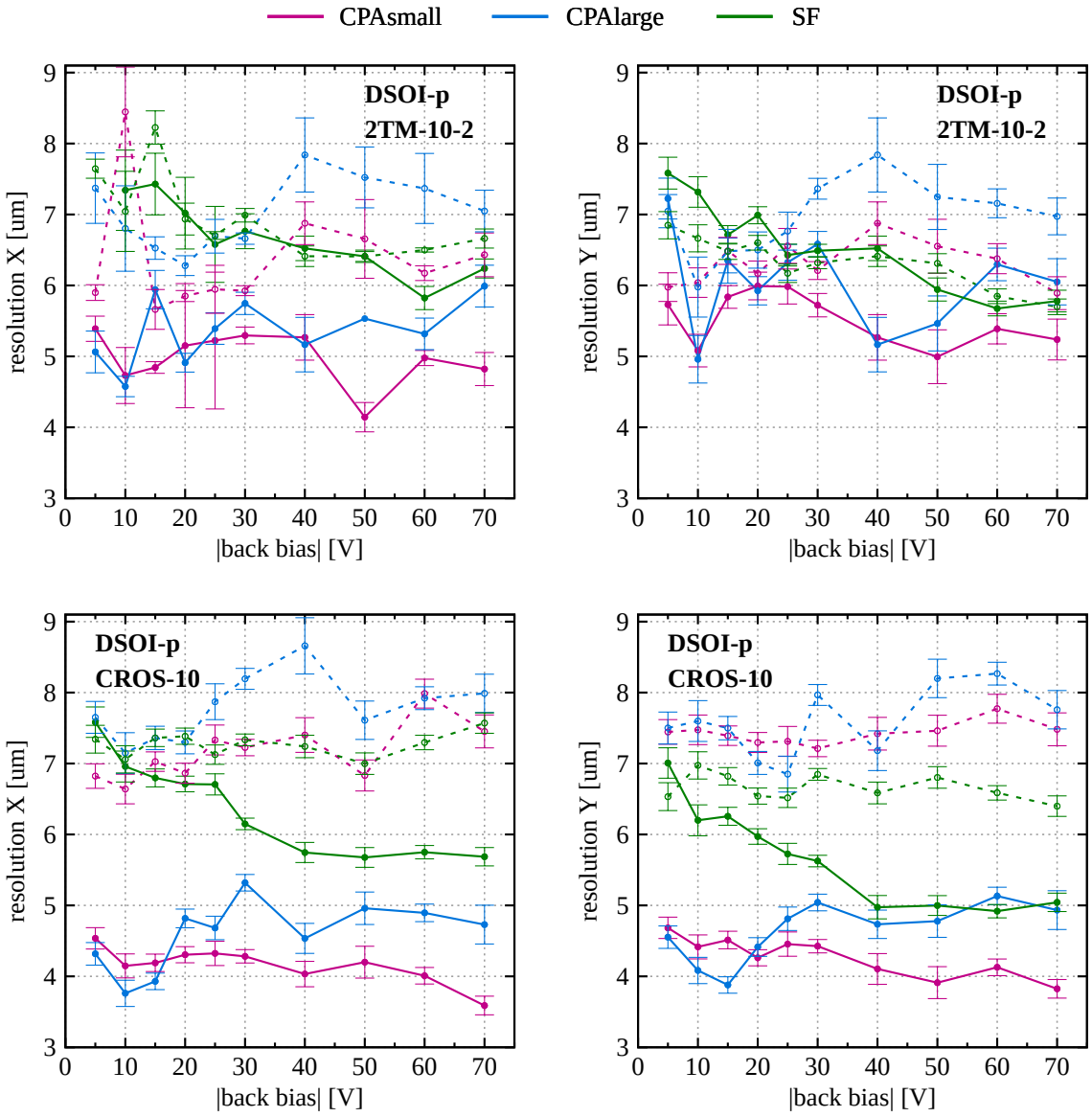

FIGURE A.1: Comparison of final spatial resolution σ_{res} using 2TM-10-2 and CROS-10 for COG (dashed) and mp-η corrected positions (solid) for the DSOI-p wafer.

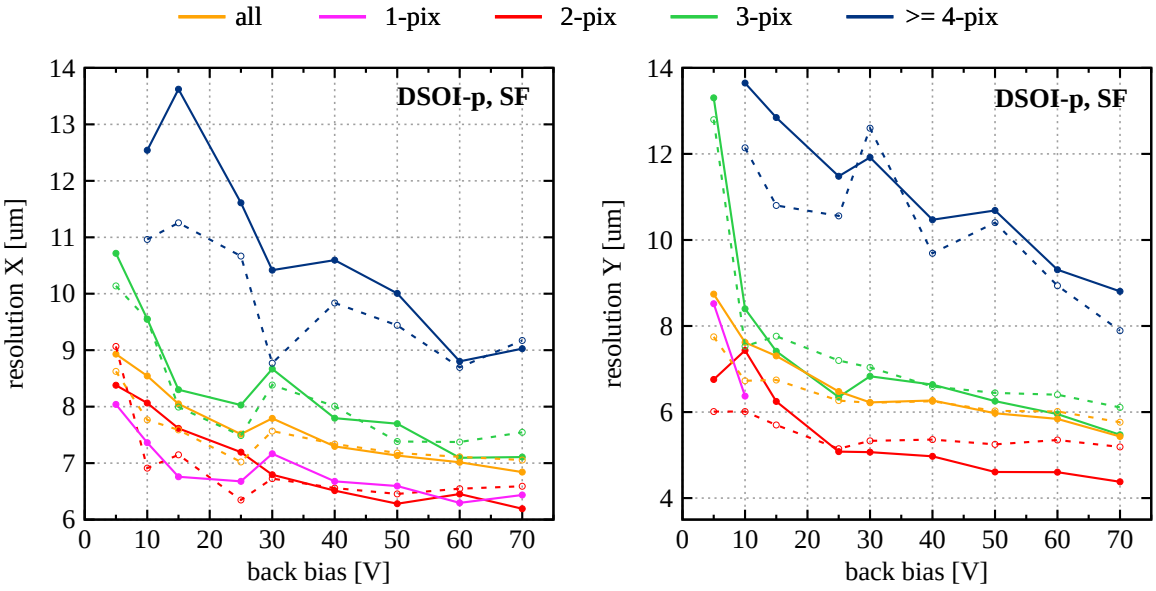

(A) Source followers

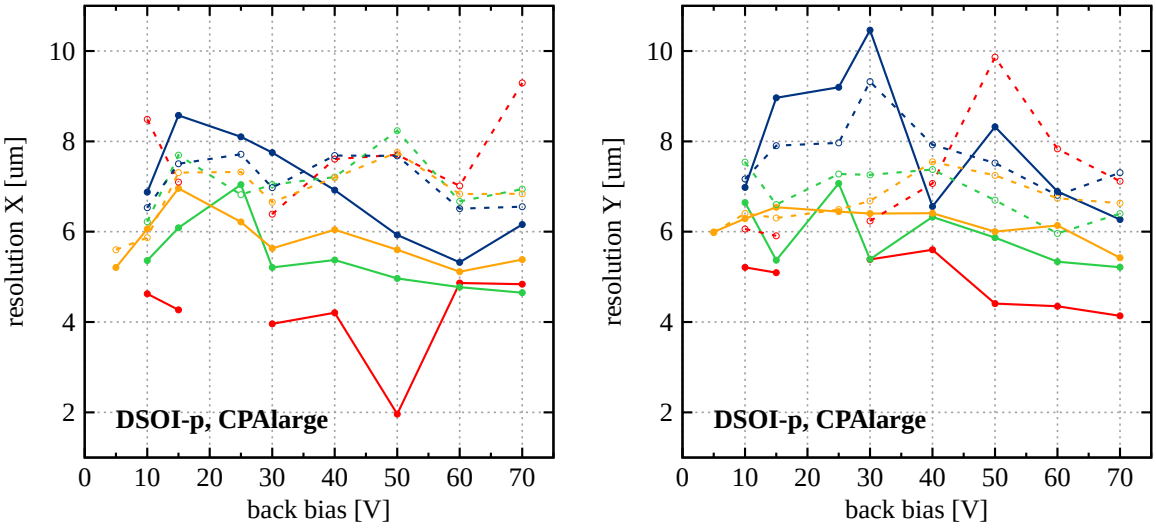

(B) Charge preamplifier with large sensing diode

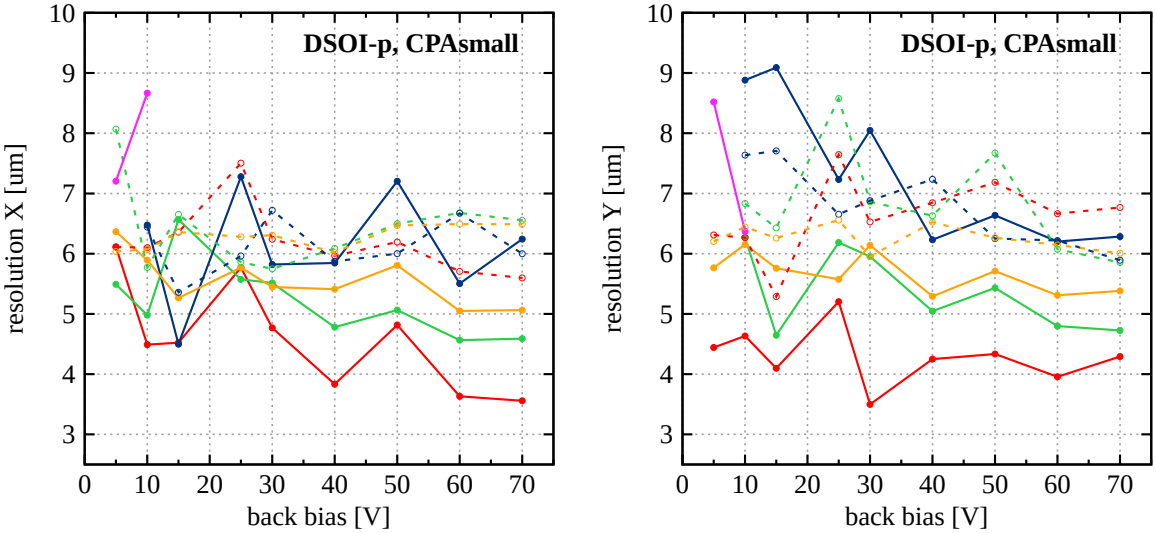

(C) Charge preamplifier with small sensing diode

FIGURE A.2: Final spatial resolution σ_{res} versus a back bias voltage for different cluster sizes (2TM-10-2) at the DSOI-p wafer for COG-positions (dashed) and mp-η corrected (solid).

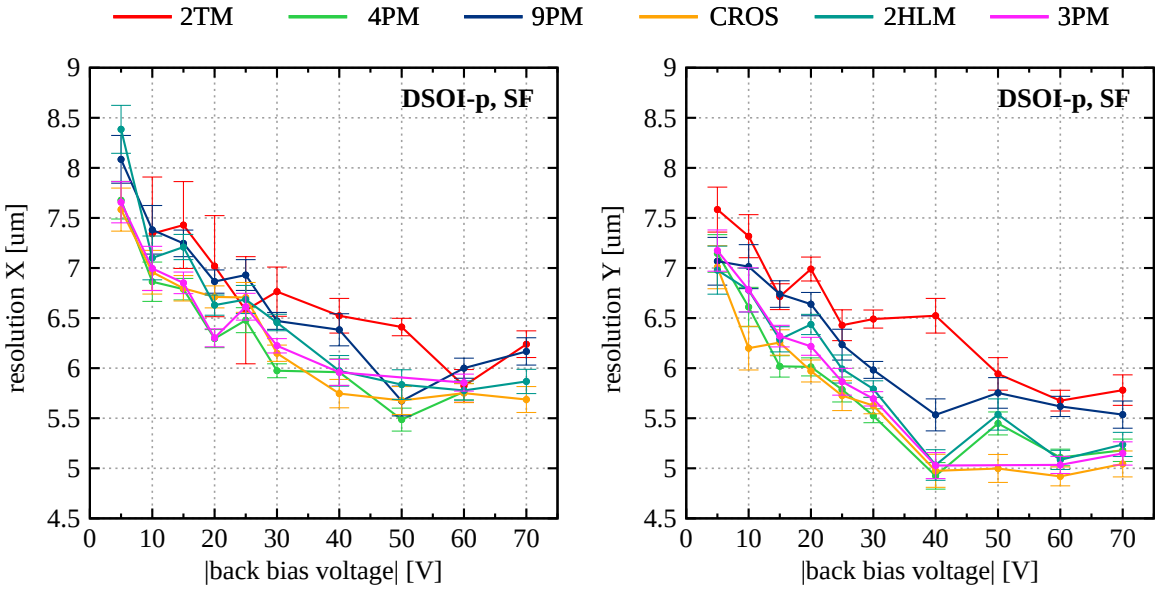

(A) Source followers

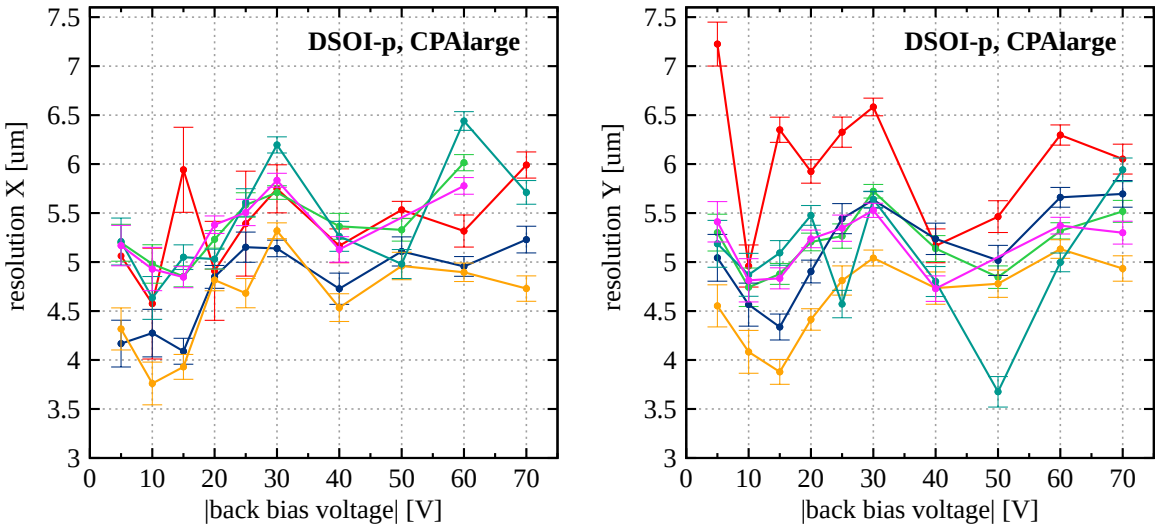

(B) Charge preamplifier with large sensing diode

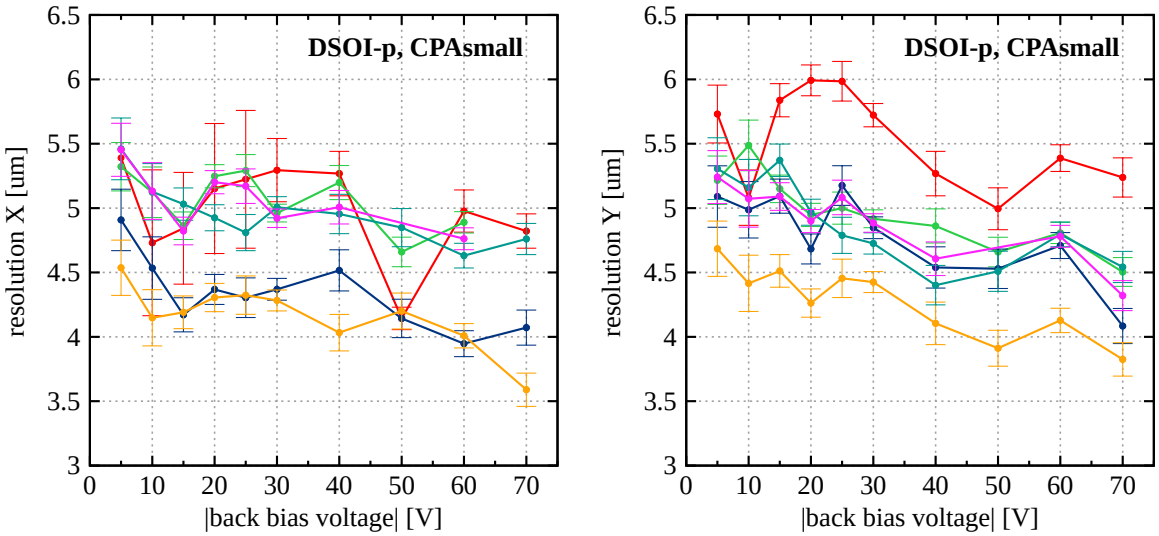

(C) Charge preamplifier with small sensing diode

FIGURE A.3: Final spatial resolution σ_{res} for the DSOI-p wafer in function of back bias voltage for different clusterization methods ($t_{\text{seed}} = 10$ and $t_{\text{neigh}} = 2$).

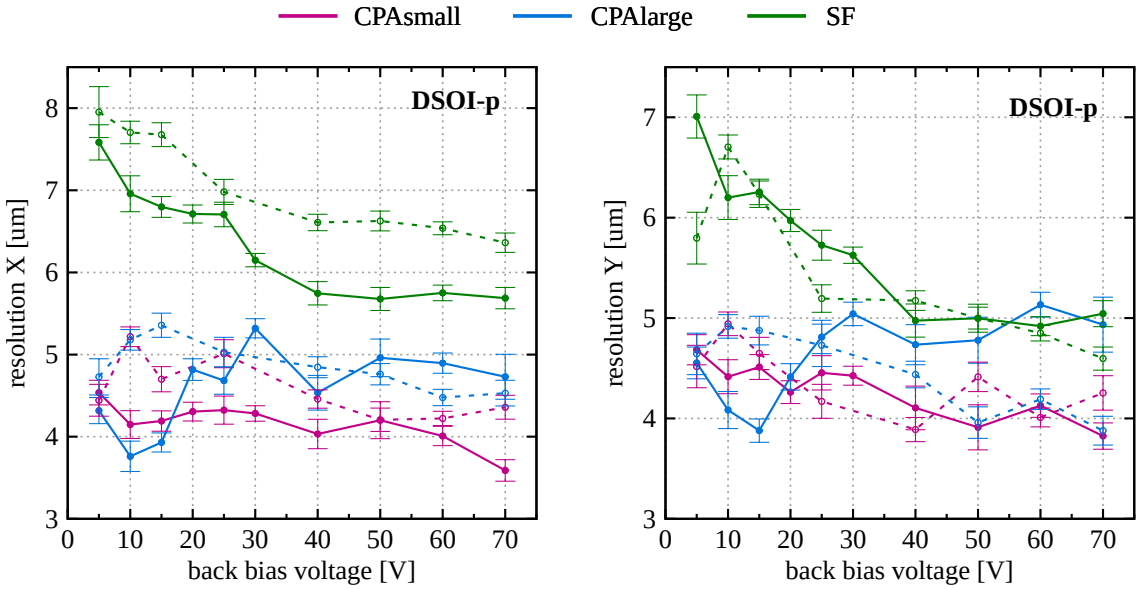

FIGURE A.4: Final spatial resolution σ_{res} for different wafers for the DSOI-p wafer. The used clusterization method was CROS-10.

Bibliography

[1] G. Aad et al., ATLAS Collaboration, "Observation of a new particle in the search for the Standard Model Higgs boson with the ATLAS detector at the LHC", *Physics Letters B* **2012**, *716*, 1–29.

[2] S. Burkhard, "The High-Luminosity upgrade of the LHC: Physics and Technology Challenges for the Accelerator and the Experiments", *Journal of Physics: Conference Series* **2016**, *706*, 022002.

[3] T. Miyoshi et al., "Performance study of monolithic pixel detectors fabricated with FD-SOI technology", *2011 IEEE Nuclear Science Symposium Conference Record* **2011**, 1702–1707.

[4] S. Ono et al., "Development of a pixel sensor with fine space-time resolution based on SOI technology for the ILC vertex detector", *Nuclear Instruments and Methods in Physics Research Section A* **2018**, *845*, 139–142.

[5] H. Hideki et al., "Evaluation of Kyoto's event-driven X-ray astronomical SOI pixel sensor with a large imaging area", *Nuclear Instruments and Methods in Physics Research Section A* **2018**.

[6] K. Hara et al., "Development of INTPIX and CNTPIX Silicon-On-Insulator Monolithic Pixel Devices", *Vertex Conference* **2010**.

[7] Y. Arai et al., "Performance of the INTPIX6 SOI pixel detector", *Journal of Instrumentation* **2017**, *12*, C01028–C01028.

[8] `http://eutelescope.web.cern.ch/`.

[9] "Physics and Detectors at CLIC: CLIC Conceptual Design Report", **2012**, (Eds.: L. Linssen et al.), DOI `10.5170/CERN-2012-003`.

[10] M. J. Boland et al., "Updated baseline for a staged Compact Linear Collider", **2016**, (Eds.: P Lebrun et al.), DOI `10.5170/CERN-2016-004`.

[11] T. Charles et al., "The Compact Linear Collider (CLIC) - 2018 Summary Report", CERN Yellow Reports: Monographs **2018**, *1802*.

[12] `http://clicdp.web.cern.ch`.

[13] H. Abramowicz et al., CLIC Collaboration, "Higgs physics at the CLIC electron–positron linear collider", *Eur. Phys. J.* **2017**, *C77*, 475.

[14] R. Philipp, "Physics analyses overview", Physics at CLIC Workshop, **2017**, `https://indico.cern.ch/event/632228/contributions/2650529/attachments/1493752/2323096/physics_at_clic_workshop_philipp_roloff_07_07_2017.pdf`.

[15] D. Dannheim, A. Sailer, Beam-Induced Backgrounds in the CLIC Detectors, **2012**, https://cds.cern.ch/record/1443516.

[16] N. Alipour Teherani et al., CLICdet: The post-CDR CLIC detector model, **2017**, http://cds.cern.ch/record/2254048.

[17] D. Dannheim, "The CLIC detector", Linear Collider Vertex Workshop, Tegernsee, **2017**, "https://agenda.linearcollider.org/event/7450/contributions/38579/attachments/31545/47519/CLIC_detector_LC_VTX_WS_1May2017.pdf".

[18] D. Dannheim, "The CLIC Vertex Detector", *Journal of Instrumentation* **2015**, *10*, C03025.

[19] A. Nurnberg, D. Dannheim, Requirements for the CLIC tracker readout, **2017**, https://cds.cern.ch/record/2261066/files/CLICdp-Note-2017-002.pdf.

[20] *Particle Detectors*, Cambridge University Press, **2008**.

[21] S. Spannagel, "Silicon Technologies for the CLIC Vertex Detector", *Jornal of Instrumentation* **2017**, *12*, C06006.

[22] L. Greiner et al., "A MAPS based vertex detector for the STAR experiment at RHIC", *Nuclear Instruments and Methods in Physics Research Section A* **2010**, *650*, 68–72.

[23] J. Kemmer, G. Lutz, "New detector concepts", *Nuclear Instruments and Methods in Physics Research Section A* **1987**, *253*, 365–377.

[24] A. Nurnberg, "Silicon pixel-detector R& D for CLIC", *Journal of Instrumentation* **2016**, *11*, C11039–C11039.

[25] M. Munker, CLIC Collaboration, Status of silicon detector R& D at CLIC, *VERTEX2018 Conference*, Chennai, India, **2018**, https://indico.cern.ch/event/710050/contributions/3185365/attachments/1739908/2815086/slides_munker_vertex2018.pdf.

[26] M. D. Buckland, "Simulation and evaluation of HV-CMOS pixel sensors for the CLIC vertex detector", *CERN-THESIS-2018-114* **2018**, PhD Thesis.

[27] I. Kremastiotis et al., "Design and standalone characterisation of a capacitively coupled HV-CMOS sensor chip for the CLIC vertex detector", *Journal of Instrumentation* **2017**, *12*, P09012.

[28] I. Perić, "Hybrid Pixel Particle-Detector Without Bump Interconnection", *Nuclear Science IEEE Transactions on* **2009**, *56*, 519 –528.

[29] M. Munker, "Test beam and simulation studies on High Resistivity CMOS pixel sensors", *CERN-THESIS-2018-202* **2018**, PhD Thesis.

[30] M. Munker et al., Study of the ALICE Investigator chip in view of the requirements at CLIC, **2017**, https://cds.cern.ch/record/2284145/files/investigator_pub_v2.pdf.

[31] R. Bugiel et al., "Test-beam results of a SOI pixel-detector prototype", *Nuclear Instruments and Methods in Physics Research Section A: Accelerators Spectrometers Detectors and Associated Equipment* **2018**, *901*, 173–179.

[32] K. Hara, Radiation hardness of Silicon-On-Insulator Pixel Devices - ten years struggle, *11th International "Hiroshima" Symposium on the Development and Application of Semiconductor Tracking Detectors (HSTD11) in conjunction with 2nd Workshop on SOI Pixel Detectors (SOIPIX2017)*, OIST, Okinawa, **2017**, `https://indico.cern.ch/event/577879/contributions/2741626/attachments/1574468/2485728/HSTD11-hara2.pdf`.

[33] K. Hara et al., "Fine-Pixel Detector FPIX Realizing Sub-micron Spatial Resolution Developed Based on FD-SOI Technology", *Proceedings of International Conference on Technology and Instrumentation in Particle Physics 2017* **2018**.

[34] S. Ono, Beam test results of an SOI monolithic pixel sensor SOFIST for the ILC vertex detector, *The 9th International Workshop on Semiconductor Pixel Detectors for Particles and Imaging (PIXEL2018)*, Academia Sinica, Taipei, **2018**, `https://indico.cern.ch/event/669866/contributions/3235134/attachments/1768868/2873181/0900-Beam_test_results_of_an_SOI_monolithic_pixel_sensor_SOFIST_for_the_ILC_vertex_detector.pdf`.

[35] M. Tanabashi et al., "Review of Particle Physics", *Phys. Rev. D* **2018**, *98*, 030001.

[36] *Handbook of Particle Detection and Imaging*, Springer, **1012**.

[37] L. Landau, "On the energy loss of the fast particles by ionization", *J. Phys.* **1944**.

[38] B. Rossi, *High-energy Particles*, New York, **1952**.

[39] S.-S. Li, W.-R. Thurber, "The dopant density and temperature dependence of electron mobility and resistivity in n-type silicon", *Solid State Electronics* **1977**, *20*, 609–616.

[40] J. M. Dorkel, P. Leturcq, "Carrier mobilities in silicon semi-empirically related to temperature, doping and injection level", *Solid State Electronics* **1981**, *24*, 821–825.

[41] K. Korbel, *UKŁADY ELEKTRONIKI FRONT-END*.

[42] C. Jacoboni et al., "A review of some charge transport properties of silicon", **1977**, *20*, 77–89.

[43] *Radiation detection and measurement, 3rd edition*, John Wiley & Sons, **2000**.

[44] S. Spannagel, "Test Beam Measurements for the Upgrade of the CMS Pixel Detector and Measurement of the Top Quark Mass from Differential Cross Sections", *Hamburg University* **2015**, PhD Thesis.

[45] M. Ahmed et al., "Prototype pixel detector in the SOI technology", *Journal of Instrumentation* **2014**, *9*, C02010–C02010.

[46] S. Bugiel et al., "Development of pixel detector in Novel sub-micron technology SOI CMOS 200 nm", *Proceedings of the 21st International Conference Mixed Design of Integrated Circuits and Systems MIXDES 2014 Lviv Ukraine June 19-21 2014* **2014**, 205–208.

[47] CERN, ROOT Data Analysis Framework, `https://root.cern.ch/`.

[48] K. Akiba et al., "The Timepix Telescope for high performance particle tracking", *Nuclear Instruments and Methods in Physics Research Section A: Accelerators Spectrometers Detectors and Associated Equipment* **2013**, *723*, 47–54.

[49] N. Alipour Tehrani, "Test-beam measurements and simulation studies of thin pixel sensors for the CLIC vertex detector", *ETH ZURICH* **2017**, PhD Thesis.

[50] B. van der Heijden et al., "SPIDR, a general-purpose readout system for pixel ASICs", *Journal of Instrumentation* **2017**, *12*, C02040–C02040.

[51] V. Blobel, "Software alignment for tracking detectors", *Nuclear Instrumentation Methods* **2006**, *A566*, 5–13.

[52] E. Belau et al., "Charge Collection In Silicon Strip Detectors", *Nuclear Instruments and Methods in Physics Research* **1983**, *214*, 253–260.

[53] R. Turchetta, "Spatial resolution of silicon microstrip detectors", *Nuclear Instruments and Methods in Physics Research A* **1993**, *335*, 45–58.